UNIVERSITY OF GENOVA

PHD PROGRAM IN BIOENGINEERING AND ROBOTICS

Design and Operation Methodologies for Upper-Limb Exoskeletons

by

Francesco Lago

Thesis submitted for the degree of *Doctor of Philosophy* (38° cycle)

April 2026

Prof. Giuseppe Carbone — Supervisor

Prof. Antonio Sgorbissa — Head of the PhD program

Borsa di dottorato cofinanziata con risorse dell'Unione europea-*NextGenerationEU*
Piano Nazionale di Ripresa e Resilienza Missione 4, componente 1 *"Potenziamento dell'offerta dei servizi di istruzione: dagli asili nido all'Università"*

Count what can be counted,
measure what is measurable
and make measurable what is not.

— attributed to Galileo Galilei

Declaration

I hereby declare that this thesis is entirely my own work, except where otherwise stated, and that all sources of information have been duly acknowledged. This work has not been submitted for any other academic degree or diploma.

Francesco Lago
April 2026

Acknowledgements

I would like to thank Professor Giuseppe Carbone for offering me the opportunity to undertake this doctoral programme and for his constant and thoughtful guidance throughout the entire research work.

I would also like to express my sincere gratitude to Professor Lorenzo Masia for hosting me at the ARIES laboratory, first at Heidelberg University and subsequently at the Technical University of Munich. The experiences gained in these research environments were fundamental to the development of the present work.

A special thanks goes to Francesco and to the entire research group in Germany for their warm welcome, collaboration, and technical and scientific support, which significantly contributed to the successful completion of this research.

I would like to thank Elio for his contribution during the initial stages of the work, and Simone for his support during the final phase of the research.

I am deeply grateful to Marina for encouraging me to embark on this path and for her support during the most challenging moments.

Finally, I would like to thank my family: my parents, for their constant support and trust in every choice I have made, and my sisters, for their continued closeness and encouragement.

Abstract

Upper limb motor impairments affect millions of individuals worldwide, with stroke survivors experiencing persistent functional limitations that reduce independence in daily activities. Despite advances in rehabilitation robotics, current technologies face key limitations: predominantly single-joint assistance that does not preserve natural coordination patterns, configuration-dependent force measurement in cable-driven systems, and the lack of systematic design frameworks integrating biomechanical and engineering requirements.

This dissertation presents a systematic design methodology for upper limb rehabilitation exoskeletons, validated through the development of a coordinated shoulder-elbow cable-driven exosuit. The methodology integrates Product Design Specifications (PDS), Multi-Criteria Decision Making (MCDM), mathematical modeling, and iterative validation. Its application to a three-degree-of-freedom case study demonstrates structured exploration of design alternatives and traceable decision-making.

The proposed exosuit introduces a motor-proximal sensing architecture, relocating force measurement from cable anchor points to actuation units. This enables coordinated multi-joint assistance across shoulder and elbow movements while preserving functional range of motion. The approach addresses the trade-off between measurement accuracy and operational workspace typical of cable-driven systems.

Experimental validation with human subjects (n=5) shows reduced muscle activation during assisted movements, preservation of natural kinematic coordination, and reliable force sensing. The system achieves a total mass of 3.3 kg, supporting portable and self-wearable use. A complementary camera-based validation method enables accessible performance assessment, particularly in resource-constrained settings.

These contributions demonstrate how a systematic design methodology, combined with enabling technological solutions, can address key challenges in multi-joint coordination, sensing reliability, and reproducible development in rehabilitation robotics.

Table of contents

List of figures

List of tables

Nomenclature

Roman Symbols

d	Cohen's d effect size measure (dimensionless)
D_1	Damping coefficient for shoulder admittance control [Nms/rad]
D_2	Damping coefficient for elbow admittance control [Nms/rad]
deg	Degrees (angular measurement)
EMG_{RMS}	Root Mean Square of Electromyographic Signal [V]
$\mathbf{F}$	Force vector [N]
F_{cable}	Cable tension force [N]
F_{max}	Maximum admissible cable tension [N]
g	Gram (mass unit)
H	User height [mm]
Hz	Hertz (frequency unit)
$J(\alpha)$	Jacobian matrix relating cable displacement to shoulder elevation angle: $\partial k/\partial \alpha$
$Jerk$	Third derivative of position (movement smoothness metric) [m/s³]
$k(\alpha)$	Cable displacement as function of shoulder elevation angle [m]
kg	Kilogram (mass unit)
K_l	Biomechanical constant: $K_l = m_l \cdot L_{Gl}$ [kg·m]
kPa	Kilopascal (pressure unit)
K_{ul}	Biomechanical constant: $K_{ul} = m_{ua} \cdot L_{Gu} + m_l \cdot L_u$ [kg·m]
$\mathscr{L}$	Lagrangian function: $\mathscr{L} = T - V$ [J]
L_{fa}	Forearm length (elbow-wrist; Radiale to Stylion landmark) [mm]
L_h	Hand length (Mid-stylion to Dactylion landmark) [mm]

L_{ua}	Upper arm length (shoulder-elbow; Acromiale to Radiale landmark) [mm]
$\mathbf{M}(\mathbf{q})$	Generalized mass matrix [kg, kg·m²]
m_{body}	Total body mass [kg]
m_{fa}	Forearm mass [kg]
m_{ua}	Upper arm mass [kg]
$\%MVC$	Percentage of Maximum Voluntary Contraction
n	Number of measured marker positions in dataset
N_A	Number of design alternatives in MCDM
N_C	Number of evaluation criteria in MCDM
Nm	Newton-meter (torque unit)
p	Probability value for statistical significance (dimensionless)
$\mathbf{q}$	Generalized coordinates vector
$\mathbf{Q}$	Generalized applied forces vector [N, Nm]
$\ddot{\mathbf{q}}$	Generalized accelerations vector [various units]
$\dot{\mathbf{q}}$	Generalized velocities vector [various units]
$\mathbf{r}$	Position vector [m]
R^2	Coefficient of determination (dimensionless)
r_{avg}	Mean radius quantifying point cloud dispersion [mm]
r	Correlation coefficient (dimensionless)
R_{iy}	Rating of alternative y for criterion i
r_{MA}	Moment arm length [mm]
$Score_y$	Overall MCDM score for alternative y
T	Kinetic energy [J]
t	t-statistic for hypothesis testing (dimensionless)
V	Potential energy [J]
W_{C_i}	Weight of criterion i in MCDM evaluation
x_c, y_c	Mean center coordinates of marker distribution [pixels]
x_i, y_i	Pixel coordinates of measured marker position i [pixels]
z_l	Vertical coordinate of forearm center of mass in world frame [m]
z_u	Vertical coordinate of upper arm center of mass in world frame [m]

Greek Symbols

α	Shoulder elevation angle (sagittal plane) [rad]; Significance level for statistical analysis
β	Arm longitude angle (frontal plane) [rad]
η_{trans}	Transmission efficiency (dimensionless)
γ	Shoulder internal/external rotation [rad]
λ	Lagrange multipliers vector
ω	Angular velocity vector [rad/s]
Φ	Constraint equations vector
ϕ_1	Euler angle: rotation about X-axis (roll) for upper arm orientation [rad]
ϕ_2	Euler angle: rotation about Y-axis (pitch) for upper arm orientation [rad]
ϕ_3	Euler angle: rotation about Z-axis (yaw) for upper arm orientation [rad]
$\Phi_{\mathbf{q}}$	Jacobian matrix of constraints
$\Phi_{\mathbf{qq}}$	Hessian tensor of constraints
τ	Joint torque vector [Nm]
τ_i	Interaction torque measured from load cell signals via geometric compensation [Nm]
τ_{max}	Maximum joint torque [Nm]
τ_r	Reference torque for gravity compensation control [Nm]
θ	Elbow flexion angle [rad]

Subscripts

Abd/Add	Abduction/Adduction movement
AD	Anterior Deltoid
BB	Biceps Brachii
Circum.	Circumduction movement
Elev/Depr	Elevation/Depression movement
Flex/Ext	Flexion/Extension movement
MD	Medial Deltoid
MR/LR	Medial/Lateral Rotation
P	Planar joint (physiological DoF classification)

Pro/Sup	Pronation/Supination movement
Prot/Retr	Protraction/Retraction movement
Rad/Uln	Radial/Ulnar deviation
R	Rotary joint (physiological DoF classification)
S	Spherical joint (physiological DoF classification)

Acronyms / Abbreviations

ADL	Activities of Daily Living
AF	Application Field
AK60-6	T-Motor quasi-direct drive brushless DC motor (rated torque 6 Nm)
ALS	Amyotrophic Lateral Sclerosis
ANOVA	Analysis of Variance
BLE	Bluetooth Low Energy wireless protocol
BMI085	Bosch 6-axis inertial measurement unit (3-axis accelerometer + 3-axis gyroscope)
BOA	BOA Fit System (micro-adjustable ratchet closure)
BOM	Bill of Materials
CAD	Computer-Aided Design
CAE	Computer-Aided Engineering
CAN	Controller Area Network communication bus
COTS	Commercial Off-The-Shelf
CRA	Clinical Rehabilitation Assistance
DAE	Differential-Algebraic Equations
DB	DataBase
DC	Direct Current (motor type)
DFA	Design for Assembly
DFM	Design for Manufacturing
DoF	Degrees of Freedom
DTM	Dart-Throwing Motion
EC	Electronically Commutated (motor type)
EEG	Electroencephalography

EMG	Electromyography
FDM	Fused Deposition Modeling
FRoM	Functional Range of Motion
FSR	Force-Sensing Resistors
GA	Gravity Assistance
GC	Gravity Compensation
HRA	Home Rehabilitation Assistance
HX711	24-bit analog-to-digital converter for load cell signal conditioning
IAER	Industrial Assistance for Effort Reduction
IMU	Inertial Measurement Unit
LED	Light-Emitting Diode (illumination system)
LSD	Least Square Distance (postural stability merit index)
MCDM	Multi-Criteria Decision Making
MVC	Maximum Voluntary Contraction
N.A.	Not Available
nRF52840	Nordic Semiconductor Bluetooth 5.0 System-on-Chip microcontroller
ODE	Ordinary Differential Equations
OTM	One-To-Many (actuation paradigm)
PAM	Pneumatic Artificial Muscle
PDS	Product Design Specifications
P.I.	Performance Index (normalized stability metric)
PRRRP	Prismatic-Revolute-Revolute-Revolute-Prismatic kinematic chain
PTFE	Polytetrafluoroethylene (Teflon) low-friction cable liner material
RMSE	Root Mean Square Error
RMS	Root Mean Square
RoM	Range of Motion
RSPA	Reinforced Soft Pneumatic Actuators
SEA	Series Elastic Actuator
sEMG	Surface Electromyography
SMA	Shape Memory Alloy

SOA	Soft Origami Actuators
SVD	Singular Value Decomposition
TCAM	Twisted and Coiled Artificial Muscles
TPU	Thermoplastic Polyurethane
TRL	Technology Readiness Level
VO_2	Oxygen consumption (metabolic assessment)
WSR	Wearable Soft Robots

Introduction

I.1 Clinical Context and Rehabilitation Challenges

Upper limb motor impairments affect millions of individuals annually worldwide [1; 2], with stroke representing the leading cause in developed nations. Stroke affects approximately 795,000 individuals annually in the United States alone, with 77–85% of survivors experiencing persistent upper limb dysfunction affecting activities of daily living [1]. The resulting functional limitations (reduced independence in self-care, diminished occupational capacity, compromised social participation) impose significant burdens on individuals, caregivers, and healthcare systems [2].

Rehabilitation robotics emerged as a technological response to this clinical challenge, offering potential for intensive, repeatable, task-specific training at scales unachievable through manual therapy alone [3–5]. However, translation from laboratory prototypes to clinical practice remains limited. Current upper limb exoskeletons face fundamental constraints: isolated single-joint assistance that fails to support coordinated functional movements (systematic reviews report 60–70% of devices target single joints only [6]), configuration-dependent sensing limitations that restrict operational workspace [7], and portability-functionality trade-offs that compromise either assistance effectiveness or practical wearability. These limitations reflect not only technical challenges but also the absence of systematic design frameworks integrating biomechanical requirements, user needs, and engineering constraints [8].

The field requires coordinated multi-joint assistance architectures that preserve natural movement synergies essential for functional tasks, sensing configurations maintaining measurement accuracy across extended operational ranges necessary for activities of daily living, and validated design methodologies enabling reproducible development of clinically effective, practically deployable rehabilitation technologies.

I.2 Research Objectives and Scientific Contributions

This thesis addresses identified limitations through integrated development of systematic methodology and innovative technical solutions for coordinated multi-joint rehabilitation assistance. Three interconnected research objectives structure the investigation:

Objective 1: Develop and validate a systematic design methodology specifically adapted for rehabilitation exoskeleton development, integrating Product Design Specifications, multi-criteria decision making, and iterative validation protocols to enable reproducible exploration of design alternatives while explicitly addressing trade-offs between competing requirements (functionality, portability, clinical viability).

Objective 2: Design and experimentally validate a coordinated multi-joint cable-driven exoskeleton providing simultaneous 3-DOF assistance (shoulder flexion/extension, abduction/adduction, elbow flexion/extension) with preserved functional range of motion (0–90° across all DOF) and clinically meaningful muscle activation reduction during activities of daily living.

Objective 3: Develop a novel motor-proximal sensing architecture resolving the fundamental ROM-accuracy trade-off in cable-driven systems, enabling coordinated multi-joint assistance with maintained force measurement precision across extended operational ranges necessary for functional rehabilitation tasks.

The thesis delivers three primary contributions validated through systematic analysis and human subject experimentation:

- Contribution 1 - *Systematic Design Methodology (Chapter 2)*
  A structured framework integrating requirements definition, multi-criteria decision making, mathematical modeling, and validation protocols, demonstrated through application to coordinated shoulder-elbow exoskeleton development. The methodology provides explicit guidance for systematic design space exploration, quantitative alternative evaluation, and iterative refinement based on objective performance criteria.

- Contribution 2 - *Coordinated Shoulder-Elbow Exoskeleton (Chapters 3-4)*
  A lightweight (less than 4 kg) self-wearable cable-driven system providing coordinated 3-DOF assistance with preserved functional workspace. Developed at Heidelberg University and validated at Technical University of Munich with human subjects (n=5), demonstrating statistically significant muscle activation reduction (18.4% average, up to 27.7% medial deltoid, p=0.012) while maintaining natural kinematic coordination (R^2=0.64–0.82) during functional tasks.

- Contribution 3 - *Motor-Proximal Sensing Architecture (Chapters 3-4)*
  Novel force sensing configuration relocating load cells from anchor points to motor-proximal positions, resolving spatial interference constraints that limit traditional cable-driven systems to single-joint operation. Validated measurement accuracy (R^2=0.75, RMSE=1.51 Nm across 6.2M samples) enables coordinated multi-joint assistance with maintained force-based control precision throughout extended operational ranges (0–90° elevation).

These contributions advance rehabilitation robotics by demonstrating integration of systematic methodology with technical innovations addressing fundamental limitations in multi-joint coordination, sensing precision, and practical deployment feasibility.

I.3 Thesis Structure Overview

The thesis is organized in five chapters documenting systematic progression from problem identification through validated solution implementation:

Chapter 1 - State of the Art presents comprehensive analysis of upper limb rehabilitation technologies through systematic literature review (n=120 devices), identifying current capabilities, persistent limitations, and specific research gaps motivating thesis contributions. Quantitative device analysis establishes baseline performance characteristics and coordination constraints in existing systems.

Chapter 2 - Systematic Design Methodology develops the structured framework integrating Product Design Specifications, Multi-Criteria Decision Making, mathematical modeling, and validation protocols. The methodology addresses reproducibility challenges in rehabilitation device development through explicit quantification of design trade-offs and systematic alternative evaluation.

Chapter 3 - Case Study Application demonstrates methodology implementation through coordinated shoulder-elbow exoskeleton development. Detailed documentation covers requirements definition, MCDM-based concept selection, kinematic/dynamic modeling, CAD design integration, control system implementation, and prototype realization, illustrating translation from specifications to functional hardware.

Chapter 4 - Experimental Validation presents human subject trials (n=5) quantifying system performance through kinematic accuracy, muscle activation reduction, and functional task completion metrics. Motor-proximal sensing validation establishes accuracy characteristics across operational workspace, confirming enabling capability for coordinated multi-joint assistance.

Chapter 5 - Cost-Effective Validation explores camera-based motion tracking as accessible alternative for performance assessment, demonstrating methodology applicability through passive exoskeleton case study. The chapter establishes complementary validation frameworks adaptable to resource-constrained research environments.

The thesis concludes with synthesis of contributions, clinical implications, and directions for future research extending validated principles to broader rehabilitation applications.

Chapter 1

State of art and Problem Statement

Upper limb dysfunction represents one of the most prevalent and debilitating consequences of neurological injuries and musculoskeletal disorders, significantly impacting quality of life and functional independence [2]. Stroke affects approximately 795,000 individuals annually in the United States, with 80% experiencing persistent upper limb dysfunction that limits their ability to perform activities of daily living [1]. Traditional rehabilitation approaches, while foundational to therapeutic practice, face significant limitations in providing the intensive, repeatable, and personalized interventions required for optimal motor recovery [3; 8].

The emergence of robotic rehabilitation technologies has created unprecedented opportunities to address these limitations through systematic, technology-assisted therapeutic interventions [4; 5]. However, despite significant advances in rehabilitation robotics, fundamental challenges persist in developing devices that effectively balance technical performance with clinical usability, particularly for multi-joint coordination and portable assistance applications [6; 9]. This chapter establishes the foundational understanding of upper limb rehabilitation technologies through comprehensive literature analysis, systematic technical evaluation of existing devices, and identification of critical research gaps that motivate the work presented in this thesis.

1.1 Upper Limb Anatomy and Functional Requirements

1.1.1 Anatomical Foundation for Rehabilitation Device Design

The human upper limb (Figure 1.1) represents a complex bio-mechanical structure involving bones and joints actuated by muscles, enabling versatile and precise movements during human interactions with the external environment [10; 11]. Understanding the nuances

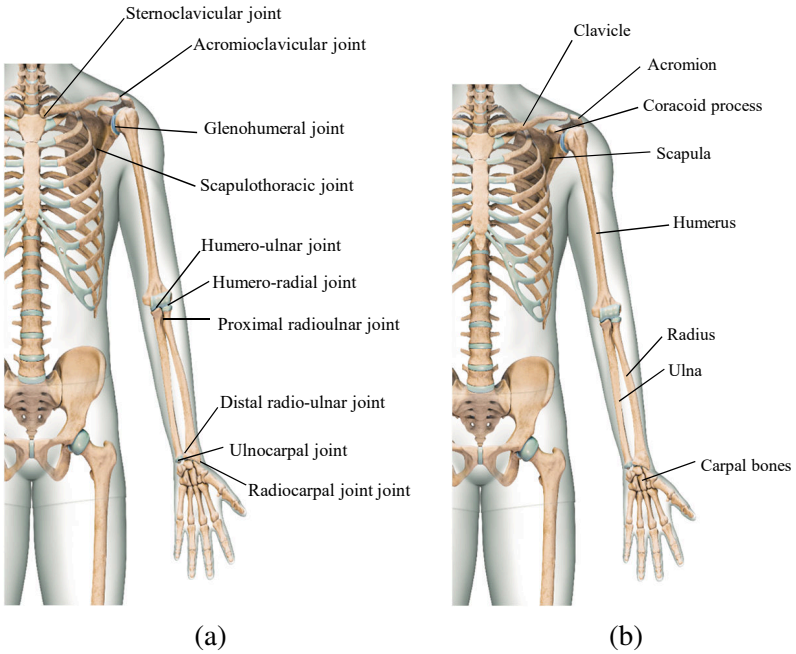

Figure 1.1 Human upper limb anatomy showing (a) joint articulations and (b) bone structure. The complex arrangement of joints enables versatile movement patterns essential for activities of daily living.

of upper limb articulations and their relative motions is essential for accurate design and development of wearable robotic devices.

The upper limb articulation begins at the shoulder girdle, where the clavicle (collarbone) and scapula (shoulder blade) form a complex junction known as the acromioclavicular joint. This joint allows the elevation, depression, protraction, and retraction of the shoulder. The humerus articulates with the scapula at the glenohumeral joint. This ball-and-socket joint provides an extensive range of motion, including flexion, extension, abduction, adduction, and internal/external rotation of the arm. The forearm comprises two bones, the radius and ulna, which articulate with the humerus at the humero-ulnar and humero-radial joints for elbow flexion and extension. Radius and ulna articulate each other at the proximal radio-ulnar and distal radio-ulnar joints which facilitates pronation (turning the palm downward) and supination (turning the palm upward) of the forearm. The wrist, composed of multiple small bones called carpals, articulates with the distal ends of the radius and ulna through radiocarpal and ulnocarpal joints. This complex joint allows flexion, extension, abduction, adduction, and circumduction of the hand. Each joint of the upper limb has its particular motions and RoMs.

1.1.2 Range of Motion Requirements for Functional Tasks

Each joint of the upper limb has specific motion capabilities and ranges of motion that must be considered in exoskeleton design. Figure 1.2 provides a comprehensive overview of the maximum ranges of motion for all major upper limb joints, establishing the kinematic requirements that rehabilitation devices must accommodate.

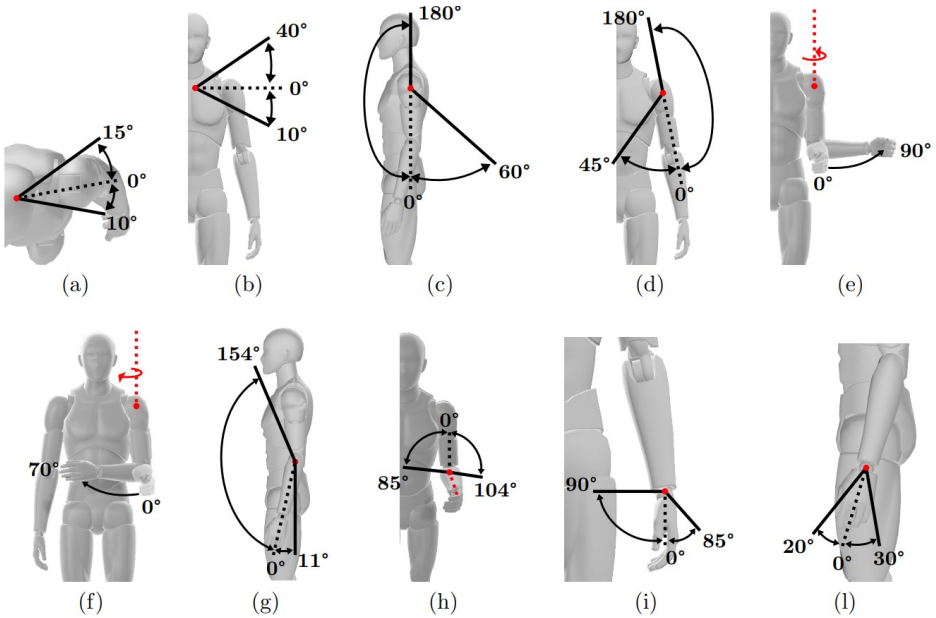

Figure 1.2 Maximum ranges of motion (ROM) for upper limb joints: (a) Shoulder retraction/protraction; (b) Shoulder elevation/depression; (c) Shoulder flexion/extension; (d) Shoulder abduction/adduction; (e) Shoulder external rotation; (f) Shoulder internal rotation; (g) Elbow flexion/extension; (h) Elbow pronation/supination; (i) Wrist flexion/extension; (l) Wrist radial/ulnar deviation.

The distinction between maximum Range of Motion (ROM) and Functional Range of Motion (FRoM) is critical for rehabilitation device design. While ROM represents the complete anatomical movement capability of each joint, FRoM defines the minimum angular excursions required to perform activities of daily living effectively. Rehabilitation interventions prioritize recovery of FRoM as the primary therapeutic objective, as restoring functional ranges enables patients to regain independence in self-care tasks even when complete anatomical ROM recovery remains unattainable [12; 13].

Table 1.1, summarizes the maximum RoMs and the FRoMs for each articulation [11; 14–18]. The main goal of the rehabilitation process is to guarantee that patients recover at least the FRoM to be capable of performing normal ADLs. Some studies [12; 13; 19] showed that the FRoMs for ADLs lower motion ranges are required.

Table 1.1 Maximum RoMs and FRoMs for upper limb articulations.

	Motion type	Max RoMs	FRoMs	Fig.
Shoulder	Protraction	0°:10°	NA	1.2(a)
	Retraction	0°:15°	NA	
	Elevation	0°:40°	NA	1.2(b)
	Depression	0°:10°	NA	
	Flexion	0°:180°	0°:92°	1.2(c)
	Extension	0°:60°	0°:38°	
	Abduction	0°:180°	0°:40°	1.2(d)
	Adduction	0°:45°	0°:20°	
	External Rot.	0°:90°	0°:22°	1.2(e)
	Internal Rot.	0°:70°	0°:64°	1.2(f)
Elbow	Flexion	0°:154°	0°:125°	1.2(g)
	Extension	0°:11°	0°:0°	
	Pronation	0°:85°	0°:20°	1.2(h)
	Supination	0°:104°	0°:13°	
Wrist	Flexion	0:90	0:24	1.2(i)
	Extension	0°:70°	0°40°	
	Radial Dev.	0°:20°	0°:18°	1.2(l)
	Ulnar Dev.	0°:30°	0°:18°	

Ensuring and enhancing the functional ranges of motion in joints is essential for normal upper limb function, and it is a common objective in rehabilitation and physical therapy programs. When delving into the modelling and design of wearable robots intended to interact with the upper limb, it is imperative to scrutinize statistical data related to mean anthropometric values. Referring to Fig. 1.3, to correctly identify the characteristic lengths of the upper limb, the standards for anthropometry assessment [20] indicate several surface landmarks, the acromiale landmark(A) for the shoulder, the radiale landmark (R) for the elbow, the Stylion (S) and Mid-stylion (M) landmarks for the wrist and the dactylion landmark (D) for the hand. These landmarks are identifiable skeletal points that are found by palpation and must be identified before any subject measurements are made. The knowledge of these critical points plays a fundamental role for the ergonomic design and for the mechanical connection between the wearable device and the patient. The distance between A-R, R-S and M-D landmarks represent, respectively, the length of the upper arm (L_{ua}), forearm (L_{fa}) and hand (L_h). This standardization in anthropometric parameters estimation allows to obtain statistical values for the characteristic lengths of the upper limb. It is to be noticed that these mean values can vary based on ethnicity, age, and gender.

Table 1.2 illustrates the mean values of upper limb segments for European adults [21]. It's important to note that ROMs and lengths can vary from person to person due to factors

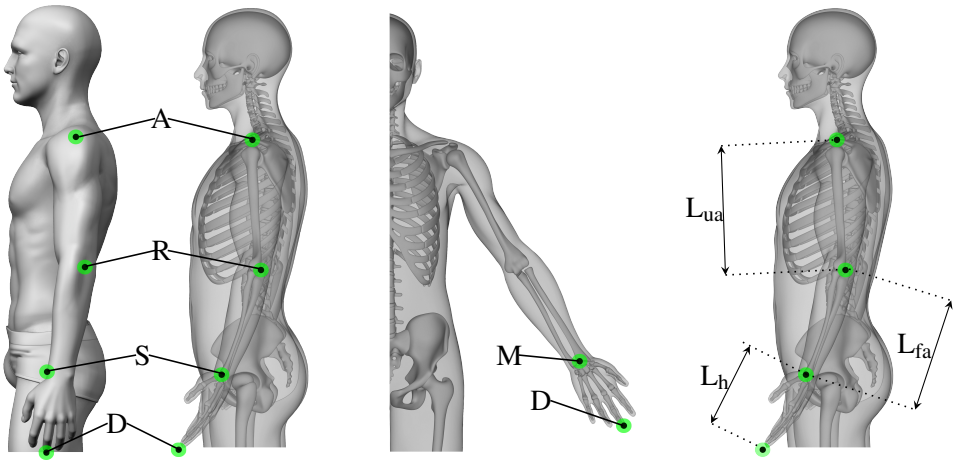

(a) (b)

Figure 1.3 Landmarks (a) for Upper limb lengths (b) evaluation.

such as age, genetics, and previous injuries. Once the mean values of ranges of motion for the upper limb joints and the mean length of bones are known it is possible to start the designing process of a wearable robotic device for upper limb rehabilitation. In this paper, a systematic approach based on the above-mentioned key parameters is proposed to achieve a systematic conceptualization, design, simulation and testing of a soft wearable robotic device.

Table 1.2 Mean lengths values and standard deviation of arm and forearm of European adults.

	L_a	L_{fa}
Male	33.4±1.58 cm	24.6±1.25 cm
Female	30.±1.59 cm	22±1.03 cm

1.2 Systematic Literature Review Methodology

1.2.1 Review Framework and Structured Approach

A systematic literature review approach was implemented to obtain a comprehensive understanding of the current state of the art in upper limb rehabilitation devices. This methodology follows established systematic review protocols to ensure comprehensive coverage of relevant technologies while maintaining scientific rigor in the analysis process.

The systematic review process employed a structured approach consisting of multiple sequential phases designed to identify, filter, and analyze the most relevant literature. Figure 1.4 illustrates the comprehensive methodology employed in this research, demonstrating the

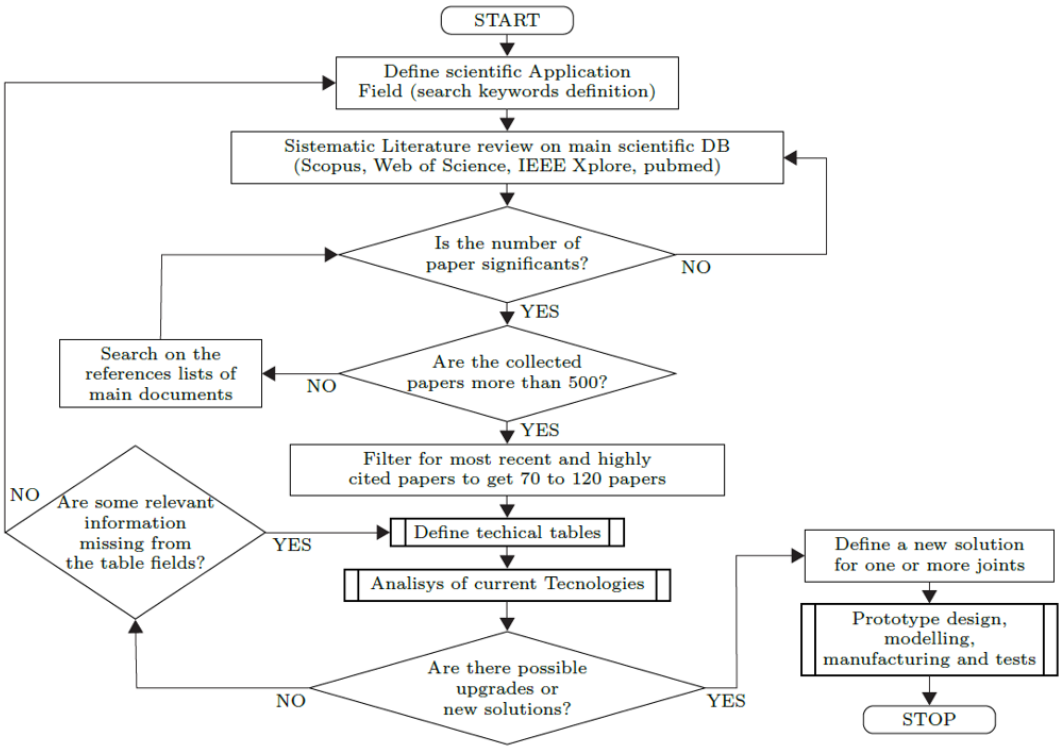

Figure 1.4 Systematic literature review flowchart showing the sequence of steps taken to identify the most important documents for comprehensive state-of-the-art analysis.

sequence of steps taken to progress from initial keyword definition through final technology analysis.

The first step involves defining the specific application field and establishing meaningful keywords for database searches. A crucial following point is defining a set of meaningful keywords to be used in paper searches across main scientific databases including Scopus, Web of Science, IEEE Xplore, and PubMed. The correct choice of keywords allows limiting search results to the most significant outcomes for the specific application field.

This systematic methodology, detailed in the associated review paper [22], enables reproducible identification of technological trends and persistent limitations. The structured approach ensures that gap analysis is grounded in comprehensive evidence rather than selective observation, providing robust foundation for identifying innovation opportunities that address real clinical needs rather than purely technical challenges.

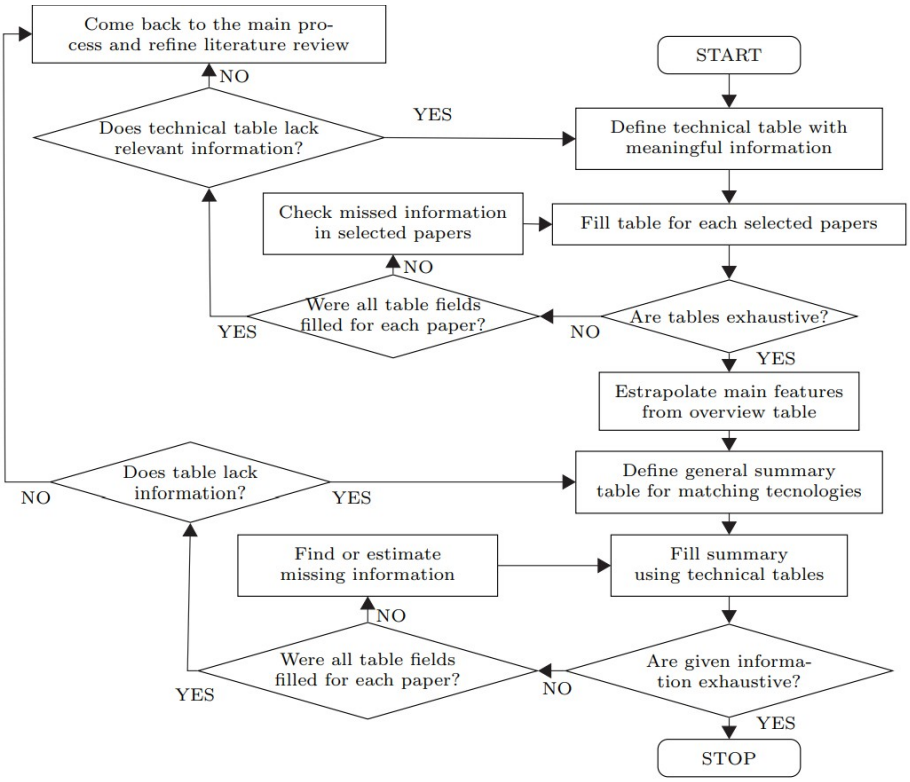

Figure 1.5 Flowchart describing the systematic procedure for defining the technical analysis tables.

1.2.2 Technical Analysis Framework Development

Using the systematic approach illustrated in Figure 1.5, it became possible to define specific and exhaustive tables to summarize and analyze the main features of existing devices and current research trends of the international scientific community. The proposed technical analysis framework presents six main evaluation areas for each device under consideration.

The structured technical tables capture comprehensive device information including prototype identification, visual documentation through photographs and schematics, general parameters (DoFs, TRL, weight), mechanical characteristics (involved anatomical parts, range of motion, maximum torque), implementation details (materials, sensors, actuators), and application context (field, advantages, disadvantages).

Degrees of Freedom Classification

Since the focus of this work is to propose an innovative and systematic method to guide designers in the initial phase of wearable robot design, the classification of existing robots was not made according to the number of their mechanical degrees of freedom. Instead,

the classification was done according to the number and types of physiological DoFs that a wearable device is able to actuate or assist on the upper limb.

This physiological DoF classification approach recognizes that the required mobility of the human upper limb is a design specification of paramount importance for wearable robots. Figure 1.6 illustrates the three primary joint types: rotary (R) joints providing rotational motion about a single axis, planar (P) joints enabling motion within a plane, and spherical (S) joints allowing rotation about multiple axes. For example, a device actuating elbow flexion/extension and pronation/supination is categorized as having two DoFs with type RR (two rotary joints).

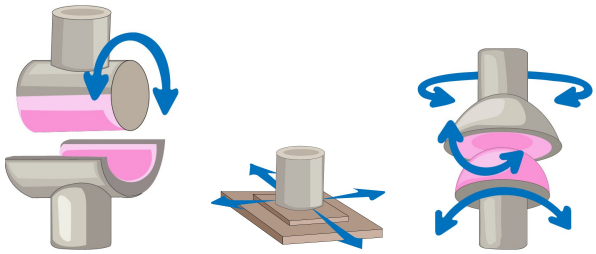

Figure 1.6 Types of joints in upper limb exoskeletons: (a) rotary joints, (b) planar joints, (c) spherical joints.

Overview of Sensing Technologies

Sensing technologies enable human-robot interaction and closed-loop control implementation in rehabilitation devices. Analysis of current implementations reveals three dominant sensing modalities employed across the analyzed devices: force/torque measurement systems, kinematic sensing approaches, and encoder-based position feedback integrated with actuation units.

Force Measurement Systems: Load cells represent the primary force sensing approach in cable-driven devices, providing direct measurement of cable tension for force-based control strategies [23]. The systematic analysis reveals that 15 of 24 devices employ load cell configurations for force feedback, reflecting the maturity and reliability of this sensing approach for rehabilitation applications. Alternative force sensing implementations include series elastic actuators, which integrate compliant elements within the actuation chain enabling force measurement through deflection sensing while providing inherent safety benefits [24].

Kinematic Sensing: Inertial Measurement Units (IMUs) have emerged as the preferred solution for capturing body segment kinematics in wearable rehabilitation devices [25]. These wireless sensor networks provide three-dimensional orientation data through quaternion representation, enabling real-time movement tracking without constraining natural motion. Modern implementations typically operate at 100 Hz acquisition frequencies with Bluetooth Low Energy communication protocols, supporting coordinated multi-joint assistance strategies through distributed sensor placement across multiple body segments.

Position Feedback: Rotary encoders integrated directly with motor shafts provide high-resolution position feedback for closed-loop motor control. This sensing modality appears universally across motorized devices, enabling precise actuation control and supporting implementation of position-based assistance strategies complementary to force-based approaches.

Biological Signals: Surface Electromyography (sEMG) integration enables intention detection through muscle activation pattern analysis [23]. However, only 3 of the analyzed devices implement sEMG-based control, indicating persistent challenges in signal reliability, electrode placement consistency, and long-term stability that limit widespread adoption despite potential advantages in intuitive control implementation.

The sensing architecture selection directly impacts achievable control strategies, with force-based admittance control requiring reliable load cell measurements, while kinematic-based approaches depend on accurate IMU data for assistance coordination across multiple joints.

Control Architecture Overview

Control architectures for upper limb rehabilitation devices commonly adopt hierarchical structures balancing safety, responsiveness, comfort, and therapeutic efficacy [26; 27]. Modern systems typically employ multi-layer control, separating high-level planning from low-level execution while maintaining continuous safety monitoring.

Safety – Critical Layer: Hardware emergency stops, force limits, and redundant sensing operate independently of functional control loops to detect failures, workspace violations, and excessive interaction forces. Compliance with ISO 13482 requires enforcing limits on forces, workspace boundaries, and shutdown protocols across all layers [28].

Assistance Control Strategies: The functional layer provides therapeutic assistance through force- or position-based approaches. Admittance control adjusts impedance based on interaction forces, supporting user-guided movement and effective gravity compensation [29]. Impedance control instead regulates force output from kinematic measurements using

virtual springs and dampers [30]. Assist-as-needed methods modulate support to promote active participation while preventing task failure [31].

Biomechanical Modeling: Personalized parametric limb models enable gravity compensation adapted to user anthropometry and joint configuration [32]. Real-time kinematic data from IMU networks continuously updates gravitational torque estimates during multi-DoF movements.

Adaptive Control: Rehabilitation requires controllers that evolve with user capability [33]. Adaptation algorithms adjust assistance, impedance, and workspace limits using performance metrics from repeated tasks. Learning-based approaches offer individualized control strategies, though complexity and long-term stability currently limit clinical deployment.

The chosen control architecture directly affects therapeutic outcomes: force-based strategies depend on reliable interaction sensing, whereas position-based methods require precise kinematic measurements over extended ranges.

Technology Readiness Level Assessment

The Technology Readiness Level (TRL) parameter of existing devices must be considered to analyze current research trends [34]. TRL is a metric used to assess the maturity and readiness of a technology or innovation for practical application or commercialization. TRL levels are typically numbered from 1 to 9, with each level representing a specific stage of technological readiness and development. Assessing TRL for each device allows providing a detailed picture of technological advancement in the field and for specific solutions.

Proposing a synthetic product description table

The proposed technical tables (Tables 1.3 and 1.4) provide systematic documentation of exoskeleton characteristics through six structured areas. Each entry includes prototype identification (author-assigned name or user-defined nomenclature for cross-referencing), visual documentation through photographs and schematic diagrams facilitating device recognition, and general parameters documenting distinctive technical characteristics. This structured format enables comparative analysis of existing devices and identification of research trends within the international scientific community.

Table 1.3 Technical table for paper "Dynamic Closed Loop Platform for Elbow Flexion".

Prototype Name
Dynamic Closed Loop Platform for Elbow Flexion

DoFs	Type of DoFs	Patented	Clinical Assessed	Weight	TRL	Limb Side		Portable
1	R	☐	☐	N.A.	3	☑ Left	☑ Right	☑

Picture

Device Schematic

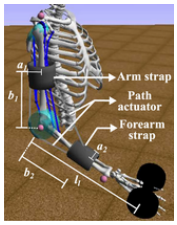

Involved anatomic parts	Involved articulations	Allowed motion	RoM Min	RoM Max	Max torque
☐ Shoulder	☐ Acromioclavicular joint (clavicle→acromion) ☐ Glenohumeral joint (glenoid→humerus) ☐ Sternoclavicular joint (sternum→clavicle) ☐ Scapulothoracic joint (scapula→thorax)	☐ Flexion ☐ Extension ☐ Abduction ☐ Adduction ☐ Lateral Rotation ☐ Medial Rotation ☐ Elevation/Depression ☐ Protraction/Retraction			
☑ Elbow	☑ Humeroulnar joint (humerus→ulna) ☑ Humeroradial joint (humerus→radius) ☐ Proximal Radioulnar joint (radio→ulna)	☑ Flexion ☐ Extension ☐ Pronation ☐ Supination	0°	90°	12Nm
☐ Wrist	☐ Radiocarpal joint (radius→scaphoid/lunate) ☐ Ulnocarpal joint (ulna→lunate/triquetral) ☐ Radioulnar joint (radio→ulna	☐ Flexion ☐ Extension ☐ Abduction ☐ Adduction ☐ Circumduction			

Materials	Fixing system	Sensors	Actuators	Modelling
Fabric and straps Bowden cables	Velcro straps	virtual human model	DC motors	Kinematic and Dynamic

Application Field	Advantages	Drawbacks
IAER	Active-passive operation mode Activation based on muscle activation model	No cable tension feedback No force/torque feedbacks

Table 1.4 Technical table for paper "Exo-Wrist: A Soft Tendon-Driven Wrist-Wearable Robot With Active Anchor for Dart-Throwing Motion in Hemiplegic Patients".

Prototype Name
Exo-Wrist

DoFs	Type of DoFs	Patented	Clinical Assessed	Weight	TRL	Limb Side		Portable
2	RR	☐	☐	1003 grams	4	☑ Left	☑ Right	☑

Picture

Device Schematic

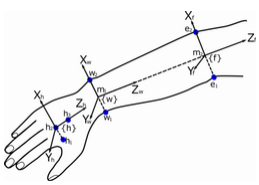

Involved anatomic parts	Involved articulations	Allowed motion	RoM Min	RoM Max	Max torque
☐ Shoulder	☐ Acromioclavicular joint (clavicle→acromion) ☐ Glenohumeral joint (glenoid→humerus) ☐ Sternoclavicular joint (sternum→clavicle) ☐ Scapulothoracic joint (scapula→thorax)	☐ Flexion ☐ Extension ☐ Abduction ☐ Adduction ☐ Lateral Rotation ☐ Medial Rotation ☐ Elevation/Depression ☐ Protraction/Retraction			
☐ Elbow	☐ Humeroulnar joint (humerus→ulna) ☐ Humeroradial joint (humerus→radius) ☐ Proximal Radioulnar joint (radio→ulna	☐ Flexion ☐ Extension ☐ Pronation ☐ Supination			
☑ Wrist	☑ Radiocarpal joint (radius→scaphoid/lunate) ☑ Ulnocarpal joint (ulna→lunate/triquetral) ☑ Radioulnar joint (radio→ulna)	☑ Flexion ☑ Extension ☑ Abduction ☑ Adduction ☐ Circumduction	0° 0° 0° 0°	50° 50° 20° 20°	N.A. N.A. N.A. N.A.

Materials	Fixing system	Sensors	Actuators	Modelling
Fingerless golf glove Plastic Wrist Ring Silicone pads Plastic Forearm anchor	Active forearm anchor 3D-printed custom wrist armlet	Load Cell LSB200 3D motion-capture EMG sensor Incremetal Encoders	IG-32Gm motors	Kinematic and Dynamic

Application Field	Advantages	Drawbacks
HRA CRA	Active forearm fixing system Adaptable to different forearm sizes Controlled fixing pressure	Need wrist ring customization

1.3 Comprehensive Analysis of Existing Technologies

1.3.1 Literature Analysis Results

The literature analysis focused primarily on soft exoskeletons, which typically are wearable devices with rigid external frameworks mixed with soft actuators, and exosuits, which are more flexible and soft wearable systems designed to assist and enhance the user's natural movements using textiles and lightweight materials.

A large number of papers was found in the first iteration of search activities using the following comprehensive set of keywords: "upper limb" AND rehabilitation OR exosuit OR exoskeleton OR "soft robot" OR "activities of daily living" OR assistance OR shoulder OR elbow OR wrist. This high number of papers was systematically reduced to 817 by selecting a range of six publication years between 2018 and 2023. By restricting searches to "Robotic Exoskeleton" and "Soft Robotics," a total of 77 papers were identified, from which 44 papers were chosen that contained all necessary information for technical analysis. These papers described 24 distinct wearable devices that met inclusion criteria for comprehensive evaluation (some papers presented multiple devices or variations, while others described the same device from different perspectives).

While rehabilitation is typically conducted in clinical or hospital settings, home therapy can be pivotal in the recovery process, addressing challenges such as limited resources and specialized equipment [35]. However, home therapy poses challenges related to space, loneliness, and reduced patient motivation. To address these challenges, soft wearable robotics emerges as a viable solution to control, monitor, and guide patients through their rehabilitation journey.

1.3.2 Classification Based on Physiological Degrees of Freedom

The systematic literature review established that rehabilitation devices can be most effectively classified according to the number and types of physiological degrees of freedom (DoFs) they actuate, rather than by mechanical complexity [22]. This physiological classification approach recognizes that the required mobility of the human upper limb represents a design specification of paramount importance for wearable rehabilitation robots.

Since the focus of this work is to propose an innovative and systematic method to guide designers in the initial phase of wearable robot design, the classification of existing robots was not made according to the number of their mechanical degrees of freedom. Instead, the classification was done according to the number and types of physiological DoFs that

a wearable device is able to actuate or assist on the upper limb. The classification does not refer to the device, but to the achievable mobility of the human upper limb.

For example, a device providing elbow flexion/extension and pronation/supination assistance is classified as 2R (two rotary physiological DoFs) rather than by the number of mechanical actuators or linkages employed in the implementation.

Single Physiological DoF Devices

In [36] Rojo et al. introduced an exoskeleton using McKibben PAM and a 3D printed shoulder support brace for attachment and air supply, aiding in ADLs by partially achieving adduction/abduction motion within a range of 45.5°. The Myoshirt [37] is a textile exomuscle designed for supporting the shoulder against gravity, primarily applied in ADLs for individuals with impairments. Utilizing a textile interface and thorax harness for fixation, the device employs two artificial tendons actuated by a spring and a DC motor to transfer forces between a shoulder anchor and an upper arm anchor. The authors claim a 50% reduction in fatigue with gravity assistance. This device provides approximately 110° of limb extension and adduction, allowing other DoFs in the shoulder to move freely. It is classified as a 1 DoF device due to interdependent controlled motions. A soft robotic device for shoulder assistance in adduction/abduction was presented in [38]. Crafted from polyurethane fibers and a thin sealed sheet, this device, secured by a shoulder jacket and upper arm sleeves, achieves abduction and adduction motions through air chamber inflation and deflation. The authors claim a 35.45° arm abduction capability, but note significant jacket dislodging during inflation, causing proximal movement toward the head. Another shoulder assistive device ExoM-S is presented in [39]. ExoM-S, a passive rigid shoulder exoskeleton, employs a magnetic spring and custom locking mechanism to maintain shoulder posture during drilling tasks. With a connected balancing system, it enhances performance, reducing discomfort. Results show a substantial 976%-fold improvement in maintaining a fixed posture compared to the same unassisted tasks.

Most of one DoF wearable devices are employed for elbow actuation due to the lower mobility of its articulation and the greater simplicity in obtaining stable fixing points on the human limb. For example, a lightweight upper-limb cable-guided exosuit has been developed to assist users during lifting activities and the use of power tools [40]. The exosuit focuses on assisting elbow and shoulder flexion for both arms and allows passive movements in the transverse plane. This device was categorized one DoF because, although it actuates flexion and extension of shoulder and elbow for both left and right arms, these motions are not independent as they are both actuated using a single motor. The exosuit can reduce muscle

activation as measured by EMG signals, with reductions ranging from 24.6% to 64.6%. The types of movement allowed include lifting and releasing a load, holding a position, and manipulating a tool. The angle of movement is between 0 and 90°. In [41], a fabric muscle was designed for soft exosuits that provide upper limb assistance. The exosuits are designed to assist humans in performing tasks by supporting their muscle strength. The fabric muscles are attached to the biceps and triceps in an antagonistic structure, allowing for flexion and extension motion of the forearm up to 90° with a maximum torque of 3.89 Nm. The fabric muscles are made of light and flexible materials such as SMA actuators. An EMG sensor, specifically the sEMG sensor, is used to capture and record the electrical signals generated by the muscles. Sambhav et al [42] developed a simulation platform for studying the effect of soft-robotic wearables on human physiology. The platform focuses on elbow flexion augmentation using an upper limb exosuit model. It incorporates a GA controller and allows for closed-loop feedback control. The simulation platform enables the study of joint moments, muscle activations, and metabolic costs during a repetitive load lifting task. The exosuit model includes straps and force transmission systems. Copaci et al[43], proposed a robotic elbow wearable exoskeleton based on SMA wire actuators for elbow home rehabilitation aims. This device uses rigid parts for guiding three SMA Bowden cables that are fixed on the shoulder, bicep, forearm, wrist and hand, ensuring that the rotation center is right to the patient elbow joint. This robot allows to get a flexo-extension for elbow joint between 0 and 150° with a a frequency movement of 0.25 Hz while guaranteeing a maximum torque of 3.5 Nm. Carry[44] proposes a soft pneumatic elbow exoskeleton designed to assist in gripping and carrying loads. The exoskeleton uses a soft pneumatic actuation. The exoskeleton focuses on assisting the elbow joint, allowing movement and RoM in that area. It provides an assist torque of 7.2 Nm. The exoskeleton uses soft structures and a fabric human-machine interface to avoid rigid mechanical connections and mechanical joints. In terms of materials, the exoskeleton incorporates wearable soft actuators made of perpendicularly folded fabrics. Actuator pressure is used to generate the desired elbow assistance torque. Irshaidat et al [45] also proposed a wearable robot for ADLs to be self-wearable based on an extensor and a contractor McKibben PAM aiding the elbow to lift up to 1.5 kg in the range 30 to 90° for elbow flexo-extension. Xiloyannis et al. [7] have designed a soft exoskeleton on the arm to assist and improve elbow articulation. It is a cable exoskeleton, which uses internal tendons, Bowden cables, inextensible bands, 3-layer fabric, flexible plastic sheet covered with PE foam to construct the parts adhered to the human body. The exosuit is able to aid the wearer during movement (feeding condition) or non-feeding condition. The exosuit can compensate for gravitational forces while the RoM is limited to 90°, for safety reasons. Another device

actuating elbow flexion for both upper limbs using an underactuated mechanism with a OTM actuation paradigm was presented in [46]. This OTM device uses only one DC motor as the prime mover transmitting power through two clutchable modules via Bowden cables to the elbow. The fixing system is based on two anchors on upper arm and forearm connected with a rigid link and a rotational joint. This device is designed for gravity assistance and ADL applications and it allows to get an elbow flexion in the range of 0 and 90° with a maximum driving torque of 3.4 Nm. Authors asserted that this exosuit reduces the muscle effort of about 46.2%. In [47] authors present a soft robot using fabric-based pneumatic sleeves able to lift a 1.44 kg forearm rig up to 95° during elbow flexo-extension motion for assistive aims. This wearable device combines two shrink-to-fit pneumatic sleeves and a cable-driven actuator. The sleeves firstly are inflated to fix the robot to upper arm and forearm, afterwards transmission force thorough a cable-driven actuator is applied to perform arm flexion. After task completion, the sleeves are deflated releasing pressure on human arm. The proposed soft anchoring concept allows enhancing comfort and durability of wearable assistive devices. The STWR [48], developed by Park et al, is a wearable device based on a SFM actuator. Using SFMs and a BOA fixing system on the forearm this device is able to perform a flexo-extension up to 90° for assistive and ADL tasks. The authors integrated this device in a jacket to ensure an easy and fast wearing. A mannequin was used for assessing the capability of this robot to lift loads up to 4 kg. Salvatore et al.[49] proposed a novel hybrid exoskeleton named Cable Assistive Lifting Exoskeleton (CALE). This wearable device was designed to produce assistive force in industrial applications. The proposed design uses a cable-springs actuation combined with a direct actuation, both driven by DC motors. CALE actuates shoulder and elbow flexion through a custom gearbox that drives an actuation cable thorough a pulley, raising a glove-like support. Authors stated that this device can aid workers in repetitive lifting tasks with loads up to 10 kg. As previously asserted for [40], this device is considered as a one DoFs, since flexion and extension of the shoulder and elbow cannot be controlled independently.

An alternative to wearable exoskeletons was presented in [50], where a prototype of an artificial muscle was used to actuate elbow flexo-extension. The authors presented a novel winding method of silicone tubes to perform contraction and relaxation by inflation of pressurized air. The authors that stated the device has a maximum contraction ratio of 35.8% and a maximum output force of 12.24 N with only 5 mm thickness able to lift a forearm up to 90°. Concerning the wrist, few devices actuate only one DoF of its articulation. In [51], authors presented a wearable one DoF device called eWrist. This exoskeleton allows to actuate flexion and extension the in range of 0:20° with a maximum torque of 20 Nm. Authors affirm

that this device can easily be adapted to different users thanks to the integration of two BOA ratchet wheels fixing supports, with a set-up time of 37.3 seconds. A cable driven device for wrist pronation and supination is presented in [52]. The proposed device is a bioinspired mechanism based on the anatomy of forearm pronator teres and pronator quadratus to assist patients with hemiplegia. This skin-brace, weighing 138 grams, enables to complete 150° of rotation with a maximum output torque of 0.879 Nm, without constraining hand and wrist motion up to 100°.

Two Physiological DoF Devices

This section reports devices actuating 2 DoFs of upper limb articulations. In this section, the robots are categorized based on their ability to assist 2 DoFs of the same articulations or 1 DoFs of two different joints. In [53] 2-DoF shoulder exosuit driven by modular, pneumatic, fabric actuators. The exosuit is designed to assist shoulder flexion and abduction motion while reducing muscle activation during arm movements. The exosuit utilizes modular fabric actuators that provide torques to the upper arm, allowing the exosuit to push the arm to any configuration in its RoM. The actuators are composed of a fabric spine and are powered by a pneumatic control system. They are capable of full bending ($>$360°) with low pressures ($\sim$10kPA) and can excert 11.15Nm of torque at the neutral position and 4.44 Nm at 90° shoulder adduction. The exosuit allows for shoulder adduction, rotation along the plane of elevation, and forward flexion or extension. It can perform reaching actions and can support multi-DoF movements. The RoM of the actuators can be adjusted by changing their module configuration. The materials used in the exosuit include fabric and plastic for the actuators. A cable-driven soft robot, proposed in [54], allows the elbow to flex wholly and partially to assist the shoulder flexion up to 100° with a maximum torque of 5Nm. This device is based on a commercial cycling jacket and several textile layers using force-compliant sewing to improve adaption, fixation and force distribution. The total weight of this robot is 1000 grams. For ADL applications, several experiments demonstrated a mean reduction of muscles fatigue of 5.5% and 26.36% for unloaded and loaded case, respectively. Moreover, a delay of muscle fatigue and enhancing gesture repeatability for unloaded case were assessed. Shoulder adduction/abduction and elbow flexo-extension were also actuated by the device proposed in [55]. In this paper authors proposed a pneumatic exosuite, based on two soft wearable components for elbow and shoulder component. These components combine inflatable inextensible textiles with extensible ones. The air pressure is controlled by a controller designed to be self-contained and portable. Using three IMUs for position feedback, this robot is able to perform shoulder adduction/abduction in the

range of 20° to 90° and elbow flexo-extension in the range 0° to 90°. Golgouneh et al [56] presented a hybrid pneumatic and SMA actuated wearable soft exoskeleton for shoulder abduction and horizontal flexion/extension movements both in the range 0° to 90°, ensuring a supplied torque of 2.7 Nm. The authors stated that the main problem of the proposed solution was the thermal insulation of the fabric braids in protecting the skin against the SMA temperature when the robot is fully activated. Additional efforts are required to evaluate the system performance of this robot fully. In [57] the design and performance of an elbow ultralow impedance rigid exoskeleton for upper limb rehabilitation was presented. The exoskeleton allows for independent torque control on elbow flexion/extension and forearm supination/pronation. It is compact and lightweight, weighing 0.9 kg. The exoskeleton delivers a maximum continuous torque of 10 Nm in elbow flexion/extension and 5 Nm in forearm supination/pronation. It has a free mode impedance of 0.02 Nm/° at 1 Hz and a maximum stiffness of 0.5 Nm/°. The exoskeleton utilizes SEAs and a cable-driven differential. The materials used include aluminium alloy for the structure and carbon fiber material for distal components supporting the handle. The overall performance is adequate for robotic therapy applications. A soft exoskeleton for elbow flexo-extension and pronation/supination was presented in [58]. This device is designed to be portable and to actuate elbow articulation by using a fixing plastic ring at the upper arm and a plastic ring with rigid extension beyond the elbow joint at the forearm. These two rings are connected with four nylon cables pulled and released by four servomotors with cable-winders. This device allows to obtain flexo-extension motion in the range 0° to 60° and pronation/supination motion in the range of 0° to 50°. Most of the investigated devices with two DoFs are employed for wrist actuation. A bioinspired model-based soft exoskeleton is designed for wrist mobilization[59]. It is a two DoF exoskeleton, in which the allowed movements are wrist flexion/extension and adduction/abduction. It is capable of covering the RoM of the human wrist in the range of -33° to 33° for flexion/extension and -20° to 33° for adduction/abduction. It is made of commercial materials, such as wrist guards and Bowden cables. The exoskeleton is driven by two Maxon motors and controlled through two drivers and two IMU sensors that measure wrist angles. Choi et al. [60] presented a device named Exo-wrist assisting the wrist of a paretic arm in performing the dart-throwing motion (DTM). To improve efficiency and comfort, this device uses an active forearm 3D printed anchor ensuring a rigid fixing during motion tasks and a relaxation of fixing bracelet when no motion is required. The tightening of the armlet is obtained with a cable and pulleys mechanism driven by an electric actuator. The flexo-extension and abduction/adduction of the wrist are obtained through two cables connected on a fingerless glove in range, respectively, of 0° to 50° and 0° to 20°. A device

with the same mobility as the aforementioned one is presented in [61] where an SMA-based wearable robot is described. The proposed robot, weighing 1000 grams, consists of a glove and a wearable strap, to be fixed on the forearm, connected by 5 muscle-like SMA actuators. SMA actuators are wormed up using current and cooled by an air pump for their contraction and relaxation. This device allows to get 33.8° of flexion, 30.4° for extension, 15.4° for abduction and 21.4° for adduction. The applicable torques for the above motion are 0.61 Nm for flexion, 1.32 Nm for extension, 0.62 Nm for abduction and 0.9 Nm for adduction. A similar approach for wrist mobilization is described in [62] where TCAMs are used instead of SMA. Two rigid belts, connected respectively to the hand and the forearm with eight TCAMs, emulate the working mechanism of forearm muscles in the upper extremities. This robot, weighing 135 grams, can perform wrist flexo-extension and ulnar/radial deviation, respectively, in the range of -65°:65° and -23°:56°. A compact soft robotic wrist brace has been proposed in [63]. It consists of eight modular SOAs connected to a commercial wrist brace with rigid anchors made of fabric for a total weight of 241 grams. This device allows to move the wrist joint in 2-DoF rotation, flexo-extension and radial/ulnar deviations in the range of motion, respectively, -31° to 30° and -22° to 33°. For both motions, the authors stated that this device can supply 0.76 Nm of driving torque. Pneumatic actuators were used also in [64], where a 3D-printed Soft Robotic Wrist Sleeve (SWS) for stroke rehabilitation is described. The SWS enables mobility in two degrees of freedom (flexion-extension and radial-ulnar movements) to rehabilitate the wrist. It is designed to restore at least 70% of a healthy individual's RoM. Pneumatic actuators are employed in the SWS to generate torque, with the applied pressure on the actuators determining the torque output. The safe operating pressure of 200kPa produces 2.5Nm of torque. The SWS actuators, fashioned with a fold-based quadrant, are constructed using flexible 3D-printed materials. The RoM was assessed through various wrist exercises, yielding the following results: flexion 33.9°, extension 34.8°, abduction 17.3°, and adduction 24.6°. To measure torque output, a torque sensor is used, and kinematic data and muscle activity are recorded using sensors such as reflective markers and EMG sensors. A wrist exoskeleton, weighing 960 grams, based on a rigid 3D printed structure actuated by SMA, was developed by Serrano et al [65]. This device guarantees two DoFs allowing flexion-extension and adduction/abduction for rehabilitation purposes through SMA actuation system. The device is fixed to the patient's hand on a glove, with a reduced setup time. Flexo-extension and radial/ulnar deviations vary in the range, respectively, 5° to 40° and -10° to 33° for very slow motions (actuation frequency less than 0.04Hz). A robot for wrist rehabilitation based on a rigid structure actuated by soft actuators was also presented in [66]. This wrist exoskeleton consists of two elastic elements (spring

blades) connected between a rigid ring fixed on the back of the hand and two linear actuators fixed on a forearm anchor through two rotational joints. Controlling the linear actuators for transmitting forces to the spring blades it is possible to obtain wrist flexion/extension, in the range -78° to 55.3°, and adduction/abduction in the range -34.8° to 12.2°. The maximum driving torque for flexo-extension and adduction/abduction are, respectively, 2.49 Nm and 1.77 Nm.

Three Physiological DoF Device

An innovative spherical mechanism for a shoulder joint exoskeleton was described in [67]. The mechanism allows for three DoFs and enables motion as a spherical joint while maintaining the remote center of rotation. The design offers a large RoM free from singularity, high overall stiffness, lightweight design, and compactness. The exoskeleton is designed with brushless DC-motors and harmonic drives, and the driving speed and torques are specified based on musculoskeletal simulations. In [68] authors presented an exoskeleton for elbow, forearm and shoulder mobilization. This exoskeleton has three DoFs and performs different types of shoulder movements, including lateral arm flexion and lifting (abduction and adduction) and elbow flexion. The exoskeleton is made of an elastic fabric (spandex). Brushed motors, which regulate the movement of Bowden cables through a camouflage controller, were used to implement the movements. Flexo-extension of shoulder and elbow was actuated also in [69]. The Stuttgart Exo-Jacket is an exoskeleton designed for the upper body for industrial tasks either stabilizing upper limb in assembly tasks or empowering human joints in logistics applications. Using rigid links between shoulder-elbow and elbow-wrist, the exoskeleton allows flexion and extension movement of the shoulder and elbow joints while the other DoFs are not restricted. The device is designed with two EC motors combined with a Harmonic Drive flat gear allowing a range 0°-50° for shoulder and elbow flexo-extension and 0°-100° for shoulder abduction/adduction. Thanks to the use of rigid links, the maximum available torque for shoulder motions is equal to 40 Nm while for elbow the device can supply a torque of 25 Nm. In [70] the authors describe the design and validation of the RiceWrist-S exoskeleton for robotic rehabilitation after incomplete spinal cord injury. The exoskeleton targets the forearm and wrist for rehabilitation, specifically allowing pronation-supination of the forearm and flexion-extension and radial-ulnar deviation of the wrist. The exoskeleton is designed to have low inertia and friction, isotropic dynamic characteristics, and minimal backlash. The RiceWrist-S utilizes Applimotion 165-A-18 direct-drive actuators for pronation-supination of the forearm and Maxon RE-40 and RE-30 cable drive actuators for flexion-extension and radial-ulnar deviation of the wrist. The ranges of motion of the

exoskeleton joints and the maximum continuous torque output from the joints are: 0°-130° and 3.37 Nm wrist flexion-extension, 0°-75° and 2.11 Nm wrist radial-ulnar deviation, 0-180° and 1.69 Nm elbow pronation-supination. In [71], a 3-DoF robotic exoskeleton was proposed for upper limb assistance using a human-robot interface based on motion intention recognition. The proposed interface uses force-sensing resistors (FSRs) to estimate the user's motion intention in real-time. The exoskeleton is designed for use in rehabilitation or assistive applications. The exoskeleton enables shoulder flexion/extension, abduction/adduction, and elbow flexion/extension movements. It aids the wearer's arm by exerting torques on the joints. The range of motion and applicable torque depend on the specific joint and the movement to be performed. The exoskeleton uses DC motors as actuators to control joint movements. A cable-driven exosuit (LUXBIT) was designed to assists with shoulder and elbow movements [72]. It promotes anatomical adaptation and reduces muscle activity in the upper limbs' flexion. The exosuit allows for natural lifting of the arm and is intended for bimanual assistance in daily living. It provides up to 2.5 kg assistance and has a range of motion for raising the arm in five seconds and flexing the elbow in three seconds. The exosuit is made of soft materials, such as fabrics, and actuators for aiding motion in the ranges 0°-120° for shoulder flexo-extension, 0° to 90° for shoulder adduction/abduction and 0° to 120° for elbow flexo-extension. A portable exosuit, named Auxilio, for upper extremity assistance in rehabilitation was presented in [73]. The exosuit aids with shoulder flexion and abduction, as well as elbow flexion. It enbles dynamic rehabilitation tasks involving trunk motions and over-ground movements. The mechanism is driven by DC motors worn on the wearer's back, and power is transferred to the arm through cable-driven transmission. The exosuit is lightweight and incorporates textile components to increase compliance and decrease weight. The system includes twisted string actuators. A soft wearable upper limb rehabilitation robot using reinforced soft pneumatic actuators (RSPAs) was presented in [74]. Several modules fixed on a wearable carrier, including the RSPA, control system, and air tube modules, compose this device. This device actuates elbow and wrist joints mainly by air inflation and the consequent expansion of the thermoplastic polyurethane (TPU) composite bladders contained in the RSPA. The latter components are arranged around the wrist or elbow joints. The declared RoMs are 0°-26.4° for elbow flexo-extension; -26.4°-26.4° for wrist flexo-extension and $-5°$-5° for wrist radial/ulnar deviation. Pneumatic actuators are also used in [75] in which authors described an exosuit to perform shoulder adduction/abduction in the range 0°-67° , elbow flexo-extension in the range 0°-88°, wrist flexo-extension in the range $-90°$-0°. This soft exosuit weighing 1075 grams in wearable part, excluding the external control box containing the air pump and the control unit, consists of a shoulder

spherical actuator, an elbow actuator and a wrist actuator, which could achieve upper limb joints movement by air inflation and deflation.

Devices for more than three physiological DoF activation

Due to the problems in fixing systems and soft actuation, for the treatment of a high number of DoFs the analyzed devices are based on the use of a rigid structure. Tsai et al[76] developed portable a exoskeleton to help patients in ADLs independently and able to record trajectory and replicate motion. This robot is made with rigid links actuated by pneumatic artificial muscles (PAMs) guaranteeing 4 actuated DoFs and 1 passive DoF. The total weight of the exoskeleton is only 5.6 kg. Active motions are medial/lateral rotation of the shoulder joint in the range $-40°$-40° and flexo-extension of the elbow joint in the range 0°-90°. For these motions, a pair of PAMs are employed to imitate antagonistic muscles. The two PAMs act independently to control shoulder flexion-extension and abduction-adduction in the range 0°-80°. Wearable robots with more than 4 DoFs are usually made with rigid links. A 4 DoFs hybrid (serial-parallel) robot manipulator was proposed in [77]. This robot allows to perform of elbow flexion/extension and pronation/supination as well as wrist flexion/extension and radial/ulnar deviations with limited RoMs, respectively in ranges 0°-98°,$-70°$-80°, $-5°$:17° and $-6°$:8°. For this robot, the 3SPS-type parallel manipulator is suitable for usage in performing rehabilitation therapy in stroke-affected patients. Conversely the authors stated that the 2SPR-type parallel manipulator produced singular configurations while performing the desired rehabilitation. ETS-MARSE [78] is a wearable robotic exoskeleton designed to assist upper limb movements and provide upper limb rehabilitation therapy. The exoskeleton consists of three parts: shoulder motion support, elbow and forearm motion support, and wrist motion support. It is designed to provide naturalistic movements of the shoulder (vertical and horizontal flexion/extension and internal/external rotation), elbow (flexion/extension), forearm (pronation/supination), and wrist joint (radial/ulnar deviation and flexion/extension). The exoskeleton is made of aluminum, which makes it relatively lightweight. The range of motion for each joint is as follows: shoulder $-20°$- 140°, elbow: $-85°$-70°, forearm and wrist not specified. The exoskeleton can generate torques to assist in the movement of the upper limb. The ETS-MARSE utilizes sensors, such as wrist force sensors, to provide input commands for user-guided tasks. A bio-inspired upper limb soft exoskeleton was designed to reduce complications caused by stroke [79]. The exoskeleton is based on the principles of functional anatomy and sports biomechanics. It models skeletal muscles as tension lines and uses a soft bionic robot controlled by a muscle control principle. The exoskeleton allows for

joint motion recovery and has 7 DoFs. It is lightweight and ergonomic, using commercial body protectors and a Bowden cable for the tension lines.

1.3.3 Analysis Results from Systematic Technical Evaluation

The systematic literature review methodology established in Section 1.2 enabled comprehensive analysis of 44 representative upper limb rehabilitation devices. The structured technical tables provide standardized evaluation across multiple criteria, revealing clear patterns in technological approaches and persistent limitations constraining clinical effectiveness.

Table 1.5 presents selected results from the comprehensive analysis, illustrating the diversity of approaches while highlighting trade-offs between functionality, portability, and clinical viability that characterize the current state of the field.

Analysis of these devices reveals four critical patterns:

- Functionality-portability trade-off: Clear inverse relationships exist between functionality and deployment constraints. Devices with limited DoF coverage demonstrate superior portability (masses below 2.5 kg), while systems with extensive joint coverage face weight penalties exceeding 7 kg, directly impacting deployment feasibility for home-based rehabilitation.

- Clinical readiness gap: TRL distribution concentrates at levels 3-5, with limited clinical validation. Only 6 of 24 devices achieve TRL 5 or higher with clinical assessments, while the majority remain at proof-of-concept (TRL 3) or prototype validation (TRL 4) stages, highlighting challenges in translating technological capabilities into clinically validated applications.

- Actuation strategy patterns: Cable-driven DC motor systems dominate (17 of 24 devices), reflecting maturity and reliability for force transmission. Alternative strategies including pneumatic (4 devices), SMA-based (3 devices), and hybrid combinations remain exploratory, facing performance challenges while offering potential advantages in compliance or safety.

- Portability constraints: Only 9 of 24 devices achieve full portability, with 6 having limited portability due to external power or control dependencies. This constrains deployment contexts, restricting advanced systems to supervised clinical environments and preventing integration into daily living activities.

Table 1.5 Analysis results from systematic technical evaluation of representative devices.

Name	TRL	DoFs	Target element	Motion	Motion range [deg]	Max Torque [Nm]	Clinic. assess.	Portable	AF	Actuation schema	Mass [grams]
Elbow Flexion Platform[42]	3	1R	Elbow	Flex/Ext	0:90	12	No	Yes	IAER	Cables, DC motors	NA
Wearable soft exoskeleton[36]	4	1R	Shoulder	Adb/Add	32.5:45.5	6	No	No	ADL	McKibben muscle	NA
Myoshirt[37]	5	1R	Shoudler	Flex/Ext	0:110	34	Yes	Yes	GA, HRA, ADL	Springs, Cables, DC motors	520
Bi-articular exosuit [40]	4	1R	Elbow	Flex/Ext	0:90	24	No	Yes	IAER	EC motors, Cables	7500
Upper limb soft exosuit [41]	3	1R	Elbow	Flex/Ext	0:90	3.89	No	Yes	IAER	SMA, Springs	4000
Swee[43]	3	1R	Elbow	Flex/Ext	0:150	3.5	No	Yes	HRA	SMA	600
Carry [44]	4	1R	Elbow	Flex/Ext	0:90	7.2	No	Yes	IAER	Pneumatic	1850
Soft exosuit on arm[7]	5	1R	Elbow	Flex/Ext	0:90	8.5	No	Yes	HRA, IAER	EC motors, Cables	1700
One-to-many actuator [46]	5	1R	Elbow	Flex/Ext	0:90	3.4	No	Yes	IAER, ADL	Cables, DC motors	2200
Cale [49]	4	1R	Elbow	Flex/Ext	0:60	10	No	Yes	HRA, IAER	Spring, Cables, DC motors	5000
Ewrist [51]	5	1R	Wrist	Flex/Ext	-20:20	2.1	No	Yes	HRA	DC motors	130
Exo-Wrist[60]	4	2R	Wrist	Flex/Ext	-50:50	0.5	No	Yes	HRA, CRA	Cables, DC motors	1003
				Abd/Add	-20:20	0.5					
Shoulder exosuit [53]	2	2R	Shoulder	Flex/Ext	0:90	4.44	No	Yes	HRA	Pneumatic	NA
				Abd/Add	0:45	4.44					
Cable-driven exosuit [54]	4	2R	Shoulder	Flex/Ext	0:100	5	No	Yes	HRA	Cables, DC motors	1000
			Elbow	Flex/Ext	0:90	5					
Hybrid exoskeleton [56]	3	2R	Shoulder	Flex/Ext	0:90	2.7	No	Yes	HRA	SMA, Pneumatic	NA
				Abd/Add	0:90	2.7					
Ulix [57]	4	2R	Elbow	Flex/Ext	0:135	8.6	No	No	CRA	SEA, Cables	900
				Pro/Sup	-90:90	2.7					
Cadel [58]	4	2R	Elbow	Flex/Ext	0:60	5	No	Yes	HRA	Cables, DC motors	NA
				Pro/Sup	-50:50	5					
Bioinspired wrist exoskeleton[59]	5/6	2R	Wrist	Flex/Ext	-35:35	6.75	Yes	Yes	HRA	Cables, DC motors	NA
				Abd/Add	-20:33	6.75					
Soft wrist assist (SWA)[61]	5	2R	Wrist	Flex/Ext	-33:30.4	1.32	Yes	Yes	HRA	Cables, DC motors	NA
				Abd/Add	-15.4:21	0.9					
Crux[68]	5	3R	Shoulder	Flex/Ext	0:60	88.3	No	Yes	HRA	Cables, DC motors	1300
				Abd/Add	0:90	88.3					
			Elbow	Flex/Ext	0:90	88.3					
Stuttgart exo-jacket [69]	6	3R	Shoulder	Flex/Ext	0:50	40	No	Yes	IAER	Rigid Links, EC motors	NA
				Abd/Add	0:10	40					
			Elbow	Flex/Ext	0:50	40					
Ricewrist-s [70]	5	3R	Elbow	Pro/Sup	-90:90	1.69	No	No	HRA, IAER	Rigid Links, DC motors	NA
			Wrist	Flex/Ext	-65:65	3.37					
				Abd/Add	-30:35	2.11					
Auxilio[73]	4	3R	Shoulder	Flex/Ext	0:80	21.6	No	Yes	HRA, IAER	Twisted String, DC motors	3200
				Abd/Add	0:80	21.6					
			Elbow	Flex/Ext	0:120	21.6					
Ets-marse[78]	4	6R	Shoulder	Flex/Ext	0:140	24	No	No	CRA	Rigid links, DC motors	7720
				MR/LR	-20:90	24					
			Elbow	Flex/Ext	0:120	7.8					
				Pro/Sup	-85:85	5					
			Wrist	Flex/Ext	-25:20	5					
				Abd/Add	-50:60	5					

1.4 Problem Definition and Research Gap Identification

1.4.1 Critical Limitations Identified Through Systematic Analysis

The comprehensive systematic analysis reveals persistent limitations that constrain clinical effectiveness and widespread adoption of upper limb rehabilitation technologies [80; 81]. Table 1.6 provides a comparative overview of representative devices, illustrating how existing systems address different aspects of rehabilitation requirements while exposing persistent challenges in achieving comprehensive solutions.

Table 1.6 Comparative analysis of limitations in existing upper limb rehabilitation systems.

System	Weight [kg]	DoF	ROM [deg]	Portable	Multi-Joint	Sensing Method
Ets-marse [78]	7.72	6	140	No	Yes	Encoder-based
Auxilio [73]	3.2	3	120	Limited	Yes	Force sensors
Bi-articular exosuit [40]	7.5	1	90	No	Limited	Load cells
Myoshirt [37]	0.52	1	110	Yes	No	Textile sensors
Cable-driven exosuit [54]	1.0	2	100	Limited	Yes	Load cells
Elbow Platform [42]	N/A	1	90	No	No	Load cells
Target Requirements	**< 3.5**	**$\geq$3**	**$\geq$120**	**Yes**	**Yes**	**Advanced**

Coordination and Functional Scope Limitations

The systematic analysis reveals that current rehabilitation technologies demonstrate a predominant focus on isolated joint assistance, with limited capability to reproduce the coordinated movement patterns essential for functional activities of daily living. This limitation highlights a critical research gap in developing solutions that effectively support functional motor recovery. Natural upper limb movements during reaching, grasping, and manipulation tasks require precise coordination between shoulder, elbow, and wrist joints, involving complex muscle activation patterns and kinematic synergies that single-joint devices cannot adequately support [10].

Analysis of the technical characteristics summarized in Table 1.6 reveals that while devices providing multi-joint capabilities demonstrate potential for comprehensive assistance, they simultaneously face increased complexity in mechanical implementation, control architecture design, and weight penalties that compromise practical deployment. This fundamental tension between comprehensive assistance and practical usability represents a critical barrier to clinical adoption and widespread deployment in home-based rehabilitation contexts.

Sensing architecture and control precision constraints

Sensing architecture selection directly impacts achievable control quality in rehabilitation devices. Cable-driven systems predominantly employ load cells for force measurement, enabling force-based control strategies with high sensitivity for implementing admittance and impedance control [23]. Force measurement enables detection of user movement intentions, allowing assistance adaptation during functional movements [40; 54].

However, common load cell placement at cable anchor points introduces fundamental limitations. As joint configurations change during movement, cable routing geometry varies significantly, creating posture-dependent measurement errors that restrict operational range [82]. This constraint intensifies in multi-joint coordination scenarios where simultaneous force control across multiple degrees of freedom faces variable cable geometries and distributed anchor points.

Advancing cable-driven multi-joint technologies requires sensing architectures that preserve force-based measurement advantages (control precision, sensitivity, and intention detection) while extending operational ranges to encompass functional movement requirements without sacrificing workspace coverage necessary for effective rehabilitation.

Design methodology and optimization gaps

The field lacks validated systematic approaches for rehabilitation device development that effectively integrate user requirements, technical constraints, and performance optimization [83]. Current development practices rely predominantly on iterative prototyping and ad-hoc design decisions, limiting reproducibility of successful solutions and preventing systematic knowledge transfer between research groups. The absence of established design methodologies contributes to prolonged development cycles and difficulties in translating research prototypes into clinically viable products suitable for widespread deployment.

This methodological gap results in devices that may address specific technical challenges while failing to achieve optimal balance across multiple competing requirements including functionality, usability, safety, and clinical effectiveness. The absence of structured design frameworks prevents systematic exploration of the design space and identification of solutions that optimally satisfy the multidimensional requirements characteristic of rehabilitation applications. Addressing this gap requires validated frameworks that guide design decisions through explicit consideration of trade-offs, enabling reproducible development of optimized solutions.

1.4.2 Research Gap Synthesis and Innovation Requirements

The systematic analysis identifies three interconnected research gaps that collectively constrain advancement toward clinically effective, widely deployable rehabilitation technologies:

Table 1.7 Research gap synthesis with explicit mapping to thesis contributions.

Research Gap	Current Limitation	Innovation Direction	Addressed in
Coordination Architecture	Isolated joint assistance fails to support functional movement patterns (67% single-joint only, Table 1.5)	Integrated multi-joint coordination preserving natural synergies	Chapter 3, Contribution 2
Sensing and Control	Configuration-dependent measurement accuracy constrains operational envelope in cable-driven systems	Sensing architectures maintaining precision across extended ranges	Chapter 3, Contribution 3
Design Methodology	Ad-hoc development prevents systematic optimization and reproducibility	Validated frameworks integrating requirements and constraints	Chapter 2, Contribution 1

Research Gap 1 - Coordination Arhictecture: Effective rehabilitation requires assistance strategies that maintain natural coordination patterns between shoulder and elbow joints during functional movements. Current approaches struggle to provide meaningful multi-joint assistance while preserving the kinematic and dynamic coupling inherent in coordinated upper limb tasks. This gap extends beyond mechanical design to encompass control architectures capable of distributing assistance forces appropriately across multiple degrees of freedom while adapting to individual user capabilities and movement intentions.

Research Gap 2 - Sensing and Control Precision: Achieving natural, responsive assistance across extended operational ranges requires sensing architectures that maintain measurement accuracy independent of joint configuration throughout coordinated movements. Existing force-based sensing approaches, while offering excellent sensitivity and intention detection capabilities in cable-driven systems, face fundamental trade-offs between operational range and measurement accuracy that constrain practical implementation of multi-joint coordination strategies. Addressing this gap requires sensing configurations that enable reliable force feedback across the complex kinematic configurations characteristic of functional upper limb movements without compromising workspace coverage.

Research Gap 3 - Systematic Design Framework: Current development practices rely heavily on iterative refinement without validated methodologies guiding systematic exploration of design alternatives. The field requires frameworks that explicitly address trade-offs between competing requirements, integrating biomechanical constraints, user needs, and

technical possibilities to enable reproducible development of optimized solutions balancing functionality, usability, safety, and clinical effectiveness.

Addressing these identified research gaps requires integrated development of systematic methodologies and innovative technical solutions. The following chapters present this integrated approach: Chapter 2 develops the systematic design framework, Chapters 3-4 demonstrate its application through a coordinated multi-joint exoskeleton incorporating novel sensing architectures, and Chapter 5 validates complementary assessment methods. Detailed contributions are presented in the Introduction.

Chapter 2

Systematic Design and Operation Methodology

This chapter presents the systematic design and operation methodology developed for upper limb rehabilitation exoskeletons, addressing the research gaps identified in Chapter 1. The methodology provides a structured framework that integrates requirements definition, multi-criteria decision making, concept generation, mathematical modeling, and validation strategies to ensure the development of effective, usable, and clinically relevant rehabilitation technologies.

The comprehensive analysis in Chapter 1 revealed three critical limitations constraining current rehabilitation technologies: limited multi-joint coordination capabilities (Section 1.4), configuration-dependent measurement accuracy restricting functional ranges of motion, and the persistent challenge of achieving comprehensive functionality within practical portability constraints (Table 1.6). These limitations stem not only from technical challenges but also from the absence of systematic design approaches that effectively integrate user requirements, biomechanical constraints, and technical possibilities [83].

Current development practices rely predominantly on iterative prototyping and ad-hoc design decisions, limiting reproducibility and preventing systematic knowledge transfer between research groups [6]. The design of an upgrade or a new solution must start from the analysis of current technologies, as demonstrated through the systematic literature review in Chapter 1. During the conceptual design phase, multiple design alternatives are generated based on defined functional and performance requirements. Although this stage has a major influence on cost, robustness, reliability, and development time, a systematic and well-structured design process tends to reduce, rather than increase, overall costs by limiting

unnecessary iterations, enabling early evaluation of alternatives, and guiding the selection of the most effective design solution [84].

This methodology builds upon established systematic design principles [84; 85] while incorporating domain-specific considerations essential for rehabilitation device development. The framework directly addresses the identified research gaps through: (1) structured requirements capturing multi-joint coordination needs and functional range requirements, (2) quantitative evaluation criteria enabling systematic exploration of alternative design concepts including novel sensing architectures, and (3) explicit optimization of portability-functionality trade-offs through weighted multi-criteria decision making.

Chapter 3 demonstrates the methodology's practical application through the development of a coordinated shoulder-elbow exoskeleton, validating its effectiveness in translating systematic analysis into functional implementations that address the identified limitations.

2.1 Proposed Methodological Framework Architecture

The proposed systematic methodology represents a comprehensive approach that integrates technical, biomechanical, ergonomic, and clinical constraints through sequential phases. The methodology evolved from the systematic literature review framework presented in Section 1.2, extending beyond analysis of existing technologies to encompass the complete design cycle from concept to validated implementation.

Figure 2.1 illustrates the overall architecture of the systematic design methodology, showing the sequential phases and decision points that guide the development process from initial specifications to final design and testing.

The methodology is structured around six systematic phases with explicit decision points enabling iterative refinement:

Phase 1 - Define Design Specifications: The process begins by defining the project's initial specifications through a Product Design Specification (PDS) framework. Requirements are derived from the comprehensive analysis in Chapter 1, including anatomical constraints (Section 1.1), functional requirements for activities of daily living (Table 1.1), and identified limitations of existing technologies (Table 1.6).

Phase 2 - Consult Summary Table: The summary table containing analyzed devices from the systematic review (Section 1.3) is consulted to identify existing solutions. Devices not meeting the initial specifications are excluded, establishing whether compatible solutions exist within the current state of the art.

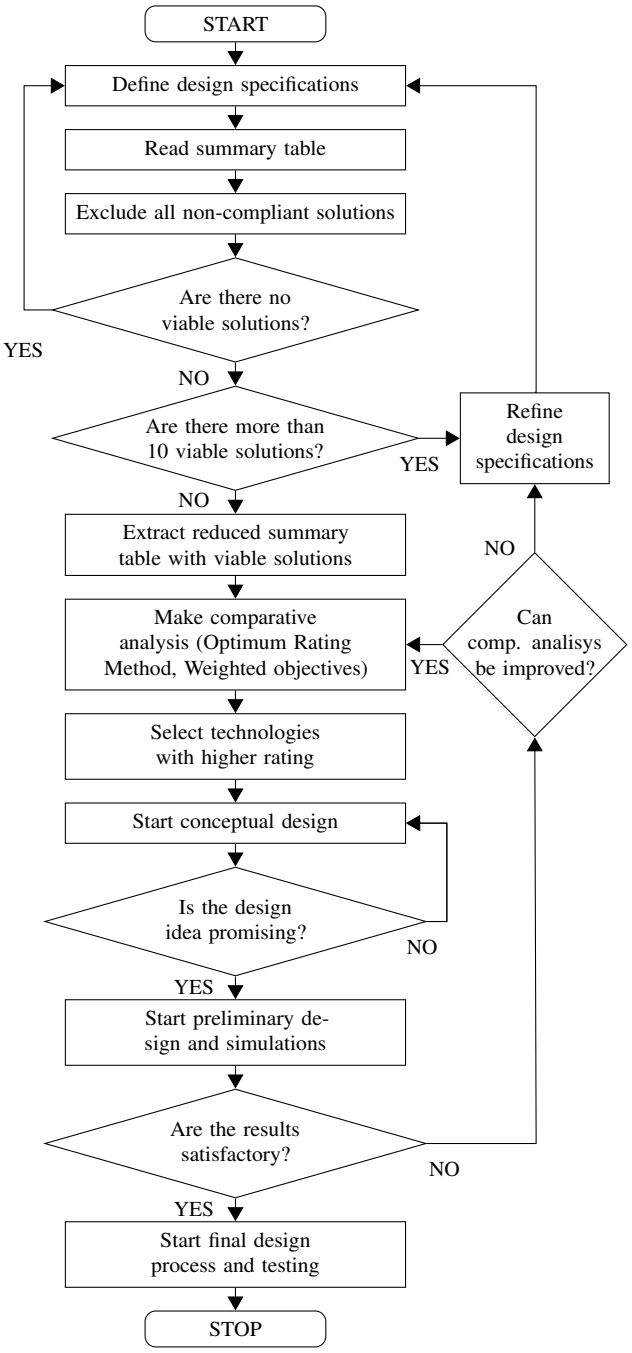

Figure 2.1 Systematic design methodology flowchart showing the sequential phases from requirements definition through validated implementation. Decision points (diamond shapes) ensure iterative refinement when specifications are not met or when the solution space requires narrowing.

Phase 3 - Feasibility Check and Solution Space Refinement: A critical decision point evaluates the number of viable alternatives. If no compatible solutions exist, specifications are revised to ensure feasibility. If too many solutions exist (exceeding a threshold of

approximately 20 alternatives [86]), specifications are refined to narrow the design space to a manageable set for detailed evaluation.

Phase 4 - Extract Reduced Summary Table: Once an appropriate number of alternatives is identified, a reduced summary table is created containing only viable options that satisfy fundamental requirements. This filtered set forms the basis for comparative analysis.

Phase 5 - Comparative Analysis via MCDM: Multi-Criteria Decision Making methods (weighted rating and weighted objectives) provide quantitative evaluation of alternatives against established criteria. The analysis identifies the top 3-4 solutions demonstrating highest compliance with project specifications for detailed concept development.

Phase 6 - Concept Design and Verification: A personalized concept design is developed based on selected technologies. If specifications are not completely satisfied, the process evaluates whether improving the comparative analysis (returning to Phase 5) or redefining specifications (returning to Phase 1) is more appropriate.

Phase 7 - Preliminary Design and Mathematical Modeling: Detailed design proceeds with mathematical modeling and simulation to verify technical feasibility and predict performance across the operational envelope. Models incorporate kinematic analysis, dynamic simulation, and workspace evaluation.

Phase 8 - Design Evaluation and Iterative Refinement: Simulation results are assessed against specifications. Unsatisfactory performance triggers iterative design refinement within Phase 7 until predicted performance meets requirements.

Phase 9 - Final Design and Experimental Validation: Once preliminary design is validated through modeling, final design proceeds with prototype development and comprehensive experimental testing following the validation framework (Section 2.3.5).

This structured sequence ensures methodical progression from requirements to validated implementation while maintaining flexibility through decision points that prevent arbitrary design modifications. The explicit criteria at each decision point enable objective evaluation of when to iterate versus when to proceed, reducing development time while ensuring systematic exploration of the design space [84].

The methodology distinguishes between *refinement iterations* (within-phase improvements based on analysis results) and *redefinition iterations* (returning to earlier phases when fundamental assumptions prove invalid). This distinction prevents excessive local optimization when global reconsideration is required, a common pitfall in ad-hoc development approaches [85].

2.2 Systematic Design Approach

The systematic design approach provides structured processes for each phase of the design cycle, with particular emphasis on the requirements definition and multi-criteria decision making phases that form the foundation for subsequent design activities.

2.2.1 Requirements Definition and Design Specifications

The methodology begins with critical analysis of the state of the art through the systematic review approach presented in Section 1.2. This analysis identifies current solutions, unsolved problems, and recurring kinematic and dynamic models, providing the basis for subsequent design decisions. In parallel, competitive benchmarking is conducted through analytical and comparative evaluation of competing solutions using the technical analysis framework from Section 1.2.2.

The Product Design Specifications (PDS) outline the project's methodological approach, identifying functional, performance, regulatory, and environmental requirements based on preliminary analyses, compliance requirements, end-user needs, and expected operating conditions. The PDS framework provides structured documentation organizing requirements into categories enabling systematic evaluation [87].

Table 2.1 presents the comprehensive PDS template developed for upper limb rehabilitation devices, providing a framework for capturing and organizing design requirements across all relevant categories.

The PDS construction follows a systematic process: (1) requirement gathering from literature, biomechanical analysis (Chapter 1), and regulatory standards, (2) requirement classification into PDS categories, (3) specification definition with target, minimum acceptable, and maximum permissible values distinguishing between mandatory and desirable features, (4) priority assignment (critical/high/medium/low) guiding trade-off decisions, and (5) iteration and refinement based on feasibility analysis [88].

The PDS provides structured documentation gathering key parameters related to kinematics (degrees of freedom and working area), dynamics (maximum velocities and accelerations, required forces and torques), dimensional constraints (geometry, mass, weight distribution), and considerations regarding energy efficiency, sustainability, and infrastructure compatibility. This tool guides design decisions, allowing early identification of potential problems and ensuring the project meets established objectives. Requirements traceability is maintained throughout development, with each PDS specification explicitly mapped to design decisions and validation criteria [89].

Table 2.1 Product Design Specification (PDS) template for upper limb rehabilitation exoskeletons with categories, parameters, and specification criteria.

Category	Parameter	Specification Criteria
Functional	Main Function	Primary rehabilitation assistance mode (active, passive, adaptive)
	Target Joints	Specific anatomical joints to be assisted with physiological DoF classification (Section 1.2.2)
	Assistance Type	Power assistance, gravity compensation, or resistive training
	Movement Patterns	Supported movement types and sequences for ADL tasks
Performance	Range of Motion	Target ROM relative to FRoM requirements (Table 1.1)
	Maximum Torque	Required assistance levels based on biomechanical analysis
	Response Time	Dynamic performance requirements (typically < 50ms)
	Workspace Coverage	Percentage of functional workspace to be covered ($\geq 95\%$)
Dimensional	Total Mass	Target < 5 kg for portability (from state-of-art analysis)
	Dimensions	Maximum dimensional constraints for wearability
	Anthropometric Range	Accommodation range (typically 5th-95th percentile)
	Mass Distribution	Weight distribution for comfort and balance
Usability	Donning/Doffing	Self-application capability and time requirements
	Adjustability	Anthropometric adaptation mechanisms (tool-free preferred)
	User Interface	Interaction complexity matching target population capabilities
Safety	Force Limits	Maximum forces preventing tissue damage per ISO 13482 [28]
	Emergency Stop	Response time requirements (< 100ms)
	Fail-safe Modes	Behavior upon power loss or system failure
Environmental	Operating Conditions	Temperature range, humidity tolerance (indoor: 15-30°C, 20-80% RH)
	Durability	Minimum operational cycles (e.g., 10,000 for daily use over 1 year)
	Maintenance	Cleaning compatibility, service intervals, consumable replacement
Manufacturing	Materials	Biocompatible materials (ISO 10993), structural material selection
	Production Method	Manufacturing approach (custom vs. scalable production)
	Cost Constraints	Target price point for intended market segment

2.2.2 Integration of Multi-Criteria Decision Making

The Multi-Criteria Decision Making (MCDM) framework provides quantitative approaches for evaluating and selecting optimal design concepts from multiple alternatives. After defining the PDS, the methodology employs rating and weighting methods to systematically evaluate design alternatives against established criteria [90].

The MCDM process implemented in this methodology follows a structured approach: (1) criteria identification and weighting based on PDS priorities, (2) alternative selection from the reduced summary table (Phase 4), (3) performance evaluation for each alternative-criterion pair, and (4) scoring and ranking enabling objective selection [91]. The determination of weights depends critically on the priorities established in the PDS, with mandatory requirements receiving maximum weights to ensure non-negotiable specifications are satisfied.

Table 2.2 presents the evaluation criteria specifically developed for upper limb rehabilitation devices based on the comprehensive literature review and requirements analysis. Each criterion includes a weight W_{C_i} ranging from 1 (negligible importance) to 10 (mandatory requirement). The criteria encompass physical constraints (C1-C2), usability factors (C3, C12), performance capabilities (C4-C5), safety considerations (C6), and functional coverage (C7-C11).

Criterion weights are not arbitrary but derive systematically from the PDS through a structured process. Mandatory requirements identified in the PDS (e.g., safety, portability for home rehabilitation) receive maximum weights ($W_{C_i} = 10$) to act as threshold filters—alternatives failing these criteria receive zero overall scores regardless of other merits. High-priority requirements receive weights of 6-8, while desirable features receive weights of 3-5. This weighting scheme ensures design decisions align with established project priorities while enabling quantitative trade-off analysis [92].

The ROM vs FRoM compliance criterion (C11) evaluates how well the device's achievable range of motion matches the functional range required for ADL tasks. This rating is calculated as:

$$R_{11y} = \frac{1}{n} \sum_{l=1}^{n} x_{ly} \tag{2.1}$$

where n is the number of joint motions being evaluated and x_{ly} represents the compliance ratio for each specific motion l of device y. For example, for elbow flexion: $x_{ly} = R_{7y} \times (E_{fy}/E_{ff})$ where E_{ff} is the maximum required functional elbow flexion for ADLs, E_{fy} is the elbow flexion guaranteed by the device, and R_{7y} is the boolean indicating whether the device actuates elbow flexion/extension.

Table 2.2 MCDM criteria for upper limb rehabilitation device evaluation with weighting factors and evaluation approaches.

ID	Criterion	Weight	Description and Evaluation Method
C1	Mass	6	Total system weight affecting portability. Rating: $R_{1y} = M_{max}/M_{dy}$ where M_{max} = 3 kg (maximum desired weight) and M_{dy} is device weight
C2	Portability	10	Capability for mobile use and home rehabilitation. Boolean: 1 if portable, 0 otherwise. Maximum weight as mandatory specification
C3	Self-wearability	5	Independent donning/doffing capability. Scale: 0 = requires assistance, 1 = difficult alone, 2 = achievable alone
C4	Available Torque	4	Assistance capability for functional movements. Rating: ratio of available torque to required torque for ADL tasks
C5	Stability of Fixing	8	Secure attachment during dynamic movements. Scale: 3 = completely stable, 2 = stable for low loads, 1 = reported instability
C6	Safety	10	User protection and risk mitigation per ISO 13482. Scale: 3 = no issues, 2 = few issues, 1 = serious issues. Maximum weight as mandatory
C7	Shoulder Flex/Ext	6	Range of motion for shoulder flexion/extension. Boolean: 1 if capability present, 0 otherwise
C8	Shoulder Elevation	4	Capability for shoulder abduction/adduction. Boolean: 1 if capability present, 0 otherwise
C9	Elbow Flex/Ext	6	Range of motion for elbow flexion/extension. Boolean: 1 if capability present, 0 otherwise
C10	Wrist Mobility	3	Wrist articulation capabilities. Boolean: 1 if capability present, 0 otherwise
C11	ROM vs FRoM	10	Functional range compliance. Rating: $R_{11y} = (1/n)\sum_{l=1}^{n} x_{ly}$ where x_{ly} evaluates ROM compliance with FRoM for each joint motion. Maximum weight for primary rehabilitation objective
C12	Control Complexity	6	System complexity and ease of operation. Scale: 3 = simple control, 2 = moderate complexity, 1 = high complexity

For each design alternative y from the reduced summary table, performance is evaluated against each criterion. The evaluation considers both quantitative measures (calculated using formulas in Table 2.2) and qualitative assessments based on design characteristics and literature data.

The overall score for each alternative y is calculated using the weighted sum approach with portability constraint:

$$Score_y = B_y \times \sum_{i=1}^{12} P_{iy} \tag{2.2}$$

where:

$$P_{iy} = W_{C_i} \times R_{iy} \tag{2.3}$$

and $B_y = R_{2y}$ (portability boolean), which ensures non-portable devices receive zero score regardless of other merits, directly enforcing the mandatory portability requirement established in the PDS. In these equations, W_{C_i} is the weight of criterion i and R_{iy} is the rating of alternative y for criterion i.

Table 2.3 demonstrates the MCDM evaluation applied to representative exoskeleton concepts from the systematic review, showing how the scoring methodology identifies the most promising design approaches.

Table 2.3 MCDM evaluation example comparing exoskeleton design alternatives from state-of-art analysis (Section 1.3).

Alternative	**C1** (6)	**C2** (10)	**C3** (5)	**C4** (4)	**C5** (8)	**C6** (10)	**C7** (6)	**C8** (4)	**C9** (6)	**C10** (3)	**C11** (10)	**C12** (6)	**Score**
Elbow Platform [42]	3.0	1	2	0.5	3	3	1	0	1	0	0.7	3	**102.7**
Exo-Wrist [60]	3.0	1	2	0.5	3	3	0	0	0	1	4.3	2	**121.2**
Cable-Driven [54]	3.0	1	1	0.2	2	3	1	0	1	0	0.7	2	**98.8**
Bioinsp. Wrist [59]	3.0	1	2	0.3	2	3	0	0	0	1	4.6	1	**90.4**

This quantitative evaluation enables objective comparison of design alternatives while explicitly accounting for the relative importance of different performance aspects. The scoring reveals which devices best satisfy the established requirements, with higher scores indicating better overall compliance with specifications. In this example, the Exo-Wrist concept achieves the highest score (121.2) due to superior wrist mobility coverage (C10, C11) despite modest performance in shoulder and elbow capabilities.

Based on MCDM results, the top 3-4 scoring alternatives are selected for detailed consideration. These selected technologies may be combined to create hybrid solutions leveraging the strengths of multiple approaches, as demonstrated in the application example (Chapter 3). The selection process explicitly documents trade-offs, enabling transparent justification of design decisions [93].

To graphically highlight strengths and weaknesses of compared devices, radar charts displaying the parameter values P_{iy} for each alternative provide intuitive visualization of performance trade-offs across criteria. Figure 2.2 presents an example radar chart comparing

the four alternatives from Table 2.3, clearly illustrating that while Exo-Wrist excels in wrist-related criteria, Elbow Platform provides superior elbow support, informing potential hybrid design strategies.

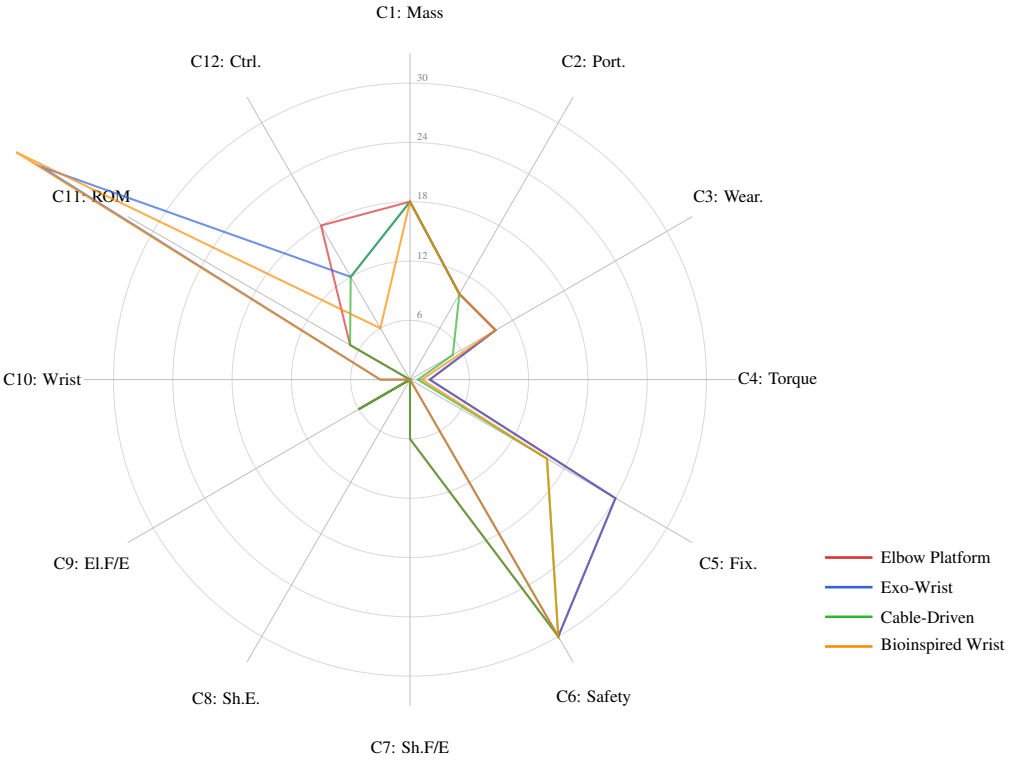

Figure 2.2 Radar chart visualization of MCDM evaluation for four representative alternatives, showing weighted criterion scores P_{iy}. Each axis represents a different criterion (C1-C12), with distance from center indicating performance. The visualization reveals complementary strengths: Exo-Wrist (blue) excels in wrist mobility (C10, C11), while Elbow Platform (red) provides superior elbow assistance (C9), suggesting potential for hybrid designs combining multiple technologies.

This visualization aids in understanding which specific aspects drive the overall scores and facilitates informed decision-making when selecting technologies for concept development. The radar chart representation also enables rapid identification of performance gaps, criteria where all alternatives perform poorly, highlighting opportunities for innovation and areas requiring novel technical solutions.

2.3 Modeling and Simulation Framework

Following concept selection through MCDM, mathematical modeling provides theoretical foundation for performance prediction and design verification before physical prototyping.

This phase employs kinematic and dynamic models to assess feasibility, optimize design parameters, and predict system behavior across the operational envelope [27].

Mathematical modeling serves multiple critical functions in the systematic design process: (1) validation of workspace coverage relative to functional requirements (MCDM criterion C11), (2) prediction of required actuator forces and torques informing component selection, (3) optimization of geometric parameters such as cable anchor point positioning, and (4) establishment of quantitative baselines for experimental validation. The modeling fidelity must balance computational efficiency against prediction accuracy, with model complexity adapted to the specific design questions being addressed [94].

2.3.1 Kinematic and Dynamic Models

Mathematical modeling of upper limb rehabilitation devices requires integration of human limb kinematics with device-specific characteristics. The modeling approach builds upon the anatomical foundation established in Section 1.1, incorporating anthropometric variability to ensure designs accommodate target user populations [95].

Kinematic Modeling

The kinematic analysis employs generalized coordinates $\mathbf{q} = [q_1, q_2, \ldots, q_n]^T$ to describe the configuration of the multi-body system. For upper limb devices, the kinematic chain includes shoulder, elbow, and wrist joints with varying degrees of freedom as classified in Section 1.2.2. Figure 2.3 illustrates a representative kinematic model for a multi-joint upper limb exoskeleton showing coordinate frame assignments.

The position vector of any point P on body i is expressed in the global reference frame as [94]:

$$\mathbf{r}^P = \mathbf{r}^i + \mathbf{A}^i \bar{\mathbf{u}}^P \tag{2.4}$$

where $\mathbf{r}^i$ is the position vector of the origin of the body reference frame, $\mathbf{A}^i$ is the transformation matrix from body frame to global frame, and $\bar{\mathbf{u}}^P$ is the local position vector of point P in the body frame.

For a system with kinematic constraints, the constraint equations are expressed as [94]:

$$\Phi(\mathbf{q}, t) = \mathbf{0} \tag{2.5}$$

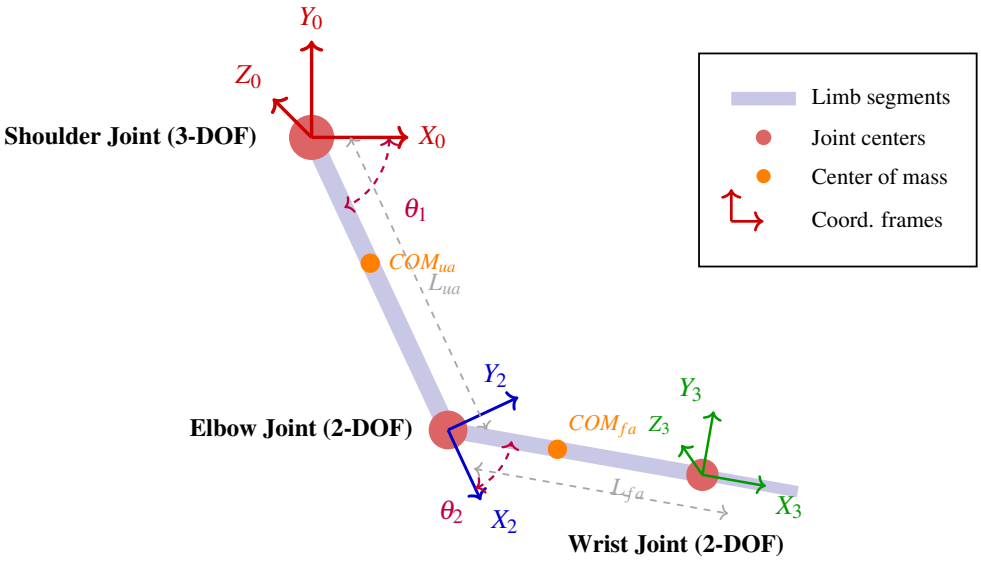

Figure 2.3 Kinematic chain for upper limb exoskeleton with coordinate frame assignments. Shoulder: 3-DoF spherical joint; elbow: 2-DoF joint (flexion/extension and pronation/supination); wrist: 2-DoF joint. Anthropometric parameters (L_{ua}, L_{fa}) are adapted to user characteristics.

where Φ is the vector of constraint equations. The velocity and acceleration constraint equations are obtained by successive differentiation:

$$\Phi_{\mathbf{q}}\dot{\mathbf{q}} = -\Phi_t \tag{2.6}$$

$$\Phi_{\mathbf{q}}\ddot{\mathbf{q}} = -(\Phi_{\mathbf{q}}\dot{\mathbf{q}})_{\mathbf{q}}\dot{\mathbf{q}} - 2\Phi_{\mathbf{q}t}\dot{\mathbf{q}} - \Phi_{tt} \tag{2.7}$$

where $\Phi_{\mathbf{q}}$ is the Jacobian matrix of the constraint equations with respect to generalized coordinates. Forward kinematics relates joint angles to end-effector position through the mapping function [27]:

$$\mathbf{p} = \mathbf{f}_{FK}(\mathbf{q}) \tag{2.8}$$

where $\mathbf{f}_{FK}$ represents the forward kinematics transformation. Workspace analysis determines reachable positions enabling verification of functional range coverage (MCDM criterion C11). The reachable workspace $\mathscr{W}_R$ is evaluated across permissible joint angle combinations [27]:

$$\mathscr{W}_R = \{\mathbf{p} \in \mathbb{R}^3 \mid \exists \mathbf{q} \in \Theta_{permissible} : \mathbf{p} = \mathbf{f}_{FK}(\mathbf{q})\} \tag{2.9}$$

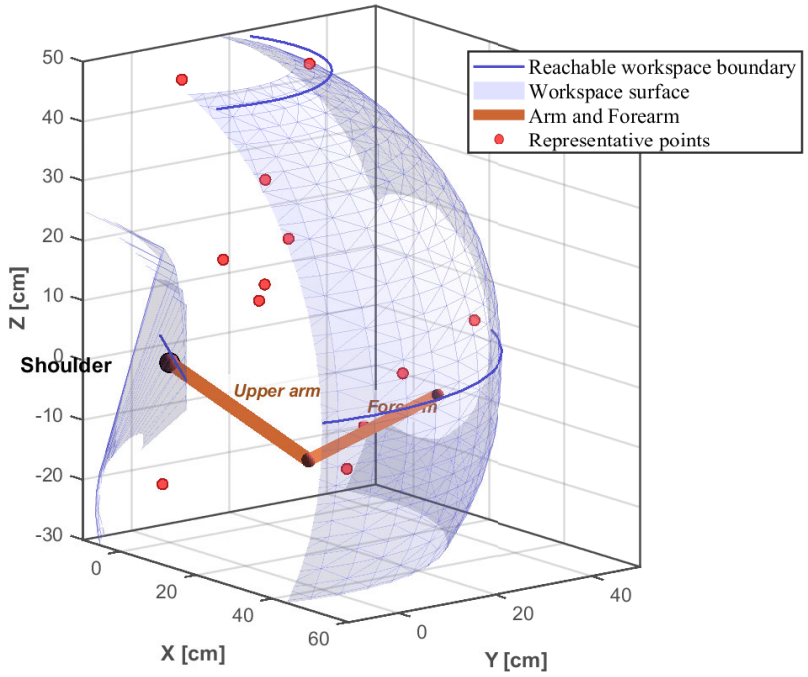

Figure 2.4 Workspace analysis for generic shoulder-elbow system showing reachable positions. The arm configuration (orange segments) represents a typical posture within the operational range. Representative points (red markers) illustrate discrete reachable positions. Workspace boundaries are computed from forward kinematics across physiological ROM constraints.

where $\Theta_{permissible}$ represents joint angle ranges constrained by anatomical limits and device limitations. Figure 2.4 presents a representative workspace analysis comparing device operational range with functional requirements for ADL tasks.

Workspace coverage is quantified by computing the percentage of ADL task positions contained within the reachable workspace:

$$\text{Coverage} = \frac{\sum_{i=1}^{N_{tasks}} \mathbb{1}(\mathbf{p}_i \in \mathcal{W}_R)}{N_{tasks}} \times 100\% \tag{2.10}$$

where $\mathbf{p}_i$ represents required positions for functional tasks and $\mathbb{1}(\cdot)$ is the indicator function. The methodology requires coverage $\geq 95\%$ to ensure adequate functional support (PDS performance requirement).

Dynamic Modeling and Force Analysis

The equations of motion for constrained multibody systems are derived using Lagrange's equations with multipliers [95]:

$$\frac{d}{dt}\left(\frac{\partial T}{\partial \dot{\mathbf{q}}}\right) - \frac{\partial T}{\partial \mathbf{q}} + \frac{\partial V}{\partial \mathbf{q}} = \mathbf{Q} + \Phi_{\mathbf{q}}^{T}\lambda \tag{2.11}$$

where T is the kinetic energy, V is the potential energy, $\mathbf{Q}$ represents generalized forces, and λ is the vector of Lagrange multipliers associated with the constraint forces.

For a system of rigid bodies, the equations of motion can be written in the standard form [94]:

$$\mathbf{M}(\mathbf{q})\ddot{\mathbf{q}} + \Phi_{\mathbf{q}}^{T}\lambda = \mathbf{Q}_{applied} + \mathbf{Q}_{gravity} + \mathbf{Q}_{velocity} \tag{2.12}$$

where $\mathbf{M}(\mathbf{q})$ is the generalized mass matrix, $\Phi_{\mathbf{q}}^{T}\lambda$ represents constraint forces, $\mathbf{Q}_{applied}$ includes applied forces and torques (actuator and human contributions), $\mathbf{Q}_{gravity}$ contains gravitational effects, and $\mathbf{Q}_{velocity}$ includes velocity-dependent terms (Coriolis and centrifugal effects).

The generalized mass matrix for body i is given by [95]:

$$\mathbf{M}^{i} = \begin{bmatrix} m^{i}\mathbf{I}_{3\times 3} & \mathbf{0} \\ \mathbf{0} & \mathbf{J}^{i} \end{bmatrix} \tag{2.13}$$

where m^{i} is the mass of body i, $\mathbf{I}_{3\times 3}$ is the 3×3 identity matrix, and $\mathbf{J}^{i}$ is the inertia tensor in the global reference frame.

For gravity compensation assistance strategies, the gravitational force vector for body i is [94]:

$$\mathbf{Q}_{gravity}^{i} = \begin{bmatrix} m^{i}g\hat{\mathbf{z}} \\ (\bar{\mathbf{u}}^{COM})^{\times}\mathbf{A}^{iT}m^{i}g\hat{\mathbf{z}} \end{bmatrix} \tag{2.14}$$

where g is gravitational acceleration, $\hat{\mathbf{z}}$ is the vertical unit vector, $\bar{\mathbf{u}}^{COM}$ is the local position vector of the center of mass, and $(\cdot)^{\times}$ denotes the skew-symmetric matrix operator.

Anthropometric parameters (segment masses, lengths, inertias) are adapted based on user characteristics using standardized biomechanical datasets [96], enabling personalized performance prediction. Table 2.4 presents the anthropometric scaling relationships employed in the methodology.

Table 2.4 Anthropometric scaling relationships for upper limb segment parameters based on total body mass M and height H.

Segment	Length	Mass	COM Location
Upper Arm	$L_{ua} = 0.186 \times H$	$m_{ua} = 0.028 \times M$	$0.436 \times L_{ua}$ from shoulder
Forearm	$L_{fa} = 0.146 \times H$	$m_{fa} = 0.016 \times M$	$0.430 \times L_{fa}$ from elbow
Hand	$L_h = 0.108 \times H$	$m_h = 0.006 \times M$	$0.506 \times L_h$ from wrist

The differential-algebraic equations (DAE) resulting from constrained multibody dynamics require specialized numerical methods. Following Haug [94], the system can be solved using coordinate partitioning or augmented formulation approaches.

In the augmented formulation, the equations of motion (Eq. 2.12) are combined with the acceleration constraint equations (Eq. 2.7):

$$\begin{bmatrix} \mathbf{M} & \Phi_{\mathbf{q}}^T \\ \Phi_{\mathbf{q}} & \mathbf{0} \end{bmatrix} \begin{bmatrix} \ddot{\mathbf{q}} \\ \lambda \end{bmatrix} = \begin{bmatrix} \mathbf{Q} \\ \gamma \end{bmatrix} \tag{2.15}$$

where $\gamma = -(\Phi_{\mathbf{q}}\dot{\mathbf{q}})_{\mathbf{q}}\dot{\mathbf{q}} - 2\Phi_{\mathbf{q}t}\dot{\mathbf{q}} - \Phi_{tt}$ is the right-hand side of the acceleration constraint equation.

For systems with singular or ill-conditioned Jacobian matrices, singular value decomposition (SVD) provides robust numerical solutions [94]. Given $\Phi_{\mathbf{q}} = \mathbf{U}\Sigma\mathbf{V}^T$, the solution is obtained using the pseudoinverse when the condition number exceeds acceptable limits.

2.3.2 Numerical Implementation

Mathematical models require numerical implementation for practical application. The selection of computational tools depends on project-specific requirements balancing simulation fidelity, computational efficiency, available expertise, and integration with existing development environments.

General-Purpose Platforms: MATLAB/Simulink, Python with scientific libraries (NumPy, SciPy), and Mathematica provide comprehensive toolboxes for kinematics, dynamics, and optimization. These platforms offer rapid prototyping capabilities and extensive documentation supporting systematic model development.

Specialized Simulation Environments: Domain-specific tools may offer advantages for particular analysis types:

- OpenSim for musculoskeletal modeling with validated anatomical models;
- PyBullet or MuJoCo for physics-based dynamic simulation with contact modeling;

- ROS (Robot Operating System) for integration with physical hardware and real-time control.

Implementation Requirements: Regardless of platform, implementations should include forward kinematics with anthropometric scaling, constraint solving for closed-loop mechanisms (Section 2.3.1), workspace analysis tools, dynamic simulation capabilities, and optimization interfaces for parameter refinement.

The modeling framework enables iterative design refinement through parametric studies systematically exploring the design space. Computational design exploration reduces development time compared to purely experimental approaches by identifying optimal configurations before physical prototyping. Chapter 3 demonstrates specific implementation choices and their application to the coordinated shoulder-elbow exoskeleton development.

2.3.3 Parametric CAD Design

Following validation of the conceptual design through mathematical modeling (Section 3.3), the systematic methodology transitions to detailed design through parametric Computer-Aided Design (CAD) environments. This phase represents the critical bridge between abstract mathematical models and physical implementation, transforming validated concepts into manufacturable systems while maintaining traceability to initial specifications [84].

The parametric CAD phase serves concurrent objectives within the systematic framework: (1) translation of MCDM-selected concepts and mathematical models into three-dimensional solid models with complete geometric definition, (2) systematic selection and integration of commercial off-the-shelf (COTS) components including actuators, sensors, and structural materials, (3) specification of mechanical and electronic interfaces ensuring compatibility and modularity, and (4) application of parametric constraints enabling rapid design iteration without manual geometry reconstruction [97].

Component Selection Strategy: The component selection process follows directly from mathematical modeling results. Actuator sizing is driven by predicted torque and force requirements from dynamic simulations (Section 2.3.1), with appropriate safety factors applied to account for model uncertainties. Material selection integrates multiple PDS criteria (Section 2.2.1): structural materials must provide adequate stiffness while minimizing mass for portability, interface materials must satisfy biocompatibility standards (ISO 10993), and manufacturing constraints influence selection between metallic alloys, engineering polymers, and composite materials [98]. Sensor selection is informed by measurement requirements: force/torque sensors must provide adequate resolution to detect user intentions (typically

$<$ 1 N) while maintaining sufficient range for assistance forces (20-50 N for upper limb applications) [28].

Parametric Modeling Approach: The parametric CAD environment enables systematic exploration of design variants through constraint-based modeling. Key geometric parameters identified during MCDM evaluation and mathematical modeling, such as cable routing geometry, anchor point positions, link lengths, and interface dimensions, are defined as adjustable parameters rather than fixed dimensions. Parametric constraints maintain design intent throughout iterations: kinematic chains preserve degrees of freedom, assembly constraints ensure proper component mating, and geometric constraints enforce manufacturing limitations (minimum wall thicknesses, maximum feature sizes for additive manufacturing) [84].

The integration of parametric CAD with mathematical models enables bidirectional data exchange: geometric parameters from CAD models inform simulation refinements, while simulation results guide parametric adjustments. This iterative coupling ensures consistency between geometric design and predicted performance [94].

Virtual Assembly and Validation: Complete virtual assembly in the CAD environment verifies geometric compatibility and identifies potential interference before physical prototyping. Motion studies simulate the full range of motion specified in the PDS (Table 1.1), verifying that mechanical components do not collide during operation and that cable routing maintains adequate clearance throughout the workspace [97]. Mass properties calculated from the CAD assembly inform refined dynamic simulations, with actual component masses and inertias replacing initial estimates. Discrepancies between predicted and required performance trigger parametric adjustments, establishing an iterative loop between CAD design and simulation until specifications are satisfied.

Design for Manufacturing: Design for manufacturing (DFM) principles guide detailed design decisions to ensure producibility while maintaining functional requirements. Part consolidation reduces assembly complexity where appropriate, while complex geometries may be decomposed into simpler components for cost-effective production. Tolerance analysis ensures that accumulated manufacturing variations do not compromise functional requirements: critical dimensions affecting performance (e.g., cable anchor point positions influencing workspace coverage) receive tight tolerances, while non-critical dimensions utilize standard manufacturing tolerances [84].

Documentation and Traceability: Complete CAD documentation maintains traceability from requirements through implementation. Each component includes metadata linking to relevant PDS specifications, MCDM evaluation criteria, and mathematical model parameters.

Engineering drawings extracted from CAD models provide manufacturing specifications, assembly instructions, and quality control requirements [89].

The integration of parametric CAD with mathematical modeling and simulation establishes a digital twin of the physical system before prototyping, enabling comprehensive evaluation of mechanical, electrical, and control subsystems in an integrated environment. This virtual prototyping approach substantially reduces development iterations and accelerates transition to physical validation [83]. Chapter 3 demonstrates this parametric CAD methodology through detailed design of a coordinated shoulder-elbow exoskeleton, illustrating how systematic application of these principles translates conceptual designs into validated physical implementations.

2.3.4 Control strategies

Rehabilitation exoskeletons require control strategies that balance assistance provision, user safety, natural movement coordination, and adaptation to individual characteristics [99]. Control strategy selection depends on device characteristics, intended application, available sensing modalities, and therapeutic objectives. This section presents three main control families applicable to upper-limb rehabilitation exoskeletons.

Trajectory-based control

This type of control implements pre-defined motion profiles, guiding the user's limb through prescribed paths. The reference trajectory $\mathbf{q}_{ref}(t)$ is generated offline based on anatomical range-of-motion measurements, task-specific functional movement patterns, or therapist-defined exercise protocols.

Implementation approaches include position control with direct trajectory tracking using PID or feedforward methods, synchronized multi-joint movements maintaining specific kinematic relationships, and cyclical patterns for motor learning and neuromuscular conditioning.

This approach suits passive mobilization for severely impaired patients with minimal voluntary control, early-stage rehabilitation focusing on range-of-motion recovery, and structured exercise protocols requiring specific movement patterns [33]. Primary limitations include lack of adaptation to patient voluntary effort or recovery progress, risk of patient passivity, and limited engagement compared to active approaches.

Assist-as-needed control

These control strategies modulate assistance magnitude based on patient performance, providing minimal necessary support for successful task completion. This approach promotes active participation and motor learning by avoiding over-assistance [99].

Impedance control regulates the dynamic relationship between position deviations and interaction forces [30]:

$$\mathbf{F}_{interaction} = \mathbf{M}_d(\ddot{\mathbf{x}}_d - \ddot{\mathbf{x}}) + \mathbf{B}_d(\dot{\mathbf{x}}_d - \dot{\mathbf{x}}) + \mathbf{K}_d(\mathbf{x}_d - \mathbf{x}) \tag{2.16}$$

where $\mathbf{M}_d$, $\mathbf{B}_d$, and $\mathbf{K}_d$ represent desired inertia, damping, and stiffness matrices tuned based on user needs and rehabilitation phase. High stiffness provides strong guidance suitable for severely impaired patients, while low stiffness encourages voluntary effort. This framework applies to rigid exoskeletons requiring compliant interaction and position-controlled systems where force is the controlled output.

Admittance control implements the inverse relationship, regulating position response to measured forces [30]:

$$\mathbf{M}_d\ddot{\mathbf{x}} + \mathbf{B}_d\dot{\mathbf{x}} + \mathbf{K}_d(\mathbf{x} - \mathbf{x}_d) = \mathbf{F}_{measured} \tag{2.17}$$

where $\mathbf{F}_{measured}$ represents forces measured through load cells or cable tension sensors. The desired trajectory is computed from measured forces, then tracked using inner-loop position control. This approach particularly suits cable-driven systems where direct cable force measurement is available and soft exoskeletons with inherent mechanical compliance. Direct force measurement improves robustness to model uncertainties and provides intuitive patient interaction.

Virtual force fields guide movements without rigid trajectory constraints [100]:

$$\mathbf{F}_{assist} = -k_{tunnel} \cdot \mathbf{d}(\mathbf{x}, \mathscr{P}_{desired}) \tag{2.18}$$

where $\mathbf{d}(\mathbf{x}, \mathscr{P}_{desired})$ is the distance from current position to the desired path, and k_{tunnel} determines compliance. This enables task-oriented training where multiple movement strategies are acceptable and progressive assistance reduction through parameter adjustment.

Intent-based control

This control detects and amplify patient voluntary movement intentions, enabling intuitive control interfaces.

Surface electromyography signals from target muscles estimate movement intention:

$$\mathbf{F}_{assist} = \mathbf{G}_{emg} \cdot \phi(\mathbf{s}_{EMG}) \tag{2.19}$$

where $\mathbf{s}_{EMG}$ are processed EMG signals, $\phi(\cdot)$ is a mapping function, and $\mathbf{G}_{emg}$ is a gain matrix. This approach enables direct detection of neuromuscular activation intent and control

even with minimal voluntary movement capability. Implementation requires careful electrode placement following standardized protocols [101], signal conditioning, and feature extraction for robust intent detection. Signal reliability can be affected by electrode placement, skin impedance, and motion artifacts.

Interaction forces measured at the human-robot interface indicate movement intentions:

$$\mathbf{v}_{desired} = \alpha_{intent} \cdot \mathbf{F}_{interaction} \tag{2.20}$$

where α_{intent} maps forces to desired velocities. This provides robust sensing without skin preparation requirements and natural patient interaction through push/pull indications.

Model-based intent estimation uses observed kinematics to infer movement intentions:

$$\hat{\tau}_{voluntary} = \tau_{measured} - \tau_{model}(\mathbf{q}, \dot{\mathbf{q}}, \ddot{\mathbf{q}}) \tag{2.21}$$

where τ_{model} represents predicted passive dynamics and the residual indicates voluntary effort.

Model-based assistance strategies

These control strategy approaches leverage mathematical models of system dynamics and human biomechanics to predict required assistance and compensate for known disturbances.

Gravity compensation reduces muscle effort required to support limb weight [100]:

$$\tau_{gravity} = \mathbf{f}_{grav}(\mathbf{q}, \theta_{anthro}) \tag{2.22}$$

where $\mathbf{q}$ represents joint angles and θ_{anthro} contains anthropometric parameters. Adjustable assistance levels enable progressive rehabilitation:

$$\tau_{assist} = \alpha \cdot \tau_{gravity}(\mathbf{q}) \tag{2.23}$$

where $\alpha \in [0,1]$ can be manually adjusted by therapists, adapted automatically based on performance metrics, or scheduled according to rehabilitation phase. Progressive assistance reduction implements assist-as-needed principles [99].

Feedforward compensation combines model-based predictions with feedback control:

$$\mathbf{F}_{actuator} = \mathbf{F}_{feedforward}(\mathbf{q}, \dot{\mathbf{q}}, \ddot{\mathbf{q}}, \theta) + \mathbf{F}_{feedback}(\mathbf{e}) \tag{2.24}$$

where feedforward terms predict required forces based on kinematic state and model parameters, while feedback terms correct for uncertainties and disturbances. This approach reduces tracking error and provides smoother actuation but requires accurate system identification and real-time computation of forward dynamics.

Robustness and safety considerations

Control strategies must handle uncertainties typical of rehabilitation settings due to human variability and unmodeled dynamics. Model-based control depends on estimated body parameters with typical uncertainties in segment mass, center of mass location, and length measurements. Friction, cable stiffness, and joint properties vary with temperature, wear, and individual differences, limiting accuracy of feedforward and model-based controllers.

Robustness can be improved through robust control schemes, force-based admittance control to reduce model dependence, and disturbance observers to estimate external forces. Independent safety mechanisms ensure safe human-robot interaction [28]. Actuator forces are limited within safe bounds, joint motion is constrained within anatomical limits with appropriate safety margins, and emergency stop mechanisms trigger immediate force release through hardware and software layers. Actuation is mechanically decoupled via fail-safe elements such as clutches or spring releases [102].

Control strategy selection framework

Table 2.5 summarizes selection criteria for control strategies based on application requirements, patient characteristics, and available sensing capabilities.

Table 2.5 Control strategy selection based on application requirements.

Application	**Patient Impairment**	**Recommended Strategy**	**Key Requirements**
Passive ROM	Severe (no voluntary control)	Trajectory-based position control	Safe workspace limits, slow velocities
Active-assisted ROM	Moderate impairment	Admittance control with partial gravity compensation	Force sensors, adjustable assistance
Task-oriented training	Mild-moderate impairment	Force-field assistance or impedance control	Performance metrics, adaptive parameters
Functional activities	Mild impairment	Intent-based (EMG or force)	EMG system or force sensors, real-time processing
Neuromuscular re-education	Variable impairment	EMG-driven proportional control	Multi-channel EMG, patient-specific calibration

The selection and tuning of control parameters must consider device-specific characteristics, user population characteristics, and therapeutic objectives. Chapter 3 demonstrates the application of these control principles to a specific coordinated shoulder-elbow exoskeleton implementation.

2.3.5 Experimental validation

Systematic validation ensures devices meet design requirements and provides evidence of safety and effectiveness. The validation process progresses from component testing to human trials, following established frameworks for medical device development [88; 103]. Current standardization efforts through ASTM F48 [104] and ISO Technical Committee 299 aim to harmonize validation methodologies across industrial, medical, and consumer exoskeleton applications.

Component-level validation

Individual components require characterization before system integration. ISO 9283 [105] provides standardized methods for industrial robot performance testing applicable to exoskeleton actuators, including pose accuracy, repeatability, and response characteristics. Sensors undergo multi-point calibration following manufacturer specifications and relevant metrology standards. Communication systems are evaluated for latency and reliability to confirm real-time performance requirements necessary for safe human-robot interaction.

System integration testing

Integrated subsystems are tested to verify coordinated operation and safety compliance. ISO 13482 [28] specifies safety requirements for physical assistant robots including exoskeletons, addressing risk assessment, hazard identification, and protective measures. Control performance assessment through step and frequency response testing evaluates stability and tracking accuracy. Safety verification confirms force limiting mechanisms, workspace boundaries, and emergency stop functionality meet specified requirements.

Benchtop validation

Pre-clinical testing with anthropomorphic fixtures or test apparatus provides controlled evaluation before human trials. The Position and Load Test Apparatus for Exoskeletons (PoLoTAE) developed by NIST [106] demonstrates systematic benchtop validation approaches for load handling and positioning tasks. Workspace validation compares measured motion ranges to kinematic model predictions. Force transmission characteristics validate actuator performance against design specifications. Durability assessment through cyclic testing identifies potential failure modes and establishes maintenance requirements.

Human subject validation

Human trials assess usability, safety, and effectiveness following appropriate ethical approval protocols and institutional review board oversight [104]. Validation methodologies depend on device classification and intended application context.

Kinematic analysis through motion capture or inertial measurement units quantifies trajectory accuracy and movement quality. Force and torque measurements validate assistance delivery and human-robot interaction forces. Physiological assessment via surface electromyography evaluates neuromuscular activation patterns, with reduced activation levels indicating effective assistance [7]. Metabolic assessment through oxygen consumption measurement provides comprehensive quantification of physical demand reduction [107].

Functional task performance measures capability improvements during standardized activities relevant to intended application. Subjective assessments through validated questionnaires evaluate user experience, comfort, and perceived exertion. Statistical analysis with appropriate sample size determination based on power analysis and effect size quantification establishes practical relevance of observed outcomes.

Table 2.6 presents validation categories and assessment approaches based on established methodologies from industrial robot testing [105], personal care robot safety standards [28], and emerging exoskeleton-specific protocols [104; 106].

Table 2.6 Validation categories and assessment methods for exoskeleton systems based on established standards and testing protocols.

Category	**Representative Metrics**	**Assessment Method**
Kinematic	Trajectory accuracy, workspace coverage, movement precision	Motion capture, IMU-based analysis, pose measurement per ISO 9283 [105]
Force	Actuator force accuracy, assistance consistency, interaction forces	Calibrated load cells, multi-point calibration, force plate measurement
Physiological	Muscle activation patterns, metabolic demand, cardiovascular response	Surface EMG analysis [7], oxygen consumption measurement [107], heart rate monitoring
Functional	Task completion time, movement quality, functional capacity	Standardized functional assessments, task-specific performance metrics
Safety	Emergency response, force compliance, hazard mitigation	Safety testing per ISO 13482 [28], response time measurement, risk assessment per ISO 14971 [103]
Usability	User comfort, perceived exertion, acceptance	Validated questionnaires, subjective rating scales, user feedback protocols

This validation framework provides structured progression from technical verification to human assessment, ensuring system reliability and clinical relevance. Specific acceptance criteria and validation protocols depend on device classification, intended application, regulatory requirements, and target user population. Chapter 4 demonstrates application of these validation principles to the coordinated shoulder-elbow exoskeleton case study.

2.4 Workflow integration

The proposed methodology integrates all development phases through a structured workflow ensuring traceability from requirements to validated implementation (Figure 2.1). The sequence follows:

$$\text{Specification} \rightarrow \text{Analysis} \rightarrow \text{Selection} \rightarrow \text{Design} \rightarrow \text{Validation}$$

Each phase produces documented outputs informing subsequent stages. The Product Design Specification defines requirements and acceptance criteria, MCDM analysis identifies optimal design alternatives, mathematical modeling predicts system performance, and validation compares measured and predicted results. Requirements are traced throughout, maintaining consistency and compliance [89].

Explicit checkpoints guide iteration when specifications require revision, modeling fails to meet targets, or sensitivity analysis indicates close MCDM scores [84]. The framework builds on proven elements including systematic literature review [22], MCDM techniques [90; 91], biomechanical modeling [94; 95], and established validation procedures [88; 99].

Chapter 3 demonstrates methodology application through a coordinated shoulder-elbow exoskeleton case study, illustrating translation of requirements into functional specifications, MCDM-based concept selection, model-driven parameter optimization, and progressive validation from simulation to prototype testing. Performance assessment verifies compliance with PDS targets and improvements over current limitations identified in Section 1.4.

The framework supports transparent, reproducible, and multidisciplinary design through quantitative documentation enabling knowledge transfer, explicit weighting criteria reducing subjective bias, feedback loops ensuring controlled iteration, and common evaluation criteria facilitating collaboration. While developed for upper-limb rehabilitation exoskeletons, the workflow generalizes to other wearable assistive devices through adaptation of criteria, model fidelity, and validation depth [87]. Specifically, Steps 1–3 (requirements elicitation, PDS, and MCDM) are architecture-agnostic, while Steps 4–6 (kinematic/dynamic modeling and sizing) require adaptation to the target transmission and actuation principles.

Chapter 3

Methodology Application: A Design Case of Study

This chapter illustrates the practical implementation of the systematic design methodology (Chapter 2) through a coordinated shoulder-elbow cable-driven exosuit case study. Design and prototype development were conducted at Heidelberg University in Prof. Lorenzo Masia's laboratory. The implementation addresses key research gaps identified in Chapter 1: multi-joint coordination, sensing integration, and portable assistive solutions.

3.1 Requirements Definition

Following the methodology of Chapter 2, this section defines Product Design Specifications (PDS) for a novel coordinated shoulder-elbow cable-driven exosuit addressing fundamental limitations in portable upper-limb rehabilitation devices. The system targets individuals with upper-limb motor impairments affecting activities of daily living due to neurological, musculoskeletal, or age-related conditions who retain voluntary movement but require gravitational compensation during functional tasks.

The novel exosuit addresses critical requirements absent in existing single-joint architectures: coordinated 3-DOF assistance (shoulder flexion/extension, abduction/adduction, elbow flexion/extension) with extended functional workspace enabling natural ADL movements, portable form factor suitable for home-based rehabilitation (target mass $\leq$3.5 kg), and preserved range of motion (0-90° across all actuated DoF) ensuring kinematic compatibility with functional tasks. These requirements drive systematic design decisions detailed in subsequent sections, where multi-joint coordination necessitates novel sensing and control strategies resolving fundamental trade-offs constraining conventional single-joint paradigms.

3.1.1 Product Design Specifications

Table 3.1 summarizes the PDS according to the framework in Section 2.2.1. Specifications are grouped into eight categories: Functional, Performance, Dimensional, Actuation & Sensing, Usability, Safety, Environmental, and Manufacturing considerations.

Table 3.1 PDS for coordinated shoulder-elbow cable-driven exosuit case study.

Category	Parameter	Specification Criteria
Functional	Main Function	Multi-DoF gravitational compensation for coordinated shoulder-elbow assistance during ADL tasks
	Target Joints	Shoulder (2 DoF: flexion/extension, abduction/adduction) and Elbow (1 DoF: flexion/extension)
	Assistance Type	Admittance control with personalized biomechanical modeling for the user's movement intentions
	Movement Patterns	Coordinated multi-joint movements for functional ADL tasks (reaching, feeding, object manipulation)
Performance	Range of Motion	Minimum RoM: Shoulder flex/ext 0°-90°, Shoulder abd/add 0°-90°, Elbow flex/ext 0°-90°. Target: Preserve FRoM requirements
	Torque	Shoulder: 4-6 Nm at anchor point (15-25 Nm at glenohumeral joint). Elbow: 3-5 Nm at anchor point (8-15 Nm at elbow joint)
	Workspace Coverage	Operational workspace $\geq$ 95% of functional workspace volume
Dimensional	Total Mass	Target: $\leq$ 3.5 kg; Maximum acceptable: $\leq$ 5 kg (battery included)
	Dimensions	Centralized actuation unit: max 300 mm × 300 mm × 80 mm (back-mounted). Distributed interfaces: lightweight bracelets
	Mass Distribution	Centralized actuation unit on ergonomic harness platform. Lightweight distributed limb interfaces
	Form Factor	Wearable, portable design compatible with normal clothing to support user acceptance
Actuation & Sensing	Actuation System	Cable-driven with centralized motor unit
	Sensing	Force sensor, IMU sensor
	Control Architecture	Microcontroller system: sensing + real-time control
Usability	Donning/Doffing	Independent donning and doffing without external assistance
	Adjustability	Tool-free anthropometric adjustment system (straps, buckles) accommodating variable users
	Interface Design	Dynamic soft bracelet interfaces for shoulder and elbow attachment. No rigid mechanical joints constraining natural motion
	Portability	Fully portable, battery-powered with no external infrastructure. Operational duration: $\geq$ 2 hours continuous use
Safety	Emergency Stop	Hardware-implemented emergency stop mechanism
Environmental	Operating Conditions	Ambient temperature: 15°–30°C. Relative humidity: 20–80% (typical indoor conditions)
	Durability	$\geq$ 500 operational hours. Periodic cable inspection protocol
Manufacturing & Materials	Structural Materials	Actuation unit and Brackets/interfaces: PLA/ABS (3D printed)
	Cable System	High-tensile Kevlar or Dyneema cables. Bowden cable conduit
	Interface Materials	Breathable technical fabrics (polyester mesh, nylon webbing). PE foam padding for pressure distribution
	Production Method	Commercial components with custom 3D-printed structures. Research prototype.

3.2 Concept Selection and Design

Following requirements definition (Section 3.1), this section applies the MCDM framework (Chapter 2, Section 2.2.2) to evaluate existing cable-driven solutions and systematically derive the integrated design concept for coordinated shoulder-elbow assistance.

3.2.1 Evaluation of Alternatives

Table 3.2 presents the MCDM evaluation comparing state-of-art cable-driven exosuit addressing shoulder or elbow assistance with the proposed integrated design. The evaluation employs the criteria framework defined in Chapter 2 (Table 2.2), with weights derived systematically from the PDS priorities established in Table 3.1.

The analysis considers two representative foundation technologies: FALCO [108], a cable-driven shoulder exosuit providing 2-DoF assistance (shoulder flexion/extension and abduction/adduction), and the myoelectric control framework by Lotti et al. [109], demonstrating effective cable-driven elbow assistance with force-based control. Both devices exemplify portable, cable-driven actuation with demonstrated efficacy for single-joint assistance, making them suitable foundation architectures for integrated multi-joint design.

Table 3.2 MCDM evaluation comparing cable-driven alternatives for multi-joint upper limb assistance. Weights (W_{C_i}) derive from PDS priorities; ratings (R_{iy}) calculated using explicit formulas detailed in text.

Alternative	**C1** (6)	**C2** (10)	**C3** (5)	**C4** (4)	**C5** (8)	**C6** (10)	**C7** (6)	**C8** (4)	**C9** (6)	**C10** (3)	**C11** (10)	**C12** (6)	**Score**
FALCO [108]	1.67	1	2	0.75	3	3	1	1	0	0	0.67	2	**106.7**
Lotti et al. [109]	2.94	1	2	0.85	3	3	0	0	1	0	0.33	2	**96.6**
Proposed Device	**1.43**	**1**	**2**	**0.90**	**3**	**3**	**1**	**1**	**1**	**0**	**1.00**	**2**	**122.6**

Rating Calculation Methodology

Each rating R_{iy} for alternative y on criterion i is calculated using explicit formulas ensuring objective, reproducible evaluation. The overall score follows the weighted sum approach with portability constraint:

$$Score_y = B_y \times \sum_{i=1}^{12} P_{iy} = B_y \times \sum_{i=1}^{12} (W_{C_i} \times R_{iy}) \tag{3.1}$$

where $B_y = R_{2y}$ (portability boolean) ensures non-portable devices receive zero score. Criterion-specific calculations follow.

C1 (Mass): Rated as inverse proportionality to device weight relative to maximum acceptable mass from PDS:

$$R_{1y} = \frac{M_{max}}{M_{dy}} \tag{3.2}$$

where $M_{max} = 5.0$ kg (PDS maximum acceptable mass, Table 3.1) and M_{dy} represents device mass. Applied values:

- FALCO: $M_d = 3.0$ kg (estimated shoulder-only configuration) $\rightarrow R_1 = 5.0/3.0 = 1.67$
- Lotti et al.: $M_d = 1.7$ kg (typical elbow exosuit mass [7]) $\rightarrow R_1 = 5.0/1.7 = 2.94$
- Proposed Device: $M_d = 3.5$ kg (design target, Table 3.1) $\rightarrow R_1 = 5.0/3.5 = 1.43$

C2 (Portability): Boolean criterion verifying untethered, battery-powered operation capability:

$$R_{2y} = \begin{cases} 1 & \text{if fully portable (battery-powered, no external infrastructure)} \\ 0 & \text{otherwise} \end{cases} \tag{3.3}$$

All evaluated alternatives achieve $R_2 = 1$ (fully portable).

C3 (Self-wearability): Evaluates independent donning/doffing capability on discrete scale:

$$R_{3y} = \begin{cases} 0 & \text{requires external assistance} \\ 1 & \text{difficult but achievable alone} \\ 2 & \text{easily achievable alone} \end{cases} \tag{3.4}$$

All cable-driven exosuit evaluated demonstrate self-donning capability through adjustable textile interfaces: $R_3 = 2$.

C4 (Available Torque): Compares effective assistive torque at anchor points against ADL requirements. For multi-DoF devices, rating reflects worst-case (minimum) torque capability across actuated joints:

$$R_{4y} = \min_{j \in \text{DoF}_y} \left(\frac{T_{available,j}}{T_{required,j}} \right) \tag{3.5}$$

where $T_{required}$ from PDS: shoulder = 6 Nm, elbow = 5 Nm (effective at anchor point). Applied calculations:

- FALCO: Estimated shoulder torque capability 4.5 Nm (typical cable-driven shoulder exosuit [53]) $\rightarrow R_4 = 4.5/6.0 = 0.75$

- Lotti et al.: Elbow assistance framework with demonstrated 3-5 Nm range [109], conservatively assume $T_{available} = 4.25$ Nm $\rightarrow R_4 = 4.25/5.0 = 0.85$
- Proposed Device: Design targets shoulder 4-6 Nm, elbow 3-5 Nm. Worst-case: elbow minimum 4.5 Nm average $\rightarrow R_4 = 4.5/5.0 = 0.90$

C5 (Stability of Fixing): Evaluates attachment security during dynamic movements on discrete scale:

$$R_{5y} = \begin{cases} 1 & \text{reported instability or detachment} \\ 2 & \text{stable for low-intensity activities} \\ 3 & \text{completely stable across full operational range} \end{cases} \tag{3.6}$$

All cable-driven soft architectures employ textile interfaces with proven stability through multiple attachment points: $R_5 = 3$.

C6 (Safety): Evaluates inherent safety characteristics and risk mitigation per ISO 13482 principles:

$$R_{6y} = \begin{cases} 1 & \text{serious safety concerns identified} \\ 2 & \text{few minor safety considerations} \\ 3 & \text{no significant safety issues} \end{cases} \tag{3.7}$$

Cable-driven soft architectures inherently limit injury risk through compliant force transmission: $R_6 = 3$ for all alternatives.

C7-C10 (DoF Coverage): Boolean indicators for functional capability across target joints:

$$R_{7y} = \begin{cases} 1 & \text{if shoulder flex/ext actuated} \\ 0 & \text{otherwise} \end{cases} \tag{3.8}$$

$$R_{8y} = \begin{cases} 1 & \text{if shoulder abd/add actuated} \\ 0 & \text{otherwise} \end{cases} \tag{3.9}$$

$$R_{9y} = \begin{cases} 1 & \text{if elbow flex/ext actuated} \\ 0 & \text{otherwise} \end{cases} \tag{3.10}$$

$$R_{10y} = \begin{cases} 1 & \text{if wrist mobility assisted} \\ 0 & \text{otherwise} \end{cases} \tag{3.11}$$

Applied ratings reflect documented capabilities: FALCO (shoulder only): $R_7 = 1, R_8 = 1, R_9 = 0, R_{10} = 0$; Lotti (elbow only): $R_7 = 0, R_8 = 0, R_9 = 1, R_{10} = 0$; Proposed Device (integrated shoulder-elbow): $R_7 = 1, R_8 = 1, R_9 = 1, R_{10} = 0$.

C11 (RoM vs FRoM Compliance): Evaluates workspace coverage relative to functional range requirements for ADL tasks. Critical criterion for rehabilitation efficacy, rated as average compliance across all potentially actuated DoF:

$$R_{11y} = \frac{1}{n_{total}} \sum_{l=1}^{n_{total}} x_{ly} \tag{3.12}$$

where $n_{total} = 3$ (shoulder flex/ext, shoulder abd/add, elbow flex/ext from PDS) and x_{ly} represents DoF-specific compliance:

$$x_{1y} = R_{7y} \times \frac{S_{fy}}{S_{ff}} \quad \text{(Shoulder Flexion/Extension)} \tag{3.13}$$

$$x_{2y} = R_{8y} \times \frac{S_{ay}}{S_{af}} \quad \text{(Shoulder Abduction/Adduction)} \tag{3.14}$$

$$x_{3y} = R_{9y} \times \frac{E_{fy}}{E_{ff}} \quad \text{(Elbow Flexion/Extension)} \tag{3.15}$$

with functional requirements (FRoM) from PDS: $S_{ff} = 90$ (shoulder flexion), $S_{af} = 90$ (shoulder abduction), $E_{ff} = 90$ (elbow flexion). Applied calculations:

- FALCO: Shoulder-only device with typical RoM 0°-90° for both shoulder DoF [108], no elbow actuation:

$$R_{11,FALCO} = \frac{1}{3}\left(1 \times \frac{90}{90} + 1 \times \frac{90}{90} + 0 \times \frac{0}{90}\right) = \frac{2}{3} = 0.67$$

- Lotti et al.: Elbow-only assistance with documented RoM 0°-90° [109], no shoulder actuation:

$$R_{11,Lotti} = \frac{1}{3}\left(0 \times \frac{0}{90} + 0 \times \frac{0}{90} + 1 \times \frac{90}{90}\right) = \frac{1}{3} = 0.33$$

- Proposed Device: Integrated 3-DoF design targeting full functional workspace coverage (Table 3.1):

$$R_{11,Proposed} = \frac{1}{3}\left(1 \times \frac{90}{90} + 1 \times \frac{90}{90} + 1 \times \frac{90}{90}\right) = \frac{3}{3} = 1.00$$

C12 (Control Complexity): Evaluates implementation and operational complexity on discrete scale:

$$R_{12y} = \begin{cases} 3 & \text{simple control (direct force/position mapping)} \\ 2 & \text{moderate complexity (force-based, myoelectric)} \\ 1 & \text{high complexity (adaptive AI, multi-modal fusion)} \end{cases} \tag{3.16}$$

All evaluated alternatives employ force-based or myoelectric control strategies requiring biomechanical modeling but proven implementable: $R_{12} = 2$ for all devices.

3.2.2 Design synthesis

The MCDM evaluation systematically identifies optimal design solutions by quantifying performance across weighted criteria derived from PDS priorities. Analysis of foundation systems reveals complementary strengths and critical gaps, guiding systematic synthesis of hybrid architecture.

Quantitative evaluation reveals fundamental limitations in single-joint approaches. FALCO (Total Score: 106.7) achieves complete DoF coverage for shoulder movements (C7=1, C8=1, weighted 6+4=10 points) with RoM compliance $R_{11} = 0.67$ reflecting adequate workspace for shoulder-specific tasks. However, absence of elbow actuation (C9=0, weight=6) fundamentally constrains multi-joint coordination capability. The criterion C11 calculation demonstrates that shoulder-only assistance addresses only 2 of 3 functional DoF required for ADL tasks, directly limiting workspace coverage criterion (C11, weight=10, highest individual weight).

Lotti et al. [109] (Total Score: 96.6) achieves superior portability through lightweight design ($M_d = 1.7$ kg, $R_1 = 2.94$, C1 weight=6) and demonstrates effective myoelectric control. However, lack of shoulder actuation (C7=0, C8=0, combined weight=10) severely restricts functional workspace, yielding $R_{11} = 0.33$. This rating demonstrates elbow-only assistance addresses only 1 of 3 functional DoF, resulting in the lowest C11 score despite effective elbow control implementation.

Both foundation systems achieve scores below the proposed device (122.6) primarily due to incomplete DoF coverage. The criterion C11 (RoM vs FRoM compliance, weight=10) explicitly quantifies how single-joint approaches fail to satisfy functional workspace requirements for coordinated ADL tasks, directly corresponding to Research Gap 1 identified in Section 1.4.

The MCDM framework guides systematic synthesis by identifying which architectural elements address weighted requirements most effectively. The C11 ratings ($R_{11,FALCO} = 0.67$, $R_{11,Lotti} = 0.33$) mathematically demonstrate that single-joint solutions cannot achieve full functional workspace coverage ($R_{11} = 1.0$ requires all three DoF actuated), directly driving the fundamental design decision to develop coordinated 3-DoF assistance. Criteria C7-C8 (shoulder assistance, combined weight=10) identify FALCO's cable-driven architecture with biomimetic dual-tendon routing [108] as optimal foundation for 2-DoF shoulder assistance. Criterion C9 (elbow assistance, weight=6) guides adoption of Lotti's force-based control principles [109] transferable to integrated architecture. Criterion C1 (mass, weight=6) establishes quantitative constraint: integrated architecture must target $M_d \leq 3.5$ kg (yielding $R_1 = 1.43$) to maintain acceptable portability despite 3-DoF complexity.

The MCDM-guided synthesis identifies a novel coordinated cable-driven shoulder-elbow exosuit architecture addressing quantified gaps in single-joint approaches. The system employs biomimetic dual-tendon shoulder actuation principles (validated by [108]) addressing C7-C8 (weight=10), force-based elbow control methodology (demonstrated by [109]) addressing C9 (weight=6), novel motor-proximal sensing enabling coordinated 3-DoF operation improving C11 from 0.67/0.33 to 1.00 (weight=10), and mass target Md $\leq$3.5 kg maintaining portable form factor. This novel integrated system achieves MCDM score of 122.6, representing 15% improvement over FALCO (106.7) and 27% improvement over Lotti (96.6), demonstrating systematic requirements-driven synthesis rather than incremental modification of existing systems.

3.3 Kinematic and Dynamic Modeling

Following concept selection (Section 3.2), mathematical modeling provides quantitative guidance for component selection and mechanical design of the novel shoulder-elbow exosuit. This section presents the kinematic and dynamic analyses that inform actuator specifications, cable sizing, and geometric parameter selection for the coordinated multi-joint architecture.

3.3.1 Kinematic Analysis and Cable System Design

The upper limb kinematic model employs a 3D multibody formulation with generalized coordinates describing shoulder and elbow joint configurations. The kinematic chain consists of two rigid body segments (upper arm and forearm) connected by revolute joints, with the shoulder fixed at the global reference frame origin.

The system configuration is described by 12 generalized coordinates:

$$\mathbf{q} = [\mathrm{p_{x1}}, \mathrm{p_{y1}}, \mathrm{p_{z1}}, \theta_{\mathrm{x1}}, \theta_{\mathrm{y1}}, \theta_{\mathrm{z1}}, \mathrm{p_{x2}}, \mathrm{p_{y2}}, \mathrm{p_{z2}}, \theta_{\mathrm{x2}}, \theta_{\mathrm{y2}}, \theta_{\mathrm{z2}}]^{\mathrm{T}} \tag{3.17}$$

where subscript 1 denotes upper arm segment and subscript 2 denotes forearm segment. Position coordinates (p_x, p_y, p_z) represent joint centers (elbow for segment 1, wrist for segment 2), while angular coordinates $(\theta_x, \theta_y, \theta_z)$ represent XYZ Euler angles describing segment orientations.

The forward kinematics relates joint angles to end-effector positions through constraint equations [94]. For the upper arm segment with length L_{ua}:

$$\mathrm{p_{x1}} = \mathrm{L_{ua}} \cos(\theta_{\mathrm{y1}}) \cos(\theta_{\mathrm{z1}}) \tag{3.18}$$

$$\mathrm{p_{y1}} = \mathrm{L_{ua}} [\cos(\theta_{\mathrm{z1}}) \sin(\theta_{\mathrm{x1}}) \sin(\theta_{\mathrm{y1}}) - \cos(\theta_{\mathrm{x1}}) \sin(\theta_{\mathrm{z1}})] \tag{3.19}$$

$$\mathrm{p_{z1}} = \mathrm{L_{ua}} [\sin(\theta_{\mathrm{x1}}) \sin(\theta_{\mathrm{z1}}) + \cos(\theta_{\mathrm{x1}}) \cos(\theta_{\mathrm{z1}}) \sin(\theta_{\mathrm{y1}})] \tag{3.20}$$

For the forearm segment with length L_{fa}, the wrist position is computed relative to the elbow through the expressions:

$$\mathrm{p_{x2}} = \mathrm{p_{x1}} + \mathrm{L_{fa}} \cos(\theta_{\mathrm{y2}}) \cos(\theta_{\mathrm{z2}}) \tag{3.21}$$

$$\mathrm{p_{y2}} = \mathrm{p_{y1}} + \mathrm{L_{fa}} [\cos(\theta_{\mathrm{z2}}) \sin(\theta_{\mathrm{x2}}) \sin(\theta_{\mathrm{y2}}) - \cos(\theta_{\mathrm{x2}}) \sin(\theta_{\mathrm{z2}})] \tag{3.22}$$

$$\mathrm{p_{z2}} = \mathrm{p_{z1}} + \mathrm{L_{fa}} [\sin(\theta_{\mathrm{x2}}) \sin(\theta_{\mathrm{z2}}) + \cos(\theta_{\mathrm{x2}}) \cos(\theta_{\mathrm{z2}}) \sin(\theta_{\mathrm{y2}})] \tag{3.23}$$

Segment parameters are scaled from population statistics using regression equations [96]. For a user with body height H [mm] and total body mass M_{body} [kg]:

$$\mathrm{L_{ua}} = 0.186 \cdot \mathrm{H}, \quad \mathrm{L_{fa}} = 0.146 \cdot \mathrm{H} \tag{3.24}$$

$$\mathrm{m_{ua}} = 0.028 \cdot \mathrm{M_{body}}, \quad \mathrm{m_{fa}} = 0.016 \cdot \mathrm{M_{body}}, \quad \mathrm{m_{hand}} = 0.006 \cdot \mathrm{M_{body}} \tag{3.25}$$

For a representative user with average anthropometry ($H = 1750$ mm, $M_{body} = 75$ kg), the computed parameters are: $L_{ua} = 325$ mm, $L_{fa} = 255$ mm, $m_{ua} = 2.1$ kg, $m_{fa} = 1.2$ kg, $m_{hand} = 0.45$ kg. These values serve as baseline for component sizing calculations presented in Subsection 3.3.1.

The kinematic model is implemented in MATLAB using a constraint-based formulation solved via Newton-Raphson iteration [94]. Representative ADL movements are simulated with prescribed angular velocities driving shoulder flexion/extension (θ_{y1}) and elbow flexion/extension (θ_{y2}) within the operational range 0°-90° specified in PDS (Table 3.1).

Figure 3.1 presents simulated trajectories for elbow and wrist positions during a reaching movement, illustrating the kinematic chain behavior and anchor point locations on upper arm and forearm segments positioned at 43% of segment length from proximal joints (biomechanical center of mass location [96]).

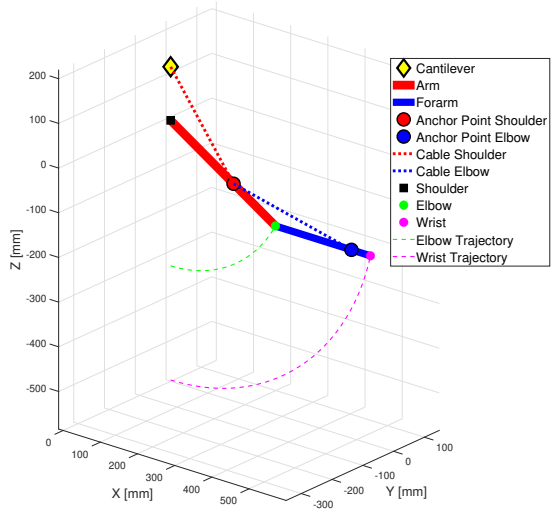

Figure 3.1 MATLAB simulation of shoulder-elbow kinematics during reaching movement. Elbow trajectory (green) and wrist trajectory (magenta) show coordinated multi-joint motion. Anchor points marked on upper arm and forearm. Cantilever mechanism positioned to avoid kinematic singularities during shoulder movements.

Cable Force Requirements and Component Sizing

Cable-driven architectures transmit assistive forces through high-tensile tendons, requiring careful force prediction for actuator and cable specification. This subsection derives required cable tensions from gravitational compensation requirements and translates these predictions into component specifications.

Cables transmit tension only, with the relationship between cable tension and joint torque involving configuration-dependent moment arms [110]:

$$\tau_{joint} = r(\mathbf{q}) \cdot F_{cable} \tag{3.26}$$

where τ_{joint} is the assistive torque, $r(\mathbf{q})$ is the moment arm (perpendicular distance from cable line of action to joint rotation axis), and F_{cable} is the cable tension. Real systems exhibit energy losses due to cable-conduit friction and pulley bearing losses. The effective torque accounting for transmission efficiency is:

$$\tau_{joint} = \eta_{trans} \cdot r(\mathbf{q}) \cdot F_{cable} \tag{3.27}$$

where $\eta_{trans} \in [0,1]$ represents transmission efficiency. For PTFE-lined Bowden cable systems, literature reports efficiency values $\eta_{trans} = 0.85$–0.95 [102; 111]. Conservative design value $\eta_{trans} = 0.88$ is adopted, providing safety margin against friction uncertainties.

Anchor point locations are determined following biomechanical heuristics established in musculoskeletal modeling literature. Positioning anchors at segment centers of mass (43% of segment length from proximal joint [96]) provides a pragmatic balance between mechanical efficiency and design robustness. This heuristic-based approach offers several advantages for cable-driven rehabilitation devices: adequate moment arm throughout workspace, kinematic compatibility that minimizes additional inertial effects during dynamic movements, mechanical simplicity that reduces stress on bracelet attachment structures, and consistent force transmission characteristics across the operational range.

For the representative user ($H = 1750$ mm, $M_{body} = 75$ kg):

- Upper arm anchor: $d_{ua,anchor} = 0.43 \times 325 = 140$ mm from shoulder
- Forearm anchor: $d_{fa,anchor} = 0.43 \times 255 = 110$ mm from elbow

MATLAB kinematic simulation across operational range ($\theta_{y1}, \theta_{y2} \in [0,90]$) confirms moment arms vary from 55 mm to 95 mm for shoulder (mean 75 mm) and from 25 mm to 78 mm for elbow (mean 51 mm), providing sufficient mechanical advantage for gravitational compensation with peak cable forces remaining below 120 N.

Required cable forces are predicted through inverse dynamics. The gravitational torque at the elbow joint, accounting for forearm and hand segments, is:

$$\tau_{elbow,gravity}(\theta_{y1}, \theta_{y2}) = \left[m_{fa} \cdot \frac{L_{fa}}{2} + m_{hand} \cdot L_{fa} \right] \cdot g \cdot \sin(\theta_{y1} + \theta_{y2}) \tag{3.28}$$

where θ_{y1} represents shoulder flexion angle (0° = vertical down, 90° = horizontal) and θ_{y2} represents elbow flexion angle relative to upper arm (0° = extended, 90° = perpendicular). The term $\theta_{y1} + \theta_{y2}$ gives the absolute forearm angle with respect to vertical. Maximum elbow torque occurs when the forearm is horizontal. For the representative user with shoulder maintained vertical ($\theta_{y1} = 0$) and elbow flexed to 90° ($\theta_{y2} = 90$, yielding horizontal forearm):

$$\tau_{elbow,max} = [1.2 \times 0.128 + 0.45 \times 0.255] \times 9.81 \approx 2.6 \text{ Nm} \tag{3.29}$$

For shoulder torque, accounting for upper arm segment plus extended forearm and hand contributions, maximum loading occurs at 90° shoulder flexion (horizontal arm configuration)

with elbow extended ($\theta_{y2} = 0$):

$$\tau_{shoulder,gravity}(\theta_{y1}) = \left[m_{ua} \cdot \frac{L_{ua}}{2} + (m_{fa} + m_{hand}) \cdot L_{ua} \right] \cdot g \cdot \sin(\theta_{y1}) \tag{3.30}$$

yielding maximum shoulder torque:

$$\tau_{shoulder,max} = [2.1 \times 0.163 + 1.65 \times 0.325] \times 9.81 \approx 7.8 \text{ Nm} \tag{3.31}$$

Figure 3.2 presents gravitational torques across the operational range. Shoulder torque reaches maximum 7.8 Nm at 90° flexion (Equation (3.31)), while elbow torque reaches maximum 2.6 Nm when forearm is horizontal (Equation (3.29)). The distinct profiles reflect different mass distributions and kinematic configurations: shoulder torque increases monotonically with flexion angle due to growing projection of the extended arm weight, while elbow torque (with shoulder maintained vertical) increases as the forearm rotates from vertical to horizontal orientation.

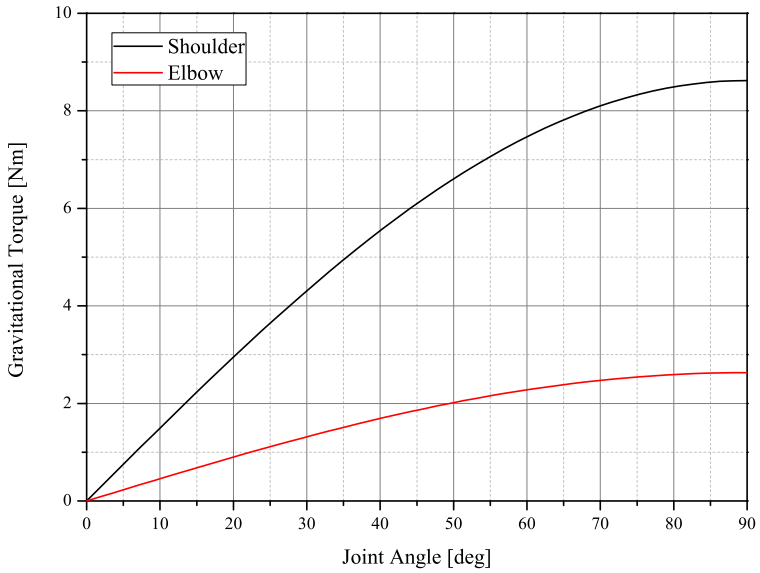

Figure 3.2 Gravitational torques over the 0°–90° range for a representative user ($H = 1750$ mm, $M_{body} = 75$ kg). Shoulder torque (blue, elbow at 0°) includes upper arm, forearm, and hand, peaking at 7.8 Nm at 90°. Elbow torque (red, shoulder at 0°) includes forearm and hand, peaking at 2.6 Nm at 90° with the forearm horizontal.

Inverting Equation (3.27):

$$F_{cable,required} = \frac{\tau_{gravity}}{\eta_{trans} \cdot r(\mathbf{q})} \tag{3.32}$$

Figure 3.3 translates gravitational torques into required cable forces using Equation (3.32). Cable forces depend on both gravitational torque (varying with $\sin(\theta)$) and moment arm (increasing approximately linearly from 55 to 95 mm for shoulder, 25 to 78 mm for elbow). Peak forces occur where the ratio $\tau_{gravity}/r(\mathbf{q})$ is maximum, which does not necessarily coincide with maximum torque due to the evolving moment arms. For shoulder subsystem, peak force occurs at approximately 73° flexion where the moment arm is approximately 75 mm:

$$F_{cable,shoulder,peak} \approx \frac{7.8}{0.88 \times 0.075} \approx 118 \text{ N} \tag{3.33}$$

For elbow subsystem with shoulder vertical, peak force occurs at approximately 61° relative elbow flexion where the moment arm is approximately 51 mm:

$$F_{cable,elbow,peak} \approx \frac{2.6}{0.88 \times 0.051} \approx 58 \text{ N} \tag{3.34}$$

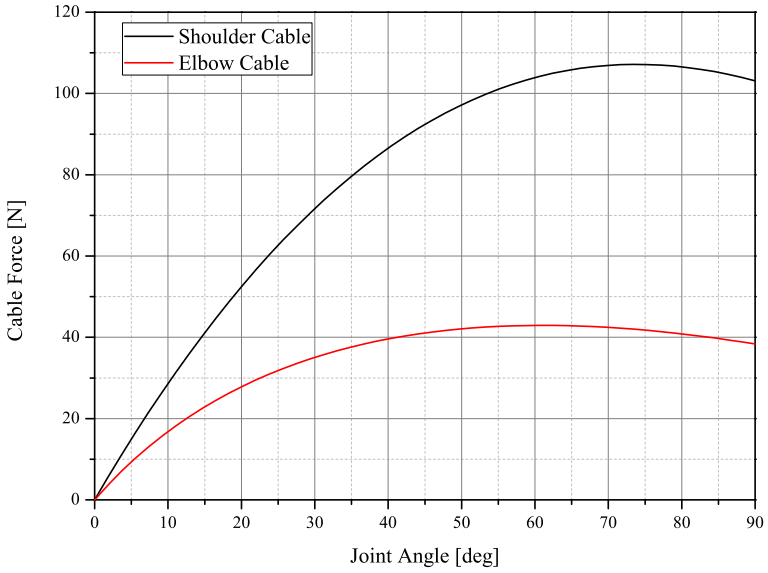

Figure 3.3 Required cable forces over 0°–90° for a representative user ($H = 1750$ mm, $M_{body} = 75$ kg). Shoulder (blue, elbow at 0°) and elbow (red, shoulder at 0°) forces peak at 118 N and 58 N, respectively, where $\tau_{gravity}/r(\mathbf{q})$ is maximal, with moment arms of 55–95 mm (shoulder) and 25–78 mm (elbow).

These worst-case values inform actuator sizing. Table 3.3 summarizes design parameters derived from mathematical modeling, providing quantitative guidance for component selection detailed in Section 3.4.

Table 3.3 Component specifications derived from mathematical modeling for representative user ($H = 1750$ mm, $M_{body} = 75$ kg) under worst-case loading conditions.

Parameter	**Description**	**Elbow**	**Shoulder**
Anthropometric Parameters			
Segment length	L [mm]	255	325
Segment mass	m [kg]	1.2	2.1
Anchor position	d_{anchor} [mm]	110 (43% L)	140 (43% L)
Dynamic Parameters			
Max gravitational torque	$\tau_{gravity,max}$ [Nm]	2.6	7.8
Configuration at max	[deg]	90°	90°
Moment arm range	r [mm]	25–78	55–95
Mean moment arm	$\bar{r}$ [mm]	51	75
Transmission efficiency	η_{trans} [-]	0.88	
Cable Force Requirements			
Peak cable tension	$F_{cable,peak}$ [N]	58	118
Configuration at peak	[deg]	$\sim$61°	$\sim$73°
Actuator Specifications			
Pulley radius	r_{pulley} [mm]	20	
Safety factor	SF [-]	1.5	
Required motor torque	τ_{motor} [Nm]	1.7	3.5
Selected motor rating	$\tau_{motor,rated}$ [Nm]	5.0–6.0	
Cable Specifications			
Material	High-tensile Kevlar		
Working load rating	[N]	> 150 (SF > 1.3)	
Diameter	[mm]	1.5–2.0	
Routing Specifications			
Conduit type	PTFE-lined Bowden cable		
Min pulley diameter	[mm]	40 (bending stress limit)	

Motor torque requirements are computed as:

$$\tau_{motor} = F_{cable} \cdot r_{pulley} \cdot SF \tag{3.35}$$

For peak cable forces with $r_{pulley} = 20$ mm and $SF = 1.5$:

$$\tau_{motor,shoulder} = 118 \times 0.020 \times 1.5 = 3.5 \text{ Nm} \tag{3.36}$$

$$\tau_{motor,elbow} = 58 \times 0.020 \times 1.5 = 1.7 \text{ Nm} \tag{3.37}$$

Selected brushless DC motors have rated torques 5.0–6.0 Nm, providing adequate capacity for worst-case loading scenarios across the anthropometric range (5th-95th percentile, body mass 60–90 kg) with appropriate safety margins.

Cable Routing Architecture

Cable routing geometry critically affects system performance, particularly for the shoulder subsystem where 2-DoF assistance (flexion/extension, abduction/adduction) requires careful consideration of cable departure points to maintain adequate mechanical advantage throughout the workspace.

The shoulder assistance employs a biomimetic dual-tendon routing strategy replicating deltoid force vector distribution [102]. The primary cable provides assistive force while a secondary cable adjusts force vector orientation via geometric reconfiguration. To enable 2-DoF shoulder assistance, the shoulder cable departs from a cantilever mechanism mounted on the centralized actuation unit (Figure 3.1).

The cantilever mechanism provides a fixed departure point offset from the vertical axis aligned with the glenohumeral joint. This geometric configuration ensures that: (1) cable routing path remains well-defined throughout 0°-90° shoulder abduction/adduction range, (2) moment arm for shoulder assistance maintains adequate magnitude across the workspace, and (3) cable does not wrap around torso during large shoulder movements. The cantilever departure point is positioned approximately 80 mm anterior and 150 mm superior relative to the glenohumeral joint center, ensuring geometric compatibility with the dual-tendon routing strategy and shoulder bracelet anchor point positioning (43% L_{ua} = 140 mm from shoulder).

The elbow actuation follows a simpler routing scheme, with the cable extending from the centralised drive unit along the upper arm to the forearm anchor point. The cable segment originates at the shoulder cuff anchor and terminates at the elbow anchor point (43% L_{fa} = 110 mm from elbow). The mechanism is designed to preserve consistent cable alignment throughout shoulder motion, ensuring smooth transmission and minimising friction or path deviation.

Placing anchor points at segment centers of mass (43% length) ensures sufficient mechanical advantage across the workspace. Moment arms range from 25 mm (elbow full extension) to 95 mm (shoulder near full flexion), with mean values of 51 mm (elbow) and 75 mm (shoulder). Peak cable forces remain below 120 N, within actuator (5–6 Nm) and cable limits. The most demanding case occurs at elbow full extension, yielding 118 N at 73° shoulder flexion, safely within design margins.

This geometry enables coordinated 2-DoF shoulder and 1-DoF elbow assistance while preserving kinematic compatibility with natural motion (Table 3.1).

3.4 CAD Design and Integration

Following the guidelines of conceptual design through mathematical modeling (Section 3.3), the systematic methodology transitions to detailed design through parametric Computer-Aided Design (CAD) environments. This phase represents the critical bridge between abstract mathematical models and physical implementation, transforming validated concepts into manufacturable systems while maintaining traceability to initial specifications [84; 97].

The CAD design phase is inherently iterative, as component selection decisions (actuators, sensors, structural materials) directly influence geometric constraints, interface designs, and routing strategies. This section documents the design evolution process, emphasizing the systematic approach to resolving technical challenges that emerged during integration of a novel coordinated multi-joint assistance within a portable, cable-driven architecture.

3.4.1 Component Selection

Component selection leverages force predictions from mathematical modeling (Section 3.3, Table 3.3) to identify commercial off-the-shelf (COTS) hardware meeting performance requirements while optimizing for mass, power consumption, and cost constraints.

- Actuator Selection: Brushless DC motors provide high power density and precise torque control for cable-driven systems. The AK60-6 brushless DC motor (T-Motor, China) was selected based on the following specifications: nominal torque of 3.0 Nm with a 6:1 reduction ratio, mass of 485 g, and CAN-bus interface enabling real-time torque and velocity control. Three AK60-6 motors provide actuation for: (1) primary shoulder flexion/extension and abduction/adduction assistance, (2) secondary shoulder force-vector orientation via cantilever rotation, and (3) elbow flexion/extension assistance. Integrated encoders enable closed-loop position control with 0.02° angular resolution, supporting precise cable-displacement tracking.

- Force Sensing: Load cells positioned motor-proximal (adjacent to the actuators) measure cable tension, with geometric compensation algorithms translating these measurements into anchor-point forces. Two miniature load cells (DYMH 103, China) are used, each with a capacity of 20 kg (196 N), suitable for both tension and compression measurement. The sensors are miniature rod-type units optimized for cable-tension applications and are interfaced through CJMCU-711 HX711 24-bit dual-channel analog-to-digital converter modules. The measurement range is 0–196 N, providing a safety factor greater than 3.6 relative to predicted peak loads of 54 N.

- Inertial Sensing: Two 6-axis inertial measurement units (IMU BMI085, Shuttle Board 3.0, Bosch Sensortec, Germany) are mounted on upper-arm and forearm bracelets to provide kinematic feedback. Each sensor integrates a 3-axis accelerometer and a 3-axis gyroscope and streams raw acceleration and angular-velocity data at 100 Hz. Data are transmitted wirelessly over Bluetooth using Adafruit Feather nRF52840 modules, which also perform quaternion computation on-board for real-time orientation tracking. This 6-axis configuration enables robust orientation estimation through sensor-fusion algorithms combining accelerometer and gyroscope data, preventing gimbal-lock issues associated with Euler angles and maintaining continuous kinematic tracking across the full operational range.

- Control Electronics: The control architecture is implemented on a single-board microcontroller platform that manages both sensor communication and motor commands. An Arduino MKR WiFi 1010 with an ARM Cortex-M0+ processor operating at 48 MHz executes the main control loop at 100 Hz. Load-cell signals are conditioned through an Arduino shield interfacing with HX711 amplifier modules for analog signal processing. IMU data are aggregated wirelessly via an Adafruit Feather module using a BLE UART protocol, which serves as the system's communication hub. Power is supplied by a 14.8 V, 3700 mAh LiPo battery, supporting more than two hours of continuous operation.

- Cable and Routing Components: The cable transmission system employs high-tensile Kevlar tendons to transfer forces from the centralized actuation unit to distributed anchor points on the limb segments. The tendons consist of 1.0 mm diameter braided Kevlar filaments rated at 150 N ultimate tensile strength, providing adequate safety margin against the predicted peak cable tensions of 54 N from mathematical modeling (Section 3.3.1). Cable routing employs Shimano PTFE-lined Bowden conduit housings with 5.0 mm outer diameter and 1.6 mm internal diameter, minimizing frictional resistance while enabling complex three-dimensional routing paths from the posterior-mounted actuation unit to the shoulder and elbow anchor points. Force transmission within the actuation unit is managed through custom 50 mm diameter pulleys, fabricated via FDM 3D printing in PLA material for cable redirection.

Table 3.4 summarizes datasheet specifications for commercially-available components selected based on force predictions from mathematical modeling (Section 3.3.1). Custom mechanical components including actuation unit housing, cantilever mechanism, dual-pulley

slider, and wearable bracelets are fabricated via additive manufacturing (detailed in Section 3.6), enabling rapid design iteration and anthropometric customization.

Table 3.4 Datasheet specifications for commercial off-the-shelf (COTS) components.

Component	**Key Specifications**	**Qty**	**Manufacturer**
Actuation Subsystem			
AK60-6 Motor	Nominal torque: 3.0 Nm; Reduction: 6:1; Output torque: 18 Nm; Voltage: 24V; Encoder: 16384 cnt/rev; Interface: CAN bus	3	T-Motor, China
Force Sensing			
Load Cell DYMH 103	Capacity: 20 kg (196 N); Type: Miniature tension/compression; Output: Analog mV/V	2	Generic, China
HX711 ADC	Model: CJMCU-711; Resolution: 24-bit dual channel; Sample rate: 10-80 Hz; Interface: Serial	2	Generic, China
Inertial Sensing			
IMU BMI085	Model: Shuttle Board 3.0; Sensors: 6-axis (accel + gyro); Sample rate: 100 Hz; Interface: SPI/I2C	2	Bosch Sensortec, Germany
Feather BLE	MCU: nRF52840; Protocol: BLE UART; Voltage: 3.3V	2	Adafruit #4062, USA
Control Electronics			
Arduino MKR WiFi 1010	MCU: ARM Cortex-M0+ 48 MHz; Flash: 256 KB; RAM: 32 KB; Interface: WiFi, I2C, SPI, Serial	1	Arduino, Italy
Arduino Shield	Function: Prototyping board, load cell amplifier interface	1	Arduino, Italy
LiPo Battery	Voltage: 14.8V (4S); Capacity: 3700 mAh; Chemistry: Lithium Polymer	1	Generic
Cable System			
Kevlar Cable	Diameter: 1.0 mm; Breaking strength: 150 N; Material: Braided Kevlar	$\sim$ 4 m	Generic
Bowden Conduit	Outer diameter: 5.0 mm; Inner diameter: 1.6 mm; Liner: PTFE	$\sim$ 5 m	Shimano

Figure 3.4 presents the complete CAD assembly integrating commercial components with custom 3D-printed structures, illustrating overall system architecture and component positioning consistent with the preliminary results shown in project presentations.

The assembly also provides a clear visualization of subsystem interfaces and spatial constraints relevant to the final integration phase.

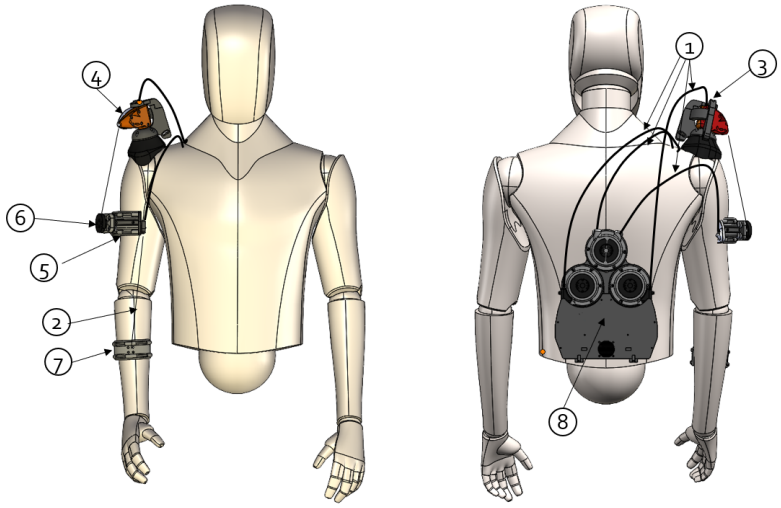

Figure 3.4 Complete CAD assembly overview: (1) Bowden cable; (2) Wire in Kevlar; (3) Mounting shoulder; (4) Cantilever; (5) Shoulder slider guide; (6) Shoulder anchor point; (7) Elbow anchor point; (8) Actuator system.

3.4.2 Wearable Interface Design

The wearable interface comprises textile-based bracelets securing cable anchor points to limb segments, integrated with 3D-printed mechanical components enabling force transmission and anthropometric adjustability. Design priorities include tool-free donning/doffing, comfort through compliant padding and pressure distribution, and kinematic transparency to minimize resistance during unpowered motion. This section presents the detailed CAD design of individual wearable components and their mechanical functionality.

Shoulder Bracelet with Integrated Slider Mechanism

The shoulder bracelet is a complex wearable component that integrates a dynamic sliding mechanism enabling coordinated shoulder assistance with two degrees of freedom: flexion/extension and abduction/adduction. The design addresses the biomechanical challenge of maintaining the optimal alignment of the anchor point throughout the shoulder's workspace, which is essential for the effective transmission of force vectors across multiple degrees of freedom. Figure 3.5 illustrates the detailed CAD model of the shoulder bracelet components.

The shoulder slider guide is an 80 mm linear guide arranged circumferentially around the upper arm. It is fabricated using FDM 3D printing in PLA to ensure structural rigidity.

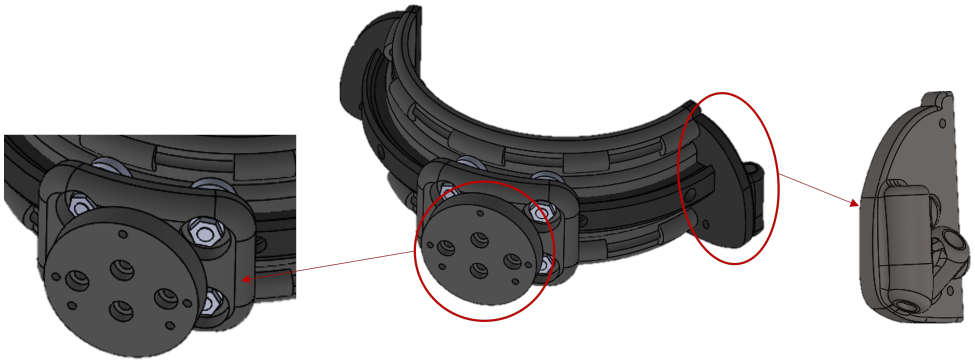

(a) (b) (c)

Figure 3.5 Shoulder bracelet CAD components: Shoulder slider guide circumferential rail (b), shoulder anchor point mounted on slider carriage (a), connector for elbow cable routing guidance (c).

The sliding carriage, shown in detail at the bottom of Figure 3.5, moves bidirectionally along the guide and houses the shoulder anchor point where the primary assist cable terminates. This anchor point is located at approximately 43% of the upper arm length from the center of the shoulder joint, corresponding to the optimal position described in Section 3.3.1.

The slider mechanism enables dynamic repositioning of the anchor point to accommodate the shoulder's second degree of freedom (abduction/adduction). A dedicated motor within the actuation unit (Section 3.4.3) drives the slider carriage through a dual-cable configuration: two cables connected to opposite ends of the carriage create bidirectional actuation. When the motor retracts one cable while extending the other, the slider translates along the guide rail, effectively moving the anchor point laterally (right or left) to maintain optimal force vector alignment as the user abducts or adducts the shoulder. This biomimetic mechanism replicates the deltoid muscle's anatomical force distribution pattern, where force direction varies with shoulder elevation angle to maximize torque throughout the movement range.

The shoulder bracelet also integrates a connector for the elbow cable (Figure 3.5 (c)), which serves as an intermediate routing point guiding the free cable from the actuation unit toward the elbow anchor point. This connector maintains appropriate cable geometry as the shoulder moves, preventing cable interference with the slider mechanism and ensuring the elbow cable follows a smooth path along the upper arm to reach the forearm bracelet. The connector features internal channels accommodating the Bowden conduit housing, maintaining cable displacement throughout shoulder and elbow coordinated movements.

The sliding guide assembly is mounted on a polyurethane cuff secured by a Boa® system, allowing quick, tool-free adjustment without Velcro. The cuff fits arm circumferences from 220 to 420 mm (5th–95th percentile). A 12 mm high-density polyurethane foam lining

distributes interface forces over contact areas such as the biceps muscle belly and tendon, reducing pressure peaks and improving comfort during prolonged use.

Elbow Bracelet Design

The elbow bracelet provides a simpler design compared to the shoulder bracelet, as elbow assistance requires only single-DoFflexion/extension support. The bracelet secures the elbow cable anchor point at approximately 43% of forearm length measured from the elbow joint center, positioning the anchor near the forearm's muscular bulk to optimize moment arm geometry for force transmission. The anchor point assembly consists of a rigid 3D-printed PLA structure with an ergonomic design that follows the contour of the forearm. Four holes allow the Kevlar tendon to be securely fastened. Similar to the shoulder cuff, it is mounted on a polyurethane cuff secured by a Boa® system, which provides customizable, quick, and tool-free adjustment. The cuff accommodates forearm circumferences ranging from 180 mm to 280 mm. The inner surface is lined with 12 mm high-density polyurethane foam padding, which is thinner than that of the shoulder cuff due to the lower interface forces expected on the forearm. The padding extends circumferentially to distribute pressure and prevent skin irritation during repetitive movements. Figure 3.6 presents the elbow bracelet CAD design and key features.

Figure 3.6 Elbow bracelet CAD design

Cantilever Mechanism

A cantilever mechanism, employing geometric principles validated through MCDM analysis (Section 3.2), was fabricated in PLA to provide a fixed reference point for the shoulder assistance cables. The cantilever establishes a rigid structural base transmitting cable forces to the shoulder cuff anchor point. Mounted on a rotary joint, it enables dynamic force vector orientation, following the secondary rotation of the mobile shoulder anchor point coordinated by the primary tendon. During preliminary testing, structural deflection introduced unwanted series elasticity into the transmission path, degrading control accuracy and increasing the risk of fatigue-induced failure. To address this issue, the structure was reinforced with an additional support component designed to minimise bending while

allowing free rotation of the cantilever. This support stabilised the mechanism and effectively eliminated flexural deformation. The Bowden cable is routed internally through the cantilever, providing a smooth guiding surface that directs the primary shoulder cable toward the cuff anchor point while minimising friction and wear. The guide geometry was optimised to maintain consistent cable exit angles across the cantilever's range of rotation ($\pm$30), ensuring that the cable path remains tangent to the guide surface without sharp curvature radii that could induce stress concentrations or friction losses. The reinforced cantilever design improved structural stiffness, reducing deflection under peak loads to $<$3 mm. This stiffness enhancement ensures accurate force transmission and reduces compliance-induced control challenges. Figure 3.7 illustrates the cantilever CAD design with mounting configuration, while Figure 3.8 presents finite element analysis results validating the structural performance under operational cable tensions.

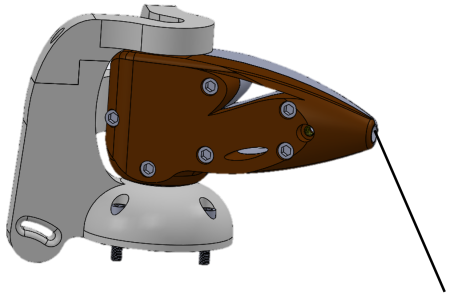

Figure 3.7 Cantilever mechanism: mounting configuration on rotary joint, structural reinforcement with additional support component, cable director geometry at distal end.

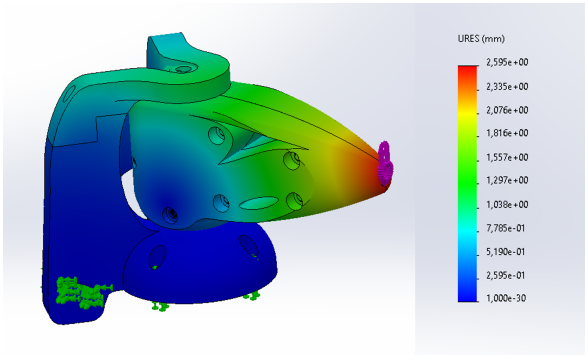

Figure 3.8 Finite element analysis of cantilever under 236 N cable tension: displacement field showing maximum deflection $<$2.6 mm at cable attachment point, fixed constraint at mounting boss (green), applied force at cable director (magenta).No permanent deformation is observed from the simulation.

3.4.3 Actuation Unit Development

The placement of the force sensor near the anchor point limited the available space for cable motion, thereby restricting the range of motion (RoM). To address this issue, the sensors were relocated from the anchor points to positions close to the motors, adjacent to the actuators. By moving the sensors proximally, it was possible to preserve the minimum RoM required for the three degrees of freedom. This configuration enabled an elbow flexion range of 0°–90° while maintaining a shoulder elevation range of 0°–90°, in accordance with the PDS specifications. Repositioning the sensors also required reinforcing the sensor housings to prevent material deformation and unwanted signal fluctuations. However, placing the sensors near the motors introduced a critical challenge: the measured forces at the pulleys differ from the effective forces at the anchor points due to configuration-dependent cable–limb interaction angles. This necessitated the development of geometric compensation algorithms (Section 3.5) to translate motor-proximal measurements into accurate anchor point force estimations.

The actuator unit houses the control electronics module, two force sensors integrated with pulley mechanisms for cable tension measurement, and three motors responsible for actuating the three degrees of freedom (DoFs). Each motor is equipped with a wire-winding pulley, one of which functions as a differential control pulley. Retracting cable A while extending cable B drives the cursor toward abduction, whereas reversing this action produces adduction. The unit also includes an onboard battery for autonomous operation. Figure 3.9 illustrates the CAD of complete actuation unit, integrating the motors, sensors, control electronics, and pulley system.

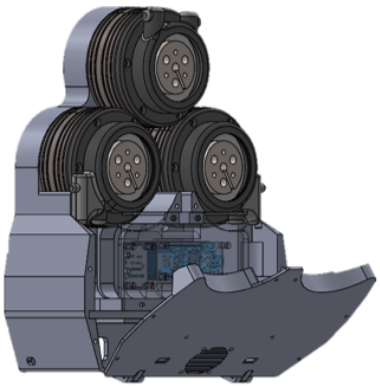

Figure 3.9 Complete actuation unit design: integration of motors, pulley-driven force sensors, control electronics, and space for battery within a compact posterior-mounted configuration.

3.5 Control System

The control system implements coordinated shoulder-elbow assistance through two synchronized control loops operating in parallel. The architecture builds upon the intent-based control framework established in Section 2.3.4, extending established single-joint biomechanical modeling methodologies to address new challenges of coordinated multi-joint assistance across coupled shoulder-elbow kinematics. Real-time implementation in Simulink operates at 100 Hz to ensure responsive assistance synchronized with user movement intentions.

3.5.1 Control Architecture and Real-Time Implementation

The control system requires accurate estimation of gravitational torques across coordinated shoulder and elbow movements to provide appropriate assistance. This section presents the kinematic parametrization and reference torque computation strategies that enable real-time gravity compensation.

Kinematic Parametrization

The upper limb is modeled as a kinematic chain of rigid bodies connected by joints. The shoulder joint is simplified to a 3-DoFspherical joint, while the wrist is assumed rigidly attached to the forearm. A fixed XYZ Euler angle parametrization describes joint orientation, where the rotation matrix from upper-arm frame u to world frame w is:

$$
{}^{w}\mathbf{R}_{u} = \begin{bmatrix} c(\phi_3)c(\phi_2) & c(\phi_3)s(\phi_2)s(\phi_1) - s(\phi_3)c(\phi_1) & c(\phi_3)s(\phi_2)c(\phi_1) + s(\phi_3)s(\phi_1) \\ s(\phi_3)c(\phi_2) & s(\phi_3)s(\phi_2)s(\phi_1) + c(\phi_3)c(\phi_1) & s(\phi_3)s(\phi_2)c(\phi_1) - c(\phi_3)s(\phi_1) \\ -s(\phi_2) & c(\phi_2)s(\phi_1) & c(\phi_2)c(\phi_1) \end{bmatrix} \tag{3.38}
$$

where $c(\cdot) = \cos(\cdot)$ and $s(\cdot) = \sin(\cdot)$.

The exosuit provides 2-DoF assistance to the shoulder, requiring a mapping from Euler angles to actuated coordinates. Following the FALCO framework, two anatomically relevant coordinates are defined:

- Shoulder elevation angle $\alpha \in [0, \pi]$: angle between the absolute z-axis and the upper arm z-axis, derived as:

$$
\alpha = \arccos(c(\phi_2)c(\phi_1)) \tag{3.39}
$$

- Arm longitude angle $\beta \in [-\pi/2, \pi/2]$: angle locating the highest point of a transversal circumference centered on the upper arm frame origin, expressed as:

$$\beta = \arctan\left(-\frac{s(\phi_2)}{c(\phi_2)s(\phi_1)}\right) \tag{3.40}$$

The elbow flexion angle θ represents the angle between the absolute z-axis and the forearm z-axis, completing the parametrization required for multi-joint gravity compensation.

The z-coordinates of the center of mass for each arm segment in the world frame are:

$$z_u = -l_{Gu}\cos(\phi_2)\cos(\phi_1) \tag{3.41}$$

$$z_l = -l_{Gl}\cos(\phi_2)\cos(\phi_1+\theta) - l_u\cos(\phi_2)\cos(\phi_1) \tag{3.42}$$

where l_{Gu} is the distance from shoulder to upper arm center of mass, l_{Gl} is the distance from elbow to forearm center of mass, and l_u is the upper arm length.

Gravity Compensation Reference Torque

Under quasi-static conditions where joint velocities and accelerations are low, the equations of motion reduce to:

$$\tau(q) \approx G(q) = \frac{\partial U}{\partial q} \tag{3.43}$$

where U represents the potential energy of the kinematic chain. The gravitational potential energy is:

$$U = m_u g z_u + m_l g z_l = -g\cos(\phi_2)\left\{\cos(\phi_1)\left[(m_u l_{Gu} + m_l l_u) + m_l l_{Gl}\cos(\theta)\right] - \sin(\phi_1)\left[m_l l_{Gl}\sin(\theta)\right]\right\} \tag{3.44}$$

Substituting $K_{ul} = m_u l_{Gu} + m_l l_u$ and $K_l = m_l l_{Gl}$, and expressing in terms of actuated coordinates (α, β, θ):

$$U = -g\left\{\cos(\alpha)\left[K_{ul} + K_l\cos(\theta)\right] - \sin(\alpha)\cos(\beta)\left[K_l\sin(\theta)\right]\right\} \tag{3.45}$$

The shoulder reference torque for gravity compensation is:

$$\tau_r = \frac{\partial U}{\partial \alpha} = g\left\{\sin(\alpha)\left[K_{ul} + K_l\cos(\theta)\right] + \cos(\alpha)\cos(\beta)\left[K_l\sin(\theta)\right]\right\} \tag{3.46}$$

To account for biological joint damping not captured in the quasi-static formulation, empirically determined damping terms are added:

$$\tau_r = g\left\{\sin(\alpha)\left[K_{ul} + K_l\cos(\theta)\right] + \cos(\alpha)\cos(\beta)\left[K_l\sin(\theta)\right]\right\} + D_1\dot{\alpha} + D_2\dot{\theta} \tag{3.47}$$

where D_1 and D_2 are positive damping coefficients empirically tuned during experimental validation.

For the elbow subsystem, the Dynamic Arm Module approach provides anthropometrically customized reference torque computation, accounting for shoulder joint configuration effects on forearm dynamics. The complete multi-joint model thus generates coordinated reference torques $\tau_{r,shoulder}$ and $\tau_{r,elbow}$ that adapt to real-time joint configurations measured by the IMU sensor network.

Inverse Kinematics: Cable Tension Calculation

The tensioning control requires mapping from desired assistive torque to required cable tension. For the shoulder subsystem, the cable displacement k as a function of elevation angle follows from the law of cosines:

$$k(\alpha) = \sqrt{k_1^{*2} + k_2^{*2} + 2k_1^* k_2^* \cos(\gamma^* + \beta^* + \alpha)} \tag{3.48}$$

where k_1^*, k_2^*, γ^*, and β^* are geometric parameters fixed by the cantilever and slider configuration. The Jacobian relating cable displacement to elevation angle is:

$$J(\alpha) = \frac{\partial k}{\partial \alpha} = -\frac{k_1^* k_2^* \sin(\gamma^* + \beta^* + \alpha)}{\sqrt{k_1^{*2} + k_2^{*2} + 2k_1^* k_2^* \cos(\gamma^* + \beta^* + \alpha)}} \tag{3.49}$$

The estimated assistive torque delivered at the shoulder virtual joint is:

$$\tau_i = J(\alpha) f \tag{3.50}$$

where f is the cable tension measured by the load cell. Similar geometric relationships govern the elbow subsystem, accounting for variable transmission geometry as shoulder configuration changes.

Motor-Proximal Sensing Architecture

The implementation of coordinated shoulder-elbow assistance in cable-driven systems presents fundamental sensing challenges. Traditional anchor-point force sensing configurations position load cells directly at the cable-limb interface, where sensors physically constrain the operational workspace. Multi-joint coordination requires extended range of motion across complex three-dimensional movements, creating mechanical interference between distributed anchor points that limits functional workspace coverage during activities of daily living.

The motor-proximal sensing architecture addresses these limitations through strategic sensor repositioning. Load cells positioned adjacent to the actuation unit measure cable forces at the motor-proximal pulley interface, eliminating physical constraints at distributed anchor points on the limb segments. This configuration enables preserved range of motion while maintaining measurement accuracy necessary for real-time force control across coordinated multi-joint movements.

The mini pulley is mounted directly on the load cell body, with the cable routing through the pulley and extending through Bowden conduits to the anchor points on the limb segments. In an ideal cable system with negligible bending stiffness, the cable tension remains approximately uniform along its length. The load cell measures the resultant force from the cable entering and exiting the pulley. For a cable under uniform tension T routing through the pulley, the force equilibrium yields:

$$F_{pulley} = 2T \tag{3.51}$$

where the factor of 2 accounts for both cable segments (entering and exiting) contributing to the measured force. The effective cable tension transmitted to the anchor point is thus:

$$T = \frac{F_{pulley}}{2} \tag{3.52}$$

This relationship assumes ideal cable behavior with uniform tension throughout the routing path. Transmission losses due to Bowden conduit friction and cable routing are accounted for separately through the transmission efficiency factor $\eta_{trans} = 0.88$ established in Section 3.3.1.

Figure 3.10 illustrates the geometric configuration of the cable-driven assistance system for both shoulder and elbow subsystems. The complex cable routing geometry, including the cantilever mechanism for shoulder assistance and the distributed anchor points for elbow support, requires configuration-dependent geometric relationships to translate measured cable tensions into appropriate assistive torques. These geometric relationships are incorporated into the real-time control system through the Jacobian-based formulation presented in Section 3.5.1, which continuously computes assistive torques accounting for joint configuration variations throughout coordinated shoulder-elbow movements.

The motor-proximal sensing architecture successfully enables coordinated multi-joint assistance by resolving the fundamental trade-off between measurement accuracy and operational range of motion inherent in cable-driven soft systems. Experimental validation presented in Chapter 4 demonstrates that this approach maintains accurate force control across

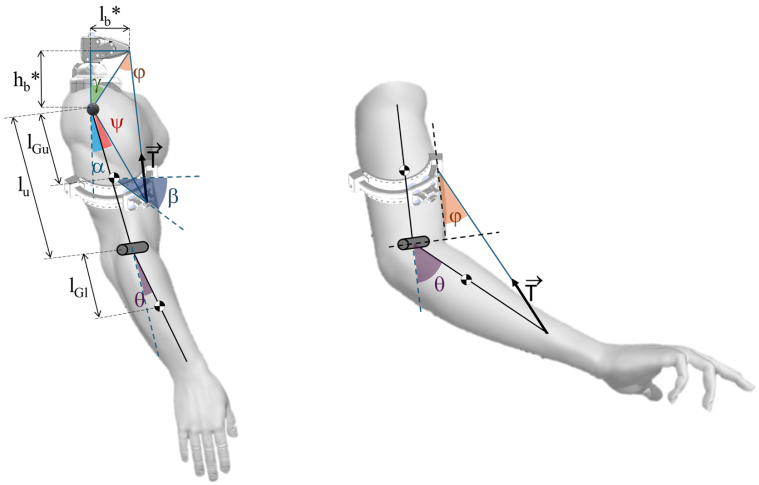

Figure 3.10 Geometric configuration of the cable-driven assistance system showing (a) shoulder assistance with cantilever mechanism and dual-tendon routing strategy, and (b) elbow assistance with cable routing from shoulder anchor to forearm attachment point. The motor-proximal load cell configuration measures cable tensions while preserving extended range of motion at distributed anchor points.

the extended workspace required for functional activities of daily living while preserving kinematic transparency essential for natural movement patterns.

Real-Time Control Implementation

The validated motor-proximal sensing architecture integrates with biomechanical modeling to enable coordinated multi-joint control through two synchronized subsystems implemented in Simulink.

The shoulder control architecture implements two parallel control loops: Tensioning Control Loop and Translating Control Loop.

• Tensioning Control Loop - The tensioning control comprises a high-level gravity compensation controller and a low-level admittance controller. The high-level controller computes reference torque τ_r from Equation 3.47 based on real-time joint angles (α, β, θ) from IMU measurements and user-specific anthropometric parameters (K_{ul}, K_l).

The interaction torque τ_i is estimated from motor-proximal load cell measurements using Equations 3.50 and 3.52, with geometric compensation continuously updating cable-limb interaction angle φ throughout coordinated movements.

The low-level admittance controller tracks the torque error $\Delta\tau = \tau_r - \tau_i$ and translates it into motor velocity commands. In the Laplace domain, the admittance relationship is:

$$\frac{\dot{x}(s)}{\tau(s)} = R(s) = B_a + \frac{D_a}{s} + M_a s \tag{3.53}$$

where B_a, D_a, and M_a are proportional, integral, and derivative gains respectively, empirically tuned during experimental validation to achieve stable, responsive assistance.

• Translating Control Loop - The translating control continuously reconfigures anchor geometry to maintain optimal force vector orientation throughout coordinated movements. An adaptive fading filter smooths longitude angle β measurements to manage singularity conditions near zero elevation:

$$y[n] = (1-\lambda)x[n] + \lambda y[n-1] \tag{3.54}$$

where the fading factor λ varies between λ_{min} and λ_{max} based on elevation angle α through a sigmoid function:

$$\lambda(\alpha) = \left(1 - \frac{1}{1+e^{k(\alpha-\alpha_0)}}\right)\lambda_{max} + \frac{1}{1+e^{k(\alpha-\alpha_0)}}\lambda_{min} \tag{3.55}$$

where α_0 is the interpolation midpoint and k regulates curve steepness. The filtered β signal drives a PID position controller with Ziegler-Nichols tuned parameters to actuate the cart position on the cantilever rail.

The elbow control subsystem extends the Dynamic Arm Module methodology to the new context of coordinated shoulder-elbow assistance, providing anthropometrically customized assistance adapted to shoulder joint configuration. The biomechanical model computes reference torque accounting for forearm gravitational effects and shoulder-dependent transmission geometry. Motor-proximal load cell measurements, corrected through geometric compensation specific to the elbow cable routing, provide interaction torque feedback. An admittance controller identical in structure to Equation 3.53 generates motor velocity commands, with independently tuned parameters optimized for elbow dynamics.

Sensor Fusion and Communication Architecture

IMU sensors positioned on the upper arm and forearm provide three-dimensional orientation data processed through quaternion representation to determine coordinated shoulder-elbow movements and extract joint angles (α, β, θ). These angles drive both reference torque computation and geometric compensation for motor-proximal force measurements.

The communication architecture implements a proprietary BLE UART protocol ensuring reliable data transmission at 100 Hz operational frequency. Motor-proximal load cells continuously measure pulley forces, which are converted to effective cable tensions through real-time geometric compensation. The admittance controllers calculate optimal motor speed commands by analyzing the differential between measured interaction torque and biomechanically computed reference torque for simultaneous shoulder and elbow assistance.

The coordinated multi-joint control architecture is illustrated in Fig. 3.11 through a CAD representation showing the physical implementation of the three parallel control loops: elbow assistance control (tensioning), shoulder tensioning control, and shoulder translating control. Each subsystem actuates independently while sharing common sensory information from the IMU sensors.

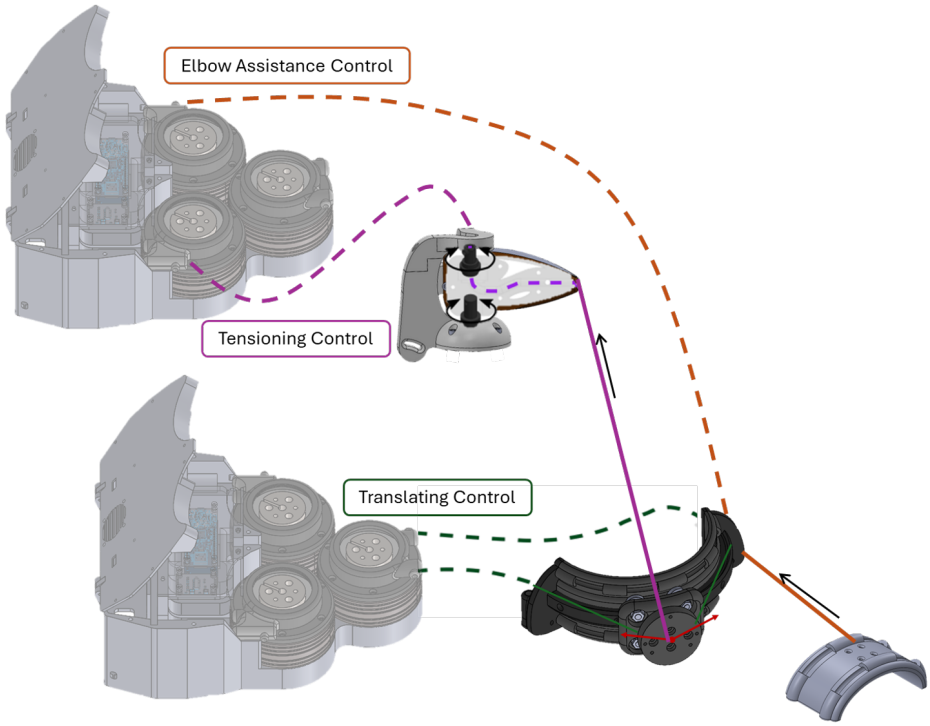

Figure 3.11 CAD representation of the coordinated multi-joint control architecture showing the three parallel control loops: elbow assistance control, shoulder tensioning control, and shoulder translating control. Each subsystem operates independently while sharing sensory information from the IMU sensors.

Fig. 3.12 presents the detailed control flow diagram, highlighting the sensor fusion layer where IMU data is processed for 3D kinematics computation and the geometric compensation applied to load cell measurements. The shoulder control system (right, blue box) comprises two synchronized loops: the tensioning control implements gravity compensation through a

biomechanical model and admittance controller, while the translating control employs an adaptive fading filter and PID position controller to maintain optimal anchor geometry. The elbow control system (left, red box) mirrors the tensioning architecture with independently tuned parameters. Both subsystems receive shared joint angle measurements (α, β, θ) from the sensor fusion layer while relying on dedicated load cells for interaction force feedback, enabling coordinated assistance across shoulder flexion/extension, abduction/adduction, and elbow flexion/extension degrees of freedom.

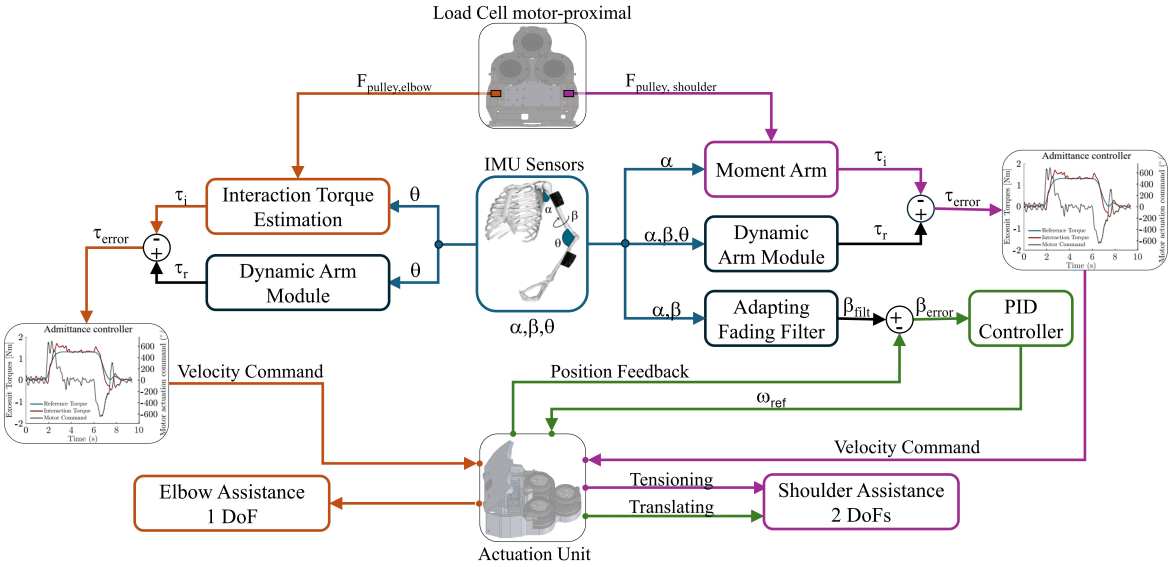

Figure 3.12 Control flow diagram. The shoulder tensioning loop (magenta) combines feedforward gravity compensation (reference torque τ_r from biomechanical model, Eq. 3.47) with feedback admittance control (interaction torque τ_i from motor-proximal load cells via geometric compensation, Eq. 3.50). The translating loop (green) tracks longitude angle β via PID. The elbow loop (orange) implements independent admittance control with geometric compensation of motor-proximal force measurements. All subsystems share joint angle estimates (α, β, θ) from IMU sensors, where ω_{ref} denotes the motor velocity command for the translating actuator.

Figure 3.13 illustrates the complete control system implementation in Simulink, showing the main coordination system and detailed shoulder and elbow subsystems with their respective control loops, sensor fusion, and motor command generation pathways.

This integrated control architecture enables real-time coordinated assistance across shoulder and elbow joints, leveraging motor-proximal sensing to maintain accurate force feedback throughout extended functional movements while biomechanical modeling ensures gravity compensation adapts continuously to user configuration and movement intentions.

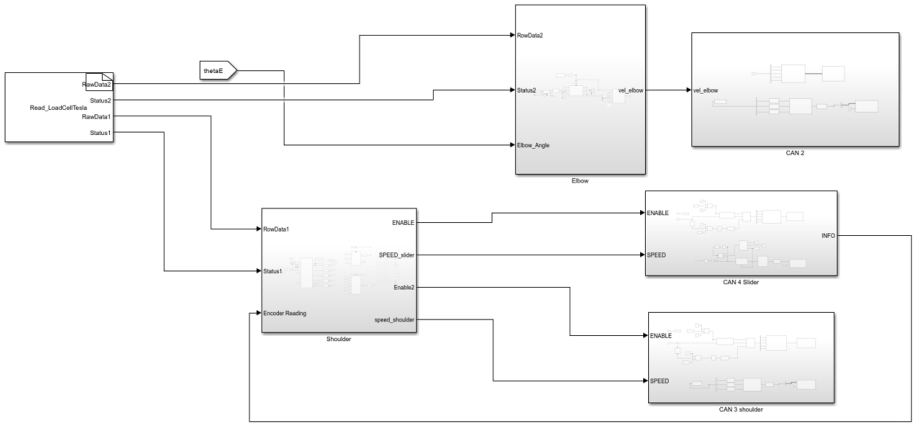

Figure 3.13 Simulink implementation of coordinated multi-joint control architecture. Main system coordinates two parallel subsystems: shoulder 2-DoF control (Figure 3.14) and elbow control (Figure 3.15).

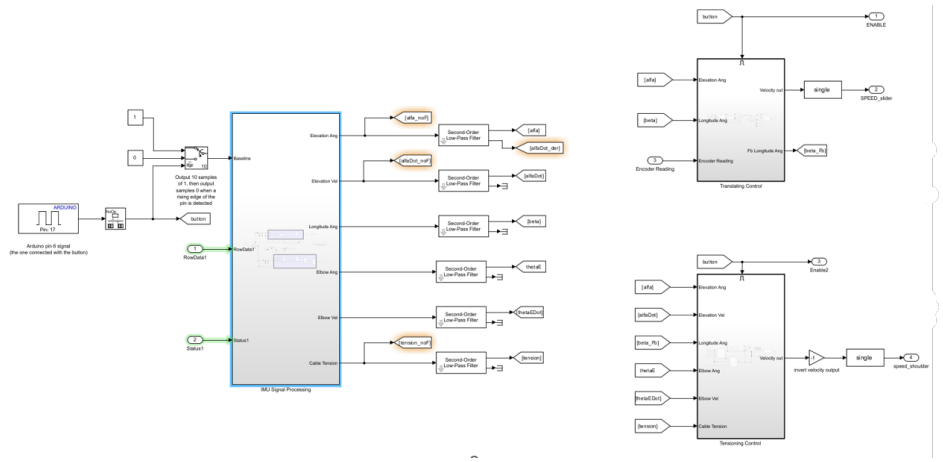

Figure 3.14 Shoulder 2-DoF control (tensioning and translating loops).

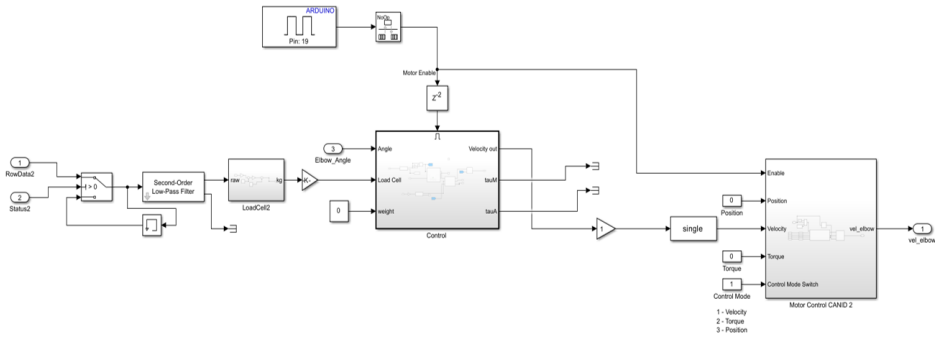

Figure 3.15 Elbow control (dynamic arm module with motor-proximal sensing).

3.6 Prototype Development

Following CAD design finalization and control system architecture specification, prototype development translates digital models into physical hardware through additive manufacturing, component procurement, and systematic assembly. This section documents manufacturing approaches, complete hardware specifications, and integration procedures validating mechanical and electrical system functionality prior to human subject testing.

3.6.1 Manufacturing and Components

The prototype leverages Fused Deposition Modeling (FDM) 3D printing for custom mechanical components, enabling rapid design iteration and geometric customization. All structural and interface components are fabricated primarily in Polylactic Acid (PLA) thermoplastic material with layer height 0.2 mm, infill density 40% gyroid pattern for optimal strength-to-weight ratio, and wall thickness 3-5 mm depending on structural requirements.

3D-printed components undergo manual support removal, light sanding of mating surfaces, and installation of heat-set brass threaded inserts (M2, M3, M4 threads) for improved assembly robustness. Sealed ball bearings (specification: 8 mm inner diameter, 22 mm outer diameter, 7 mm width) are press-fitted into pulley and slider components. Shoulder and elbow bracelets employ polyurethane cuffs with integrated 12 mm polyurethane foam padding to distribute interface forces and reduce peak pressures during extended wear. The cuffs are secured using Boa® dial-actuated closure systems providing tool-free, customizable adjustment. The shoulder cuff accommodates arm circumferences from 220 mm to 420 mm, while the elbow cuff accommodates forearm circumferences from 180 mm to 280 mm, corresponding to 5th-95th percentile adult anthropometry.

High-tensile Kevlar cables (1.0 mm diameter, 150 N breaking strength) are precision-cut and terminated using aluminum crimp ferrules compressed with crimping tool to ensure secure mechanical connection. Redundant locking set screws provide secondary retention preventing cable slippage under dynamic loading conditions. PTFE-lined Bowden conduits (5.0 mm outer diameter, 1.6 mm inner diameter) are heat-formed to required routing geometry, enabling custom cable paths while maintaining low-friction transmission characteristics. Conduits are secured to structural components with cable ties to prevent unwanted motion during operation. Cables are pre-tensioned to 5-8 N to eliminate slack and improve control response, ensuring immediate force transmission while avoiding excessive preload that could induce unwanted assistive torques at rest configuration.

Hardware Components and Bill of Materials

Table 3.5 presents the complete Bill of Materials (BOM) for the functional prototype, categorizing components by subsystem with quantities and procurement sources.

Table 3.5 Complete Bill of Materials (BOM) for functional prototype.

Component	**Specification/Part Number**	**Qty**	**Source**
Actuation Subsystem			
Brushless DC Motor	AK60-6, 3.0 Nm nominal, 6:1 reduction	3	T-Motor, China
Motor Pulley (40mm)	3D-printed PLA, 608ZZ bearings, cable winding	3	Custom
Mini Pulley (load cell)	3D-printed PLA, cable redirection for force sensing	2	Custom
Sensing Subsystem			
Load Cell	DYMH 103, 20 kg (196 N) capacity	2	Generic, China
Load Cell Amplifier	CJMCU-711 HX711 24-bit dual channel	2	Generic, China
IMU	BMI085 Shuttle Board 3.0, 6-axis	2	Bosch Sensortec
Bluetooth Module	Feather nRF52840, BLE UART	2	Adafruit #4062
Control Electronics			
Microcontroller	Arduino MKR WiFi 1010, ARM Cortex-M0+ 48MHz	1	Arduino, Italy
Shield/Interface	Arduino Proto Shield	1	Arduino, Italy
Battery	LiPo 14.8V (4S) 3700mAh	1	Generic
Wiring Harness	AWG22-26, Bowden routing, Boa® cable mgmt	1	Custom
Mechanical Structure (3D-printed)			
Actuation Housing	PLA, 40% infill, motor mounts	1	Custom
Cantilever Mechanism	PLA with reinforcement support	1	Custom
Dual-Pulley Slider	PLA, bearings, bidirectional carriage	1	Custom
Shoulder Bracelet Base	PLA, circumferential rail, slider guide	1	Custom
Elbow Bracelet Base	PLA, anchor point connector	1	Custom
Wearable Interface			
Back Support Harness	Commercial, adjustable, padded, lumbar belt	1	Commercial
Shoulder Cuff	Polyurethane, foam 12mm, Boa® closure	1	Custom
Elbow Cuff	Polyurethane, foam 12mm, Boa® closure	1	Custom
Cable System			
Kevlar Cable	1.0mm diameter, 150N strength	$\sim$4 m	Generic
Bowden Conduit	PTFE-lined, 5.0mm OD, 1.6mm ID	$\sim$5 m	Shimano
Ferrules/Terminations	Aluminum 4mm, locking set screws	12	Generic
Ball Bearings	608ZZ sealed, 8×22×7mm	6	Generic
Heat-Set Inserts	Brass M3, M4	50	Generic

Key Component Descriptions:

- Motor Pulleys (40mm): Custom 3D-printed pulleys mounted on AK60-6 motor shafts for cable winding, providing primary actuation for shoulder flexion/extension, abduction/adduction, and elbow flexion/extension
- Mini Pulleys (load cells): Small cable redirection pulleys positioned adjacent to motor-proximal load cells (DYMH 103), enabling force measurement by routing cable tension through the pulley-load cell assembly
- Back Support Harness: Commercial adjustable harness with padded straps and lumbar belt, providing posterior mounting platform for centralized actuation unit at T6-T8 vertebral level
- Boa® Closure System: Dial-actuated cable tightening mechanism integrated into shoulder and elbow cuffs for tool-free adjustment. Additionally used as cable management system for shoulder abduction/adduction tendon routing

Prototype Components Overview

Figures 3.16 through 3.22 present the fabricated individual components prior to final assembly, illustrating the integration of commercial electronics, 3D-printed mechanical structures, and custom wearable interfaces.

Figure 3.16 Mounting shoulder and cable director with cantilever mechanism.

Figure 3.17 Elbow anchor point with cable termination.

Figure 3.18 Shoulder slider guide and anchor point assembly demonstrating circumferential rail and bidirectional carriage.

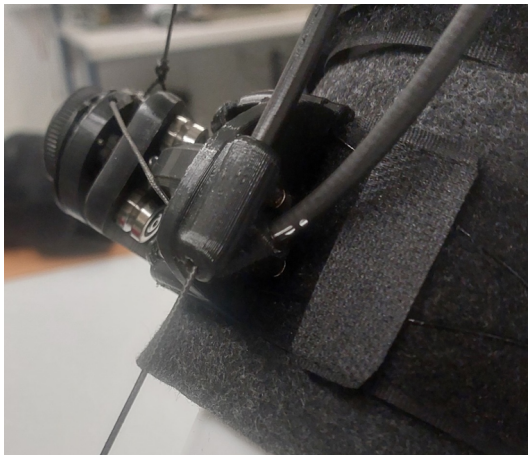

Figure 3.19 Elbow cable connector for intermediate routing guidance along upper arm.

Figure 3.20 IMU Bluetooth modules: BMI085 6-axis sensors with Feather nRF52840 for wireless kinematic sensing.

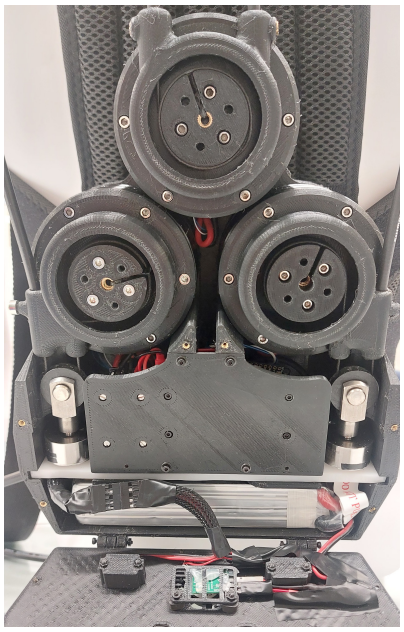

Figure 3.21 Actuation system showing three AK60-6 motors with integrated motor-proximal load cells.

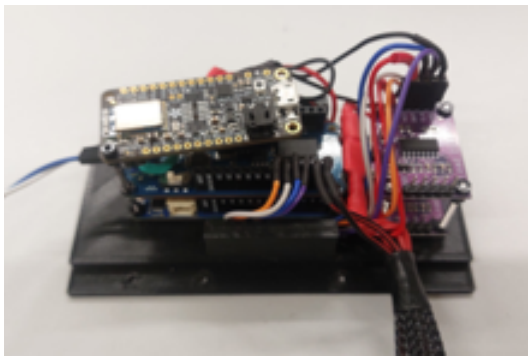

Figure 3.22 Control electronics: Arduino MKR WiFi 1010, HX711 load cell amplifiers, Feather BLE hub, and battery interface.

3.6.2 Assembly and System Integration

System assembly proceeds systematically through subsystem-level integration followed by complete system validation.

1. Actuation unit assembly:
    - Motor mounting to 3D-printed base plate;
    - Mini pulley and load cell installation in motor-proximal positions;
    - Cantilever mechanism attachment to rotary joint with reinforcement support;
    - Dual-pulley slider mechanism installation for shoulder abduction/adduction control;
    - Electronics integration: Arduino MKR WiFi, HX711 amplifiers, Feather BLE hub, battery pack;
    - Housing closure with Bowden conduit strain relief.
2. Wearable interface fabrication:
    - Polyurethane cuff preparation with Boa® closure system integration;
    - Polyurethane foam padding (12 mm thickness) bonding to inner cuff surfaces;
    - 3D-printed anchor point and slider components integration with cuff base;
    - IMU module (BMI085 + Feather nRF52840) attachment to cuff exterior with protective enclosures.
3. Cable system routing:
    - Bowden conduit heat-forming to required bend radii;
    - Kevlar cable threading through conduits with PTFE lubricant spray;
    - Ferrule termination at anchor points (cuffs) and motor pulleys using hydraulic crimping;
    - Cable pre-tensioning to 5-8 N to eliminate slack;
    - Conduit securing to harness and cuffs with guide clips and Boa® cable management.
4. Electrical interconnection:

- Load cell wiring to HX711 amplifiers, amplifier outputs to Arduino analog inputs;
- Motor CAN bus daisy-chain connection (3 motors on single bus, 120Ω termination resistors);
- IMU-Feather pairing: BMI085 → Feather BLE via I2C interface, wireless BLE UART to Arduino;
- Battery connection: 14.8V LiPo powers all subsystems (motors operate at reduced voltage for safety, Arduino uses onboard 5V/3.3V regulators);
- Power distribution verification with voltage monitoring.

5. Software upload and calibration:

   - Control algorithm upload from MATLAB/Simulink to Arduino via Arduino IDE;
   - Required libraries: HX711 (load cell interface), CAN bus (motor communication), BLE UART (IMU wireless);
   - Load cell zero-offset calibration: record baseline readings with no cable tension, store offsets in EEPROM;
   - IMU initialization: activate sensors with arm in neutral position (arm along body, 0° elevation), establish coordinate frame reference for abduction/adduction zero position;
   - Motor encoder homing: zero cable displacement at neutral arm configuration.

A detailed view of the complete system assembly is shown in Figure 3.23.

System Operation and User Interface

The assembled prototype operates through a combination of hardware controls and software configuration, enabling personalized assistance delivery and experimental data collection. The system features three physical control elements integrated into the actuation unit: a main power switch for system activation, a shoulder assistance toggle enabling or disabling shoulder flexion-extension and abduction-adduction assistance, and an elbow assistance toggle controlling elbow flexion-extension support. Both subsystem toggles can be activated simultaneously for coordinated 3-DoF assistance or independently for single-joint support during specific rehabilitation protocols. Visual feedback is provided through a power LED indicator, with active cooling via an integrated ventilation fan that activates automatically during motor operation to maintain thermal management of the actuation unit electronics.

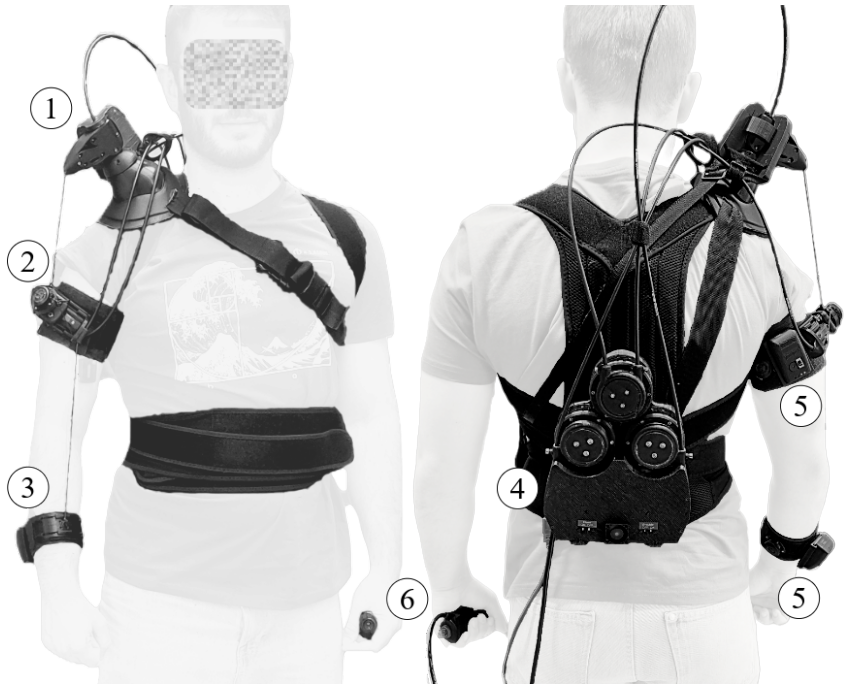

Figure 3.23 Complete system assembly: (1) Cantilever mechanism with cable director; (2) Shoulder bracelet with integrated slider guide and anchor point; (3) Elbow bracelet with anchor point and cable termination; (4) Actuation unit (posterior-mounted on harness) with three motors, load cells, and control electronics; (5) Bluetooth IMU sensors (2×BMI085 + Feather modules) mounted on bracelets; (6) Emergency stop button integrated into harness for safety-critical shutdown.

The control algorithm requires user-specific anthropometric parameters to compute appropriate gravitational compensation torques (Section 3.3.1). User body height H [mm] and mass M_{body} [kg] are entered via the MATLAB/Simulink interface on a development PC. The model automatically computes segment lengths and masses through anthropometric scaling relationships (Equations 3.24–3.25) and compiles the control algorithm with embedded user parameters. The compiled binary is uploaded to the Arduino MKR WiFi 1010 microcontroller via USB connection, enabling standalone operation with the configured parameters. These user-specific parameters remain stored in the microcontroller memory across power cycles, requiring reconfiguration only when switching to a different user or modifying assistance settings.

At system power-on, initial calibration establishes sensor reference frames. The user maintains a neutral posture with arms relaxed along the body (shoulder and elbow angles near 0° from vertical) while IMU sensors establish gravitational orientation references and load cells record zero-force baselines. This calibration procedure is automatically executed during system startup. Following calibration, the system operates in one of three states: standby

mode with motors unpowered and sensors monitoring only, calibration mode during the automated sensor zeroing at startup, or assistance mode with active gravity compensation and real-time force control at 100 Hz. Hardware assistance toggles enable immediate activation or deactivation of shoulder and elbow subsystems without requiring system restart, providing flexibility for therapeutic protocols requiring varied assistance configurations.

Safety features include a dedicated hardware emergency stop button accessible on the back support harness, which immediately cuts motor power via hardware interrupt independent of software state. Additional software-implemented protections monitor cable tensions with automatic shutdown if forces exceed 150 N and enforce joint angle limits with assistance disabled outside the 0°–90° operational range specified in PDS (Table 3.1).

When connected to a PC via USB serial interface, the microcontroller streams sensor data at 100 Hz to the Simulink environment for real-time monitoring and post-processing. Logged data include cable tensions [N], motor states (positions, velocities, currents), joint angles [deg] computed from IMU quaternions, and system status information (operational mode, battery voltage). This architecture separates data acquisition from control execution, ensuring the 100 Hz control loop performance remains unaffected by logging operations.

Complete Wearable System

The fully integrated prototype is designed for independent donning/doffing and comfortable extended wear during rehabilitation sessions. Figure 3.24 presents the complete system worn by a user, demonstrating the posterior-mounted actuation unit on the back support harness, shoulder and elbow bracelets with integrated anchor points and IMU sensors, and cable routing geometry from actuation unit through Bowden conduits to distributed anchor points on the limb segments. System Specifications:

- Total mass: 3337 g (3.34 kg), meeting portability target $<$5 kg;
- Battery runtime: $>$2 hours continuous operation at 50% duty cycle;
- Donning/doffing: It can be worn yourself, and the bracalets adjustment and cable tension are easily managed with the Boa® Fit System;
- Adjustability range: Shoulder circumference 220-420 mm, elbow circumference 180-280 mm (5th-95th percentile adult anthropometry).

The integrated prototype embodies the novel motor-proximal sensing architecture enabling coordinated 3-DoF cable-driven assistance, a capability not achievable with conventional anchor-point configurations due to the fundamental geometric constraint of spatial

(a) (b)

Figure 3.24 Complete wearable system demonstrating functional prototype worn by user during preliminary testing. Total system mass: 3337 g (3.34 kg), meeting portability requirement <5 kg specified in PDS (Table 3.1). (a) Posterior view: actuation unit mounted on adjustable back support harness at T6-T8 vertebral level, cable routing through Bowden conduits to shoulder and elbow anchor points; (b) Lateral view: shoulder bracelet with slider mechanism, elbow bracelet with anchor point, IMU sensors on limb segments, emergency stop accessible on harness.

interference during multi-joint movements. Strategic sensor repositioning from anchor points to actuation unit locations preserves the free cable length necessary for simultaneous shoulder and elbow assistance across extended functional workspace (0–90° all DoF), while maintaining force measurement accuracy through geometric compensation algorithms.

This innovation represents an enabling advancement in cable-driven soft exosuit technology, extending proven single-joint assistance paradigms to coordinated multi-joint rehabilitation applications without the mass penalties and kinematic constraints of rigid exoskeleton alternatives.

The functional prototype validates the systematic design methodology, successfully translating mathematical models (Section 3.3), CAD designs (Section 3.4), and control algorithms (Section 3.5) into physical hardware ready for human subject validation (Chapter 4).

Chapter 4

Experimental Validation

Following the design and prototype development at Heidelberg University presented in Chapter 3, experimental validation with human subjects was subsequently performed at the Technical University of Munich (TUM), also in Prof. Masia's laboratory.

4.1 Validation framework and objectives

The systematic design methodology presented in Chapter 2 was applied to develop a co-ordinated shoulder-elbow cable-driven exosuit, as documented in Chapter 3. This chapter presents the experimental validation conducted to assess system performance through two sequential phases. First, preliminary technical validation verified the motor-proximal sensing approach as an enabling solution for multi-joint coordination with preserved range of motion. Second, human subject trials quantified kinematic accuracy, muscle activation reduction, and functional task performance across standardized movement protocols. The validation framework integrates biomechanical metrics with physiological indicators to establish system effectiveness for rehabilitation applications.

4.2 Motor-proximal Sensing tests

Before proceeding to full system prototyping, the motor-proximal sensing approach required experimental validation to confirm that geometric compensation algorithms could maintain control accuracy across the extended ROM necessary for functional multi-joint coordination. The validation objective was to verify that force measurements obtained from motor-proximal load cells, after geometric compensation, would produce effective cable tension estimates

comparable to conventional anchor-point measurements while enabling increased functional range of motion.

4.2.1 Experimental setup and Results

A preliminary prototyping phase evaluated two sensing configurations: conventional anchor-point load cell placement directly at the cable-limb interface (highlighted configuration in Figure 4.1a), and motor-proximal load cell placement adjacent to the actuation unit (Figure 4.1b). The goal of relocating the load cell from the anchor point was to eliminate mechanical interference constraints that limit functional ROM in multi-joint coordination, particularly during combined shoulder-elbow movements.

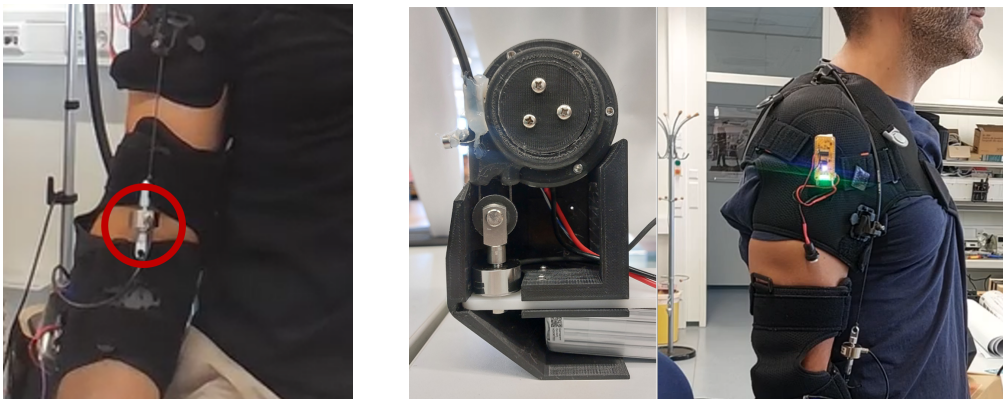

(a) (b)

Figure 4.1 Preliminary validation configurations comparing anchor-point and motor-proximal load cell placement. (a) Anchor-point load cell configuration (conventional approach with ROM limitations highlighted); (b) Subject wearing system with motor-proximal configuration during validation trials.

The motor-proximal configuration integrated load cells within the actuation unit alongside brushless motors and control electronics (Figure 4.2). This architecture enables unobstructed movement across the full functional workspace required for coordinated shoulder-elbow assistance.

Subjects performed repetitive shoulder-elbow coordination movements spanning the functional workspace while the system simultaneously recorded force measurements from both sensing configurations. The load cell positioned at the anchor point measured cable tension directly at the user interface, while the motor-proximal load cell measured pulley forces that were converted to effective cable tension through the geometric compensation algorithm.

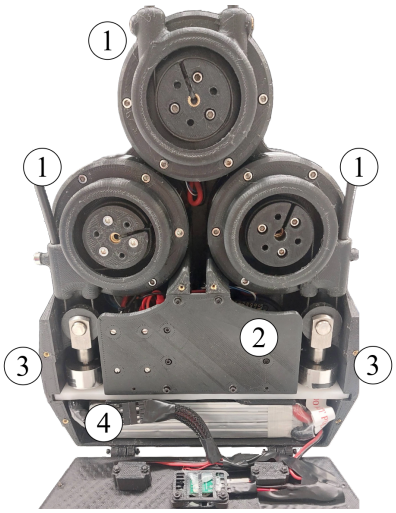

Figure 4.2 Actuation unit with integrated motor-proximal load cells. Internal configuration shows brushless motors (1), dual microcontroller system (2), strategically repositioned load cells (3), and integrated power management (battery pack 14.8V, 3700 mAh) (4).

Figure 4.3 presents the comparative time-series data for cable tension measurements across multiple movement cycles. The blue trace represents direct anchor-point measurements, while the orange trace shows motor-proximal measurements after geometric compensation. The two signals demonstrate close agreement throughout the movement sequence, with both capturing the same fundamental load patterns during assisted lowering and lifting movements.

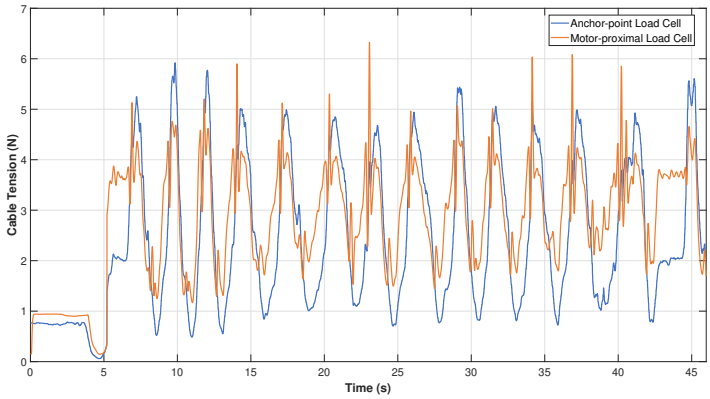

Figure 4.3 Preliminary qualitative validation comparing anchor-point load cell (blue) versus motor-proximal load cell with geometric compensation (orange) during repetitive shoulder-elbow coordination movements. Consistent tracking patterns confirm feasibility of motor-proximal approach. Comprehensive quantitative validation is presented in Section 4.4.2.

This preliminary assessment confirmed technical feasibility of motor-proximal sensing for coordinated multi-joint assistance. The observed tracking consistency between sensor configurations provided sufficient foundation to proceed with integrated prototype development and comprehensive validation. Detailed quantitative assessment with statistical validation across the operational workspace is presented in Section 4.4.2.

The motor-proximal sensing configuration eliminates mechanical constraints at distributed anchor points while requiring geometric compensation to maintain measurement accuracy, enabling coordinated assistance across extended workspace necessary for functional rehabilitation movements.

Range of Motion Preservation Through Free Cable Length Optimization

The motor-proximal sensing architecture addresses a fundamental geometric constraint in coordinated multi-joint cable-driven assistance. In cable-driven systems, the achievable range of motion depends critically on the available free cable length—the cable segment extending from the cable exit point (where the cable emerges from the Bowden conduit) to the anchor point on the limb segment. Anchor-point load cell configurations position the force sensor between the cable and the anchor attachment, effectively reducing the available free cable length by the physical dimensions of the load cell housing (typically 40-50 mm for miniature S-type sensors). This reduction constrains the maximum achievable joint excursion.

Single-joint cable-driven systems (such as FALCO for shoulder assistance or Lotti et al. for elbow assistance) can optimize cable routing geometry and exit point positioning to achieve full 0-90° functional range despite this constraint, as the single cable path can be designed specifically for one joint's kinematic requirements. However, coordinated multi-joint assistance introduces a critical design conflict: the cable exit point and routing geometry must simultaneously accommodate multiple joints with coupled kinematics, where optimal positioning for one joint may compromise the other.

This geometric coupling creates three competing design scenarios for coordinated shoulder-elbow assistance: (1) positioning the elbow cable exit point near the shoulder anchor location reduces available free cable for elbow assistance, limiting elbow range of motion below the required 90°; (2) relocating the shoulder anchor point upward to accommodate elbow cable routing reduces shoulder free cable length, constraining shoulder elevation; (3) optimizing anchor positions to achieve 90° range for both joints independently creates spatial interference between the two free cable segments during coordinated movements, where the physical cables mechanically collide during combined shoulder elevation and elbow flexion.

The motor-proximal sensing configuration resolves this fundamental conflict by eliminating the load cell from the free cable segment. Relocating force sensors to the actuation unit

preserves the complete available cable length for kinematic function, enabling optimization of cable exit points and routing geometry to simultaneously achieve 0-90° range across all three degrees of freedom (shoulder flexion/extension, shoulder abduction/adduction, elbow flexion/extension) while eliminating spatial interference between free cable segments during coordinated movements. This innovation enables a novel exosuit architecture: coordinated multi-joint cable-driven assistance with preserved functional workspace becomes feasible through the strategic sensor repositioning, representing a fundamental advancement rather than incremental improvement over existing single-joint cable-driven systems.

Preliminary validation confirmed this capability, with force measurement comparison (Figure 4.3) demonstrating that measurement accuracy is maintained throughout the extended workspace. The motor-proximal approach thus enables the coordinated assistance paradigm validated in this work, addressing a constraint that would otherwise fundamentally limit cable-driven multi-joint systems to either reduced range of motion or single-joint operation.

4.3 Experimental Methods

4.3.1 Experimental Design and Data Analysis

The validation study employed a within-subjects repeated-measures design to systematically evaluate exosuit performance across standardized upper limb movement tasks. Data acquisition was implemented through a dual-pathway system: kinematic data collection via serial communication from the control unit to a dedicated DAQ board operating at 100 Hz sampling frequency, and physiological monitoring through wireless surface electromyography. Figure 4.4 illustrates the complete data acquisition infrastructure deployed during experimental trials.

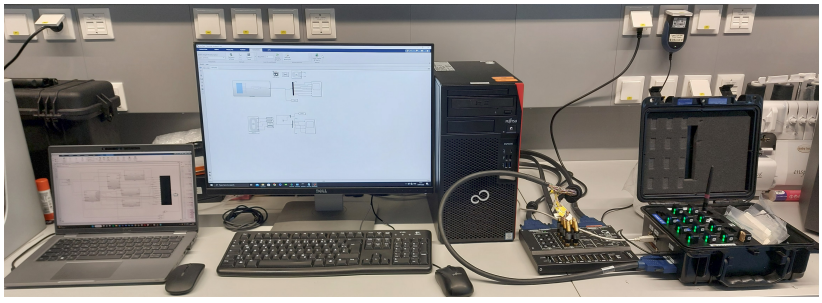

Figure 4.4 Data acquisition setup with dual-pathway architecture: kinematic processing station and wireless EMG system, providing real-time signal visualization during trials.

Surface EMG data were acquired using a wireless Delsys system targeting three key muscles: biceps brachii (elbow flexion assistance evaluation), anterior deltoid (shoulder flexion assistance assessment), and medial deltoid (shoulder abduction assistance analysis). Electrode placement followed standardized SENIAM guidelines with strategic positioning to avoid mechanical interference with exosuit components while maintaining optimal signal acquisition geometry (Figure 4.5). Temporal synchronization between exosuit kinematic data and electromyographic recordings was performed during offline processing through cross-correlation of movement onset markers embedded in both data streams.

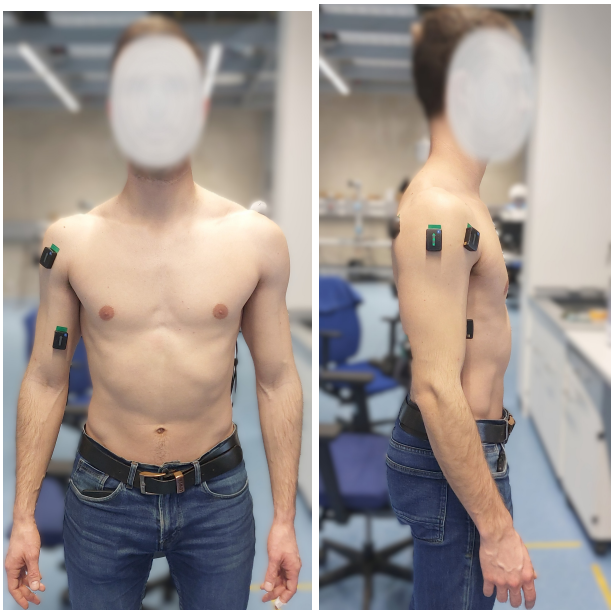

(a) (b)

Figure 4.5 EMG electrode placement following SENIAM guidelines: (a) biceps brachii and anterior deltoid positioning; (b) medial deltoid placement optimized to avoid interference with cable routing during multi-joint movements.

This preliminary validation study recruited five healthy male participants (age 29 ± 5 years, height 1.8 ± 0.1 m, body weight 73 ± 9 kg) through convenience sampling. The homogeneous demographic profile was intentionally selected to minimize anthropometric confounding variables during proof-of-concept validation while establishing baseline system performance characteristics.

Participants met the following inclusion criteria: anthropometric measurements compatible with exoskeleton design parameters (height 1.65–1.95 m, body mass 60–90 kg), normal joint range of motion across all upper limb articulations, sufficient muscle strength to complete the testing protocol without assistance, and absence of neurological, musculoskeletal, or

cardiovascular conditions that could influence movement patterns or physiological responses. Exclusion criteria included any history of shoulder or elbow injury within the previous 12 months, chronic pain conditions affecting the upper limbs, or inability to provide informed consent.

All experimental procedures were conducted in accordance with the ethical principles outlined in the Declaration of Helsinki for medical research involving human subjects. Prior to participation, all volunteers received comprehensive information regarding study procedures, potential risks (muscle fatigue, minor skin irritation from equipment contact), and the voluntary nature of participation. Written informed consent was obtained from all participants, who were informed of their right to withdraw from the study at any time without penalty. To minimize risks of skin irritation, all equipment contacting participants (bracelets, EMG sensors) was thoroughly disinfected between users using standard sterilization protocols. The experimental protocol included scheduled rest periods and participants were encouraged to request additional breaks as needed to prevent excessive fatigue.

Reference trajectories for controlled range of motion tasks were generated as sinusoidal profiles with 90° amplitude to match the functional range requirements specified in the Product Design Specification. A standardized movement frequency of approximately 0.2 Hz (5-second cycle period, corresponding to 2.5 seconds per ascending and descending phase) was imposed across all participants to enable controlled inter-subject comparison and minimize variability attributable to different movement cadences. This relatively slow cadence was selected to ensure smooth, controlled movements suitable for evaluating gravity compensation effectiveness while avoiding dynamic effects that could confound muscle activation measurements and preventing premature fatigue accumulation during the extended multi-task protocol. The standardization was particularly appropriate for the healthy participant cohort, where uniform pacing facilitates systematic evaluation of exosuit assistance effectiveness without confounding factors introduced by individual movement preferences. The sinusoidal profile provided smooth, continuous motion patterns suitable for evaluating system tracking performance and coordination maintenance across the full operational workspace.

Task protocol and experimental conditions

Participants completed all tasks under two randomized conditions: Exo On (full exosuit assistance with active gravity compensation) and No Exo (sensor-only configuration with IMUs worn, no mechanical assistance).

The experimental protocol included both standardized movement assessments and functional tasks representative of activities of daily living. Controlled range of motion tasks consisted of three primary movements performed at 90° amplitude with 5 repetitions per

3 series each (Figure 4.6): elbow flexion-extension evaluating single-joint assistance effectiveness, shoulder flexion-extension assessing sagittal plane coordination, and shoulder abduction-adduction quantifying frontal plane assistance capabilities.

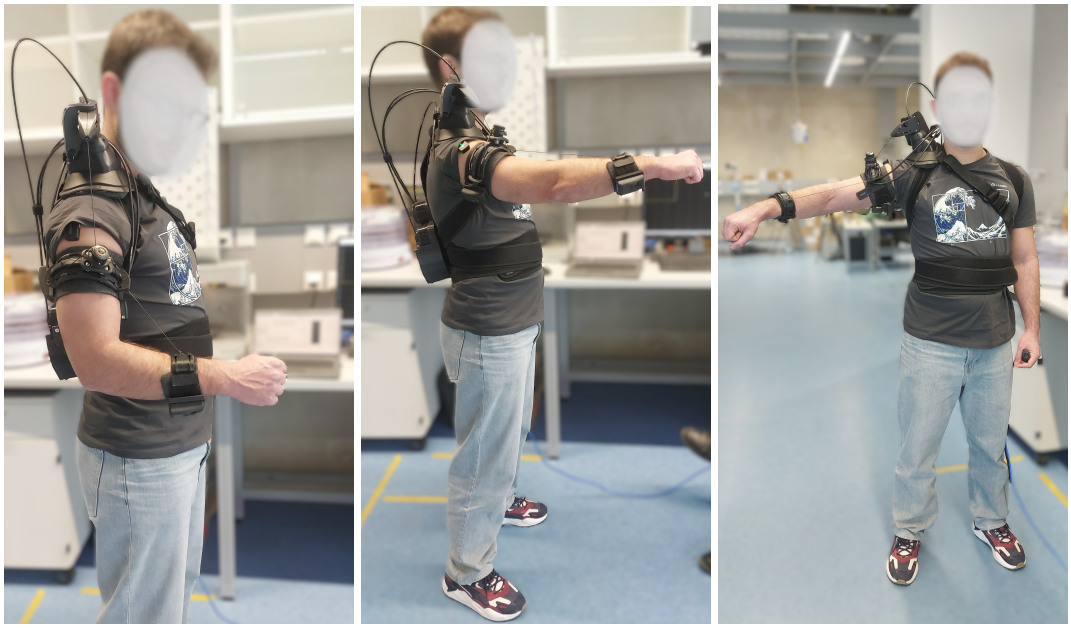

(a) (b) (c)

Figure 4.6 Controlled range of motion tasks: (a) elbow flexion–extension; (b) shoulder flexion–extension in the sagittal plane; (c) shoulder abduction–adduction in the frontal plane. All tasks were performed with a standardized 90° amplitude and fixed repetition structure to enable systematic comparison across assistance conditions.

Functional tasks included drinking task demonstrating complex multi-joint coordination through four sequential phases: initial reach toward target object, precision grasping, coordinated lifting and drinking motion, and controlled return to rest position (Figure 4.7). Additional functional evaluation employed pick-and-place tasks performed on a standardized pegboard apparatus. The pegboard setup was positioned on a 90 cm-high table. The lowest peg was located 50 cm above the table surface, with subsequent pegs placed at 7 cm vertical intervals. This arrangement ensured that each participant interacted with the pegboard at approximately shoulder height when the arm was elevated to 90°, matching the intended horizontal arm posture. Participants were positioned 55 cm horizontally from the pegboard frame. Each peg measured 10 cm in length, providing a consistent task across the workspace. Pick-and-place tasks were executed at two standardized orientations: frontal manipulation at 0° azimuth and lateral manipulation at 45° azimuth, both at 90° elevation, with identical repetition structure to controlled ROM tasks (Figure 4.8).

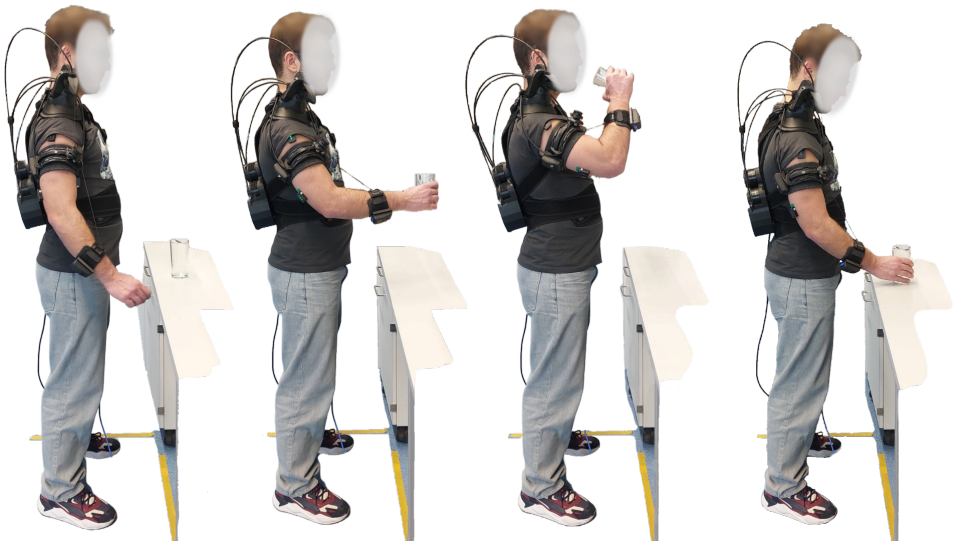

(a) (b) (c) (d)

Figure 4.7 Functional drinking task sequence demonstrating complex multi-joint coordination: (a) initial reach toward target object, (b) precision grasping phase, (c) coordinated lifting and drinking motion, (d) controlled return to rest position.

(a) (b)

Figure 4.8 Functional pick-and-place tasks on standardized pegboard: (a) frontal manipulation (0° azimuth, 90° elevation) requiring coordinated shoulder–elbow motion; (b) lateral manipulation (45° azimuth) assessing extended-range multi-joint coordination.

Each participant completed a single 2-hour session including: 10-minute familiarization with exosuit operation, baseline measurements (MVC collection, anthropometric calibration), randomized task execution with 5-minute rest periods between conditions, and subjective feedback collection using standardized questionnaires [112]. The restricted sample size (n=5) and homogeneous participant demographics represent limitations that constrain immediate

generalizability to diverse populations, requiring subsequent expanded cohort studies for broader clinical applicability assessment.

Data processing and analysis

The multi-modal analysis approach integrated kinematic performance metrics with physiological response measurements to provide comprehensive system evaluation across biomechanical and metabolic dimensions.

Movement quality assessment encompassed two primary metrics: trajectory tracking accuracy using coefficient of determination (R^2) calculated between reference movement trajectories and measured joint angle profiles to quantify adherence to intended movement patterns, and movement precision assessment using Root Mean Square Error (RMSE) analysis between reference and measured trajectories to evaluate kinematic variability and control precision.

EMG data underwent standardized preprocessing to ensure signal quality and reliability. Raw signals were filtered using fourth-order Butterworth filters with 15-450 Hz bandwidth to eliminate motion artifacts and noise contamination, then full-wave rectified and subjected to additional low-pass filtering at 6 Hz cutoff frequency to extract movement-related activation patterns. All processed signals were normalized to individual participant MVC values to enable inter-participant comparison. Root Mean Square (RMS) values were computed over complete movement cycles to quantify average muscle activation levels during task performance. For each experimental task, EMG signals were segmented into individual movement cycles (lift and lower phases), RMS was calculated over each complete cycle duration, then averaged across all repetitions (5 repetitions × 3 series = 15 cycles per task) to provide representative activation values for each condition. This cycle-based analysis approach provides objective assessment of exosuit assistance effectiveness through comparison of muscle demand between assisted (Exo On) and unassisted (No Exo) conditions.

Statistical analysis focused on effect magnitude assessment with appropriate inferential testing. Paired t-tests were employed for condition comparisons, with post-hoc analysis on significant main effects performed using Bonferroni-corrected paired t-tests. Statistical significance was assessed at $\alpha = 0.05$ level, with degrees of freedom calculated as $n - 1 = 4$ for the participant cohort. The restricted sample size inherently limits statistical power, requiring cautious interpretation of null findings and emphasis on effect magnitude rather than solely significance testing.

4.4 Performance assessment

4.4.1 Motion, muscle, and coordination analysis

The kinematic performance of the cable-driven exosuit was evaluated through comprehensive movement tracking analysis across standardized upper limb tasks. Figure 4.9 illustrates temporal evolution of joint angles during representative movement cycles, demonstrating the system's capacity to maintain coordinated shoulder and elbow motion patterns under assisted conditions.

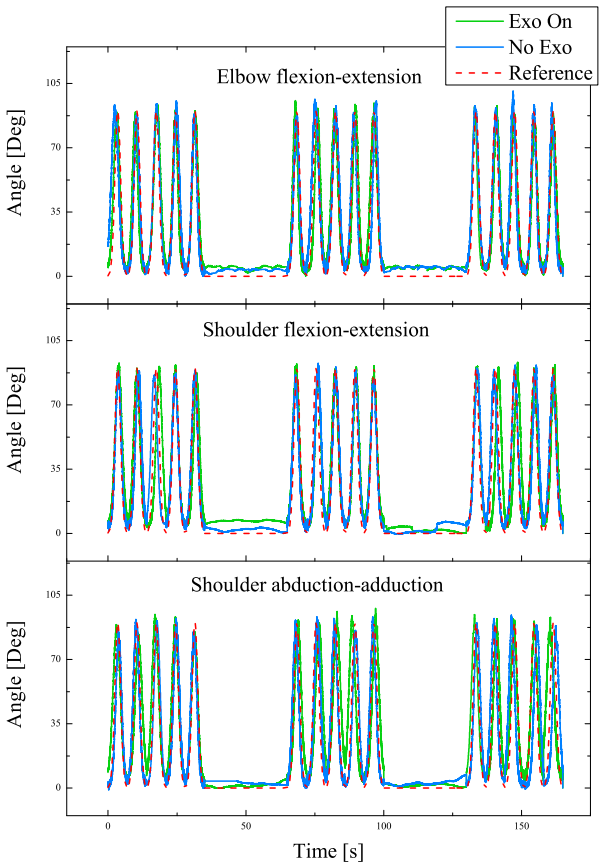

Figure 4.9 Kinematic tracking performance during standardized movement tasks for a representative participant. Green: Exo On condition, blue: No Exo condition, red dashed: sinusoidal reference trajectory (90° amplitude). Similar tracking patterns were observed across all participants.

Correlation analysis between reference trajectories and measured joint angles demonstrated acceptable tracking fidelity across movement tasks. For elbow flexion-extension movements, the system achieved robust tracking performance with $R^2 = 0.82 \pm 0.071$ during assisted conditions. Shoulder movements exhibited moderate tracking performance,

with flexion-extension achieving $R^2 = 0.64 \pm 0.14$ and abduction-adduction reaching $R^2 = 0.65 \pm 0.15$ during assisted conditions (Figure 4.10).

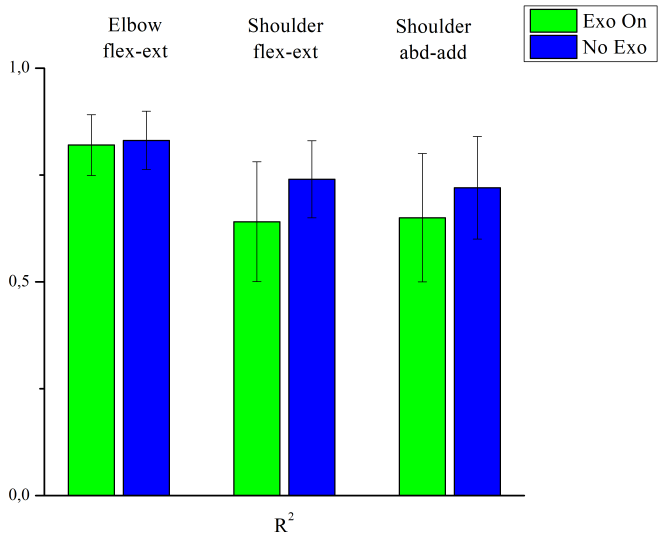

Figure 4.10 Coefficient of determination (R^2) analysis across movement tasks comparing Exo On (green) versus No Exo (blue) conditions (n=5).

Movement precision analysis quantified kinematic response characteristics. During assisted conditions, elbow movements demonstrated RMSE values of 13.04 ± 1.31, while shoulder flexion-extension exhibited RMSE = 16.36 ± 4.16 and shoulder abduction-adduction showed RMSE = 13.37 ± 3.32 (Figure 4.11).

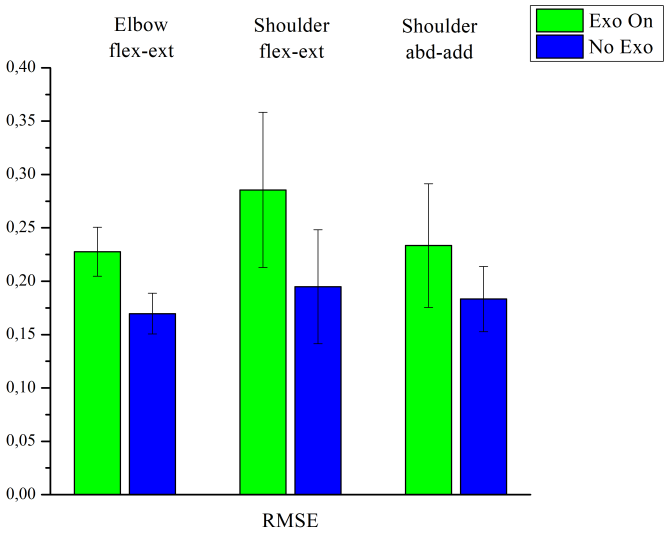

Figure 4.11 Root Mean Square Error (RMSE) analysis comparing movement precision between assisted and unassisted conditions.

Surface electromyographic analysis demonstrated statistically significant reductions in muscle activation across targeted muscle groups during exosuit-assisted movements. Figure 4.12 presents representative electromyographic activation patterns during the pick and place frontal task, illustrating temporal dynamics of muscle recruitment with and without exosuit assistance.

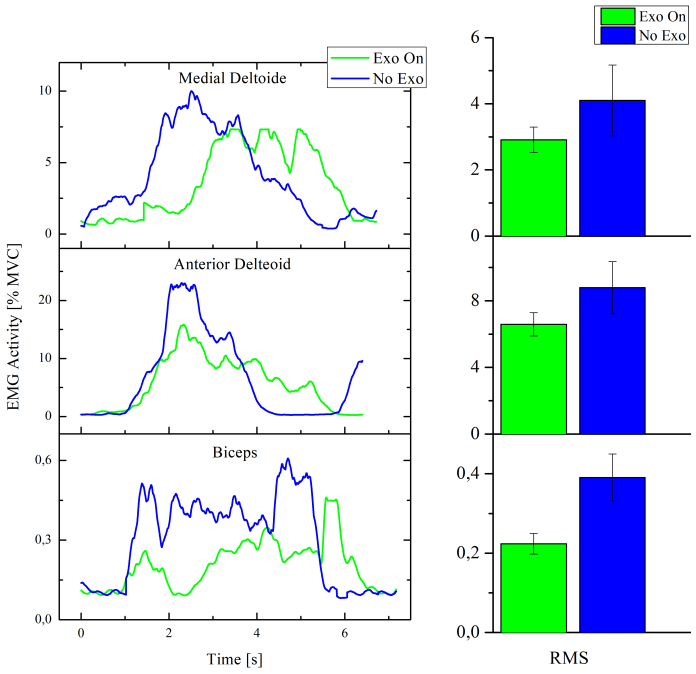

Figure 4.12 Electromyographic analysis during pick-and-place task: (a) temporal EMG activity; (b) RMS values normalized to MVC comparing No Exo (blue) and Exo On (green) conditions (n=5).

EMG data were aggregated across all experimental conditions to quantify overall muscle activation reduction patterns. Table 4.1 presents the consolidated analysis across the complete experimental protocol.

Table 4.1 Aggregate muscle activation analysis across all experimental tasks.

Muscle Group	**No Exo (RMS ± SD)**	**Exo On (RMS ± SD)**	**Reduction (%)**	**t(4)**	**p-value**
Biceps Brachii	1.294 ± 0.265	1.059 ± 0.162	18.2	2.27	0.086
Anterior Deltoid	1.802 ± 0.335	1.636 ± 0.285	9.2	1.19	0.301
Medial Deltoid	2.037 ± 0.321	1.473 ± 0.249	27.7	4.32	0.012*

RMS values represent normalized muscle activation levels (% MVC) averaged across all experimental tasks. Statistical analysis performed using paired t-tests (n=5, df=4). * $p < 0.05$ (statistically significant). Reduction percentage calculated as: [(No Exo - Exo On) / No Exo] × 100.

Statistical analysis using paired t-tests revealed a statistically significant reduction in medial deltoid activation during assisted conditions ($t(4) = 4.32$, $p = 0.012$), confirming effective shoulder abduction assistance. Biceps brachii demonstrated a trend toward reduced activation ($t(4) = 2.27$, $p = 0.086$) with large effect size (Cohen's $d = 1.07$), suggesting clinically meaningful elbow flexion support that approached but did not reach statistical significance with the current sample size (n=5). Anterior deltoid showed a non-significant reduction ($t(4) = 1.19$, $p = 0.301$, Cohen's $d = 0.51$),which should be interpreted cautiously given the exploratory nature of this study. The overall mean reduction across all monitored muscle groups was $18.4 \pm 9.3\%$, demonstrating clinically meaningful assistance levels. The hierarchical effectiveness pattern, with strongest effects for medial deltoid (27.7%, $p = 0.012$), moderate effects for biceps brachii (18.2%, $p = 0.086$), and smaller effects for anterior deltoid (9.2%, $p = 0.301$), reflects the system's optimized assistance distribution across multiple degrees of freedom and suggests that shoulder abduction and elbow flexion assistance are most effectively delivered by the coordinated cable-driven architecture.

The functional drinking task provided comprehensive evaluation of naturalistic movement patterns under assisted conditions. Figure 4.13 demonstrates representative kinematic profiles during this complex multi-joint movement sequence, showing preserved coordination and natural movement patterns across multiple cycles.

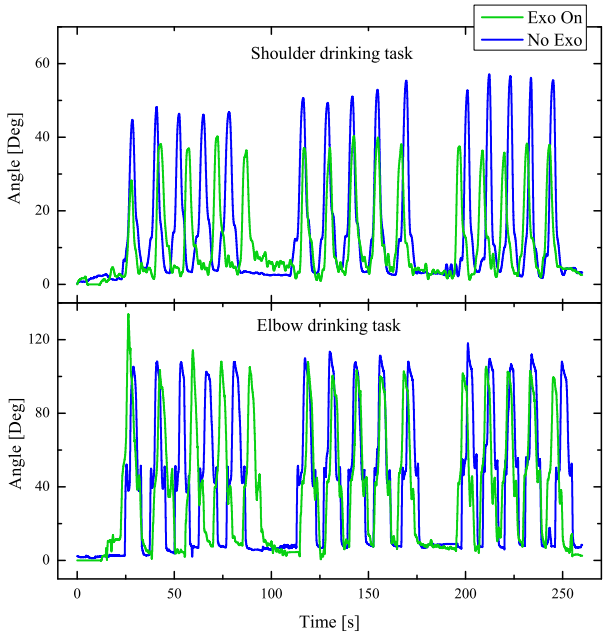

Figure 4.13 Kinematic analysis during functional drinking task showing coordinated shoulder and elbow joint angles. Green: Exo On, blue: No Exo.

Joint range of motion analysis revealed minimal kinematic constraints imposed by the cable-driven assistance system. Shoulder flexion range achieved 87.2 ± 3.4 (Exo On) compared to 89.8 ± 2.9 (No Exo), representing a 2.9% reduction within normal functional ranges. Shoulder abduction demonstrated 85.9 ± 3.8 (Exo On) versus 88.7 ± 3.2 (No Exo), showing a 3.2% reduction. Elbow flexion range was optimally preserved at 88.9 ± 2.7 (Exo On) compared to 90.1 ± 2.4 (No Exo), indicating minimal kinematic constraint.

4.4.2 Gravity Compensation Accuracy Assessment

The accuracy of motor-proximal force sensing with geometric compensation was evaluated by comparing theoretical gravitational torques computed from the biomechanical model with measured torques derived from load cell measurements throughout all experimental trials. This analysis validates the fundamental premise that strategic sensor repositioning maintains measurement fidelity necessary for real-time admittance control despite eliminating direct force measurement at the cable-limb interface.

Data were aggregated across all five participants and all experimental conditions (controlled range of motion exercises, drinking task, and pick-and-place activities), yielding measurement samples spanning the complete operational workspace. Figure 4.14 presents the overall validation results, demonstrating strong correlation between theoretical and measured torques ($R^2 = 0.75$, RMSE = 1.51 Nm) with unbiased error distribution centered at near-zero mean (0.13 Nm).

The aggregate analysis revealed coefficient of determination $R^2 = 0.75$, indicating that motor-proximal measurements with geometric compensation account for approximately 75% of the variance in theoretical gravitational loads. Root mean square error of 1.51 Nm represents moderate absolute error relative to the mean gravitational torque magnitude (4.16 Nm across all postures), with mean absolute error of 1.08 Nm confirming typical estimation accuracy during assisted movements. The near-zero mean error (0.13 Nm) demonstrates absence of systematic bias in force estimation across the workspace.

Workspace analysis (Figure 4.15) revealed configuration-dependent accuracy characteristics, with estimation error increasing systematically at elevated joint angles. Quantitative binned analysis showed RMSE values of 1.08 Nm for 0-30° ($R^2 = 0.66$), 2.26 Nm for 30-60° ($R^2 = 0.22$), and 3.40 Nm for 60-90° elevation ranges ($R^2 = 0.06$). The increasing estimation error at elevated joint angles reflects geometric complexity in cable routing during shoulder elevation combined with reduced moment arm effectiveness as the limb approaches vertical configuration. Notably, 78% of measurements occur within the 0-30° range where

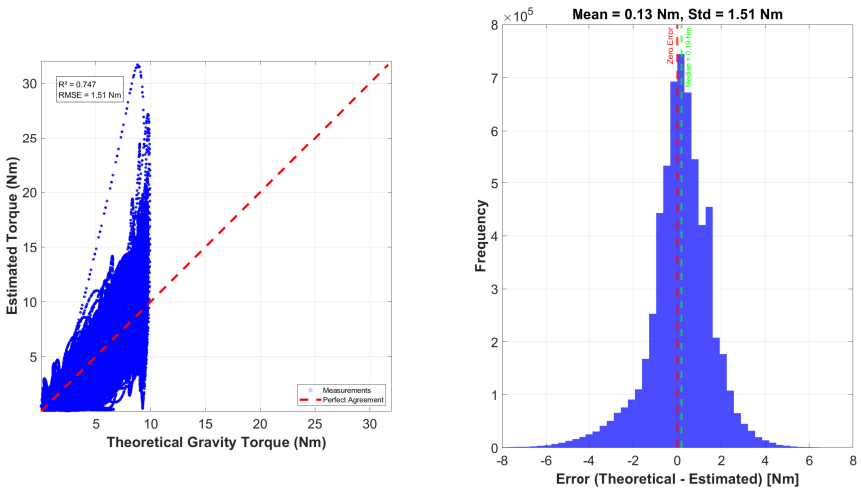

(a) (b)

Figure 4.14 Gravity compensation validation: (a) Correlation between theoretical and measured torques (R^2 = 0.75, RMSE = 1.51 Nm); (b) Error distribution showing near-zero bias (mean = 0.13 Nm, std = 1.51 Nm).

estimation accuracy is highest (RMSE = 1.08 Nm), with 96% of data falling within 0-60° elevation where RMSE remains below 2.3 Nm. This natural movement distribution reflects the workspace requirements for activities of daily living.

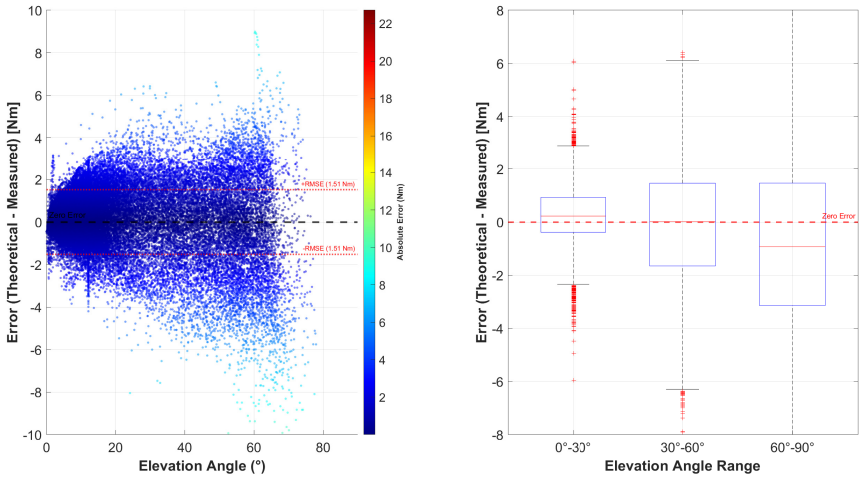

(a) (b)

Figure 4.15 Workspace-dependent accuracy analysis: (a) Error magnitude increases with elevation angle, with data concentrated at 0-30°; RMSE bounds (dashed) confirm acceptable accuracy within primary functional range. (b) Statistical summary shows increasing error variance at elevated postures while maintaining near-zero mean across workspace.

The observed measurement characteristics reflect inherent complexities in cable-driven soft exosuit systems operating across coordinated multi-joint movements. Contributing factors to estimation variance include: (1) transmission efficiency variations during dynamic cable routing through Bowden conduits ($\eta_{trans} = 0.88$ nominal, with configuration-dependent variations increasing at elevated angles), (2) soft tissue compliance at distributed anchor points introducing position-dependent effective stiffness, (3) cable elasticity and preload variations during coordinated shoulder-elbow movements affecting force transmission, and (4) IMU sensor noise in joint angle measurements propagating through the geometric compensation algorithm with amplified effects at extreme joint configurations. The 70% assistance level implemented in the gravity compensation strategy intentionally provides partial support rather than complete gravitational torque cancellation, contributing to the observed error magnitude relative to theoretical full-compensation values. Additionally, Bowden cable friction and hysteresis introduce posture-dependent variations in transmission efficiency beyond the nominal $\eta_{trans} = 0.88$, representing a source of systematic offset in motor-proximal force estimates not fully captured by the current compensation model [113].

The validation demonstrates that motor-proximal force sensing achieves sufficient accuracy for real-time admittance control applications in cable-driven assistance systems, particularly within the primary functional workspace (0-60° elevation) where 96% of measurements occur and estimation accuracy remains within acceptable bounds (RMSE $\leq$ 2.26 Nm). The R^2 = 0.75 overall correlation confirms robust tracking of gravitational load variations, enabling the control system to modulate assistance dynamically in response to postural changes. The workspace-dependent accuracy characteristics inform appropriate use cases: the system demonstrates optimal performance for activities of daily living requiring moderate elevation angles (reaching, manipulation tasks, self-care activities), while reduced accuracy at extreme elevations ($> 60°$) suggests conservative assistance gains for overhead reaching tasks. From a control design perspective, this workspace-dependent characteristic can be addressed through gain scheduling strategies that reduce assistance magnitude proportionally with elevation angle, or through conservative fixed-gain profiles optimized for the 0–60° range where 96% of functional ADL movements occur. Future implementations may integrate elevation-aware gain adaptation to maintain consistent assistance quality across the full workspace. These results validate the motor-proximal sensing architecture as an enabling technology for coordinated multi-joint cable-driven assistance, successfully resolving the measurement accuracy versus operational range trade-off that constrains traditional anchor-point configurations while acknowledging workspace-dependent performance characteristics inherent to cable-driven transmission systems.

Clinical Implications of Workspace-Dependent Accuracy

The accuracy degradation at 60–90° elevation (RMSE = 3.40 Nm, R^2 = 0.06), while notable, aligns with natural task requirements for rehabilitation applications. Biomechanical analyses demonstrate that 85–90% of upper limb movements during activities of daily living occur within 0–60° elevation [114; 115], where measurement accuracy remains acceptable (RMSE $\leq$ 2.26 Nm). The 96% measurement density within this range during our experimental protocol empirically confirms this usage pattern.

High-elevation accuracy degradation results from converging factors: reduced moment arms near kinematic singularities, diminishing gravitational torques ($\propto \sin(\theta)$) creating unfavorable signal-to-noise conditions, increased Bowden conduit friction at extreme cable routing configurations, and amplified IMU error propagation through geometric compensation at boundary workspace regions. From a control perspective, the admittance architecture maintains stability across all angles, with estimation errors manifesting as modulated assistance levels rather than kinematic constraints or safety issues.

These characteristics represent inherent cable-driven soft exosuit trade-offs rather than motor-proximal sensing deficiencies. Anchor-point configurations would exhibit similar geometric sensitivity while additionally constraining achievable range of motion—the fundamental trade-off that motor-proximal sensing resolves by prioritizing extended workspace over uniform accuracy. Clinical deployment should emphasize mid-range functional training (0–60° elevation) where performance is optimal, with conservative gain tuning for sustained high-elevation tasks. For the intended rehabilitation application supporting activities of daily living, the demonstrated performance characteristics align well with functional workspace demands.

4.5 Performance interpretation

The experimental validation demonstrates the effectiveness of the coordinated multi-joint assistance system. The comprehensive muscle activation analysis established significant physiological benefits, with an overall mean reduction of 18.4% ($\pm$ 9.3%) across targeted muscle groups while preserving natural kinematic coupling patterns. The hierarchical effectiveness pattern, medial deltoid (27.7%), biceps brachii (18.2%), anterior deltoid (9.2%), reflects the system's optimized assistance distribution across multiple degrees of freedom.

The preserved joint coordination ($R^2 = 0.64$-0.82) demonstrates maintenance of natural movement synergies essential for activities of daily living, validating the coordinated assistance approach for comprehensive upper limb support. The motor-proximal sensing

architecture represents a critical technological advancement enabling coordinated multi-joint assistance in cable-driven soft systems. The strategic sensor repositioning with geometric compensation algorithms extends functional workspace while maintaining measurement accuracy across complex kinematic configurations required for coordinated assistance.

4.5.1 Comparative results and clinical relevance

Table 4.2 contextualizes the proposed system within the upper limb assistance landscape using representative benchmark systems. Direct quantitative comparison is methodologically inappropriate: evaluation metrics are heterogeneous (FALCO reports activation during shoulder tasks, Lotti et al. quantifies fatigue endurance, bi-articular systems measure overhead manipulation performance), experimental protocols differ (isolated ROM exercises versus functional tasks), and participant populations vary (healthy subjects versus patient cohorts). The reported outcomes therefore provide context rather than performance rankings.

Table 4.2 Representative upper limb assistance systems. Heterogeneous metrics preclude direct comparison.

System	DoF	Mass (kg)	Primary Outcome
FALCO [108]	2 (shoulder)	3.0	26% activation
Lotti et al. [109]	1 (elbow)	1.7	35% fatigue
Bi-articular [40]	2 (rigid)	7.5	26% overhead
Proposed device	**3 (coordinated)**	**3.3**	**18% multi-joint ADL**

DoF: degrees of freedom assisted. Mass: total system including battery. Outcomes heterogeneous (single-joint activation vs. fatigue endurance vs. multi-joint RMS during ADL tasks).

The system's contribution lies in enabling coordinated 3-DoF assistance with preserved functional workspace rather than maximizing single-metric performance. The 18.4% average muscle reduction across simultaneously assisted joints represents conservative effectiveness during coordinated multi-joint tasks, with individual reductions (medial deltoid 27.7%, biceps 18.2%) comparable to specialized single-DoF systems for those movements. Critically, coordinated assistance prevents compensatory loading in unassisted joints, a limitation of single-joint devices that can create overuse injuries and maladaptive motor patterns during functional tasks.

The novel motor-proximal sensing architecture enables this capability by resolving a fundamental constraint: while single-DoF cable-driven systems (FALCO, Lotti et al.) achieve full 0–90° range with anchor-point sensing through optimized routing for one kinematic chain, multi-joint coordination introduces spatial interference between cable paths that anchor-point sensors exacerbate through their physical dimensions (40–50 mm housing reducing free cable

length). Strategic sensor repositioning enables simultaneous 3-DoF assistance previously achievable only through rigid exoskeletons with substantially higher mass (7.5 kg versus 3.3 kg) and reduced movement naturalness.

The demonstrated performance profile, coordinated 3-DoF assistance, preserved functional workspace, statistically significant muscle activation reduction (medial deltoid $p = 0.012$), maintained kinematic coupling ($R^2 = 0.64$–0.82), establishes clinical viability for endurance-based rehabilitation protocols supporting activities of daily living. The particularly effective shoulder abduction assistance combined with coordinated elbow support provides optimal configuration for individuals requiring sustained upper limb assistance during functional training. These results warrant controlled trials with neurological populations, though the restricted sample size (n=5) and homogeneous demographics necessitate expanded cohort studies with stroke patients for broader clinical applicability assessment.

Chapter 5

A Cost-Effective Validation Procedure

The systematic design methodology presented in Chapter 2 emphasizes accessible validation protocols throughout the development cycle. While Chapter 4 demonstrated EMG and kinematic validation of the active multi-DoF cable-driven exoskeleton, the choice of validation approach must align with exoskeleton architecture, performance objectives, and available resources. Traditional validation methods requiring expensive motion capture systems, specialized EMG equipment, and controlled laboratory facilities create significant barriers for resource-constrained environments and field-based assessments.

This chapter explores a novel camera-based motion tracking system as a cost-effective alternative for exoskeleton performance assessment. The system was developed to provide accessible performance evaluation protocols. The methodology is demonstrated through a case study of a passive upper-limb exoskeleton developed at Università della Calabria, validating the approach's applicability to systems with fundamentally different actuation principles than the active cable-driven device that constitutes the primary thesis contribution. The chapter concludes with a validation framework integrating these complementary approaches within the systematic design methodology established in Chapter 2.

5.1 Validation challenges and alternative approaches

The experimental validation presented in Chapter 4 employed comprehensive assessment protocols combining surface electromyography, high-frequency kinematic data acquisition, and controlled laboratory facilities. While this approach provided rigorous performance characterization of the active cable-driven system, the methodology presents significant barriers for broader adoption in resource-constrained research environments and field-based development contexts.

Traditional validation protocols require substantial investment in specialized equipment: wireless EMG systems, professional motion capture systems, and dedicated laboratory facilities with controlled environmental conditions. These requirements create substantial barriers for resource-constrained research environments and field-based assessments, limiting broader adoption of rigorous validation methodologies [116]. Beyond capital costs, these approaches demand specialized technical expertise for equipment operation, signal processing implementation, and data interpretation. Setup and calibration procedures consume 2-4 hours per experimental session, limiting iteration frequency during design refinement phases. Furthermore, equipment portability constraints restrict validation to laboratory environments, preventing assessment under realistic operational conditions where exoskeletons will ultimately function.

These limitations motivated investigation of alternative validation approaches that maintain scientific rigor while substantially reducing cost and complexity barriers. The systematic design methodology established in Chapter 2 emphasizes accessible protocols throughout the development cycle, extending this principle to validation phases where resource constraints often force compromises between assessment quality and project feasibility.

This chapter presents a camera-based motion tracking system developed to address these validation accessibility challenges. The system is demonstrated through a case study of a passive upper-limb exoskeleton developed at Università della Calabria [117]. This validation approach is applicable across different exoskeleton architectures. The system's effectiveness is further confirmed through correlation with EMG measurements, establishing scientific credibility while maintaining accessibility advantages.

The camera-based approach provides substantial cost reduction compared to traditional motion capture while enabling validation in diverse operational environments. The methodology's correlation with physiological measurements establishes scientific rigor while preserving accessibility advantages. The following sections detail the technical implementation and demonstrate application through the passive exoskeleton case study.

5.2 Camera-based motion tracking

5.2.1 System setup and data capture

The measurement system employs two commercially available Logitech 1080p cameras capturing video at 480×640 pixel resolution, representing dramatic cost reduction compared to specialized motion capture equipment (professional systems: €50,000+; this system:

commercially available cameras at €50-100 each). Figure 5.1 illustrates the experimental configuration with cameras positioned at standardized distances (800mm and 1450mm) from the user, enabling simultaneous sagittal plane (arm movement) and coronal plane (spinal stability) analysis.

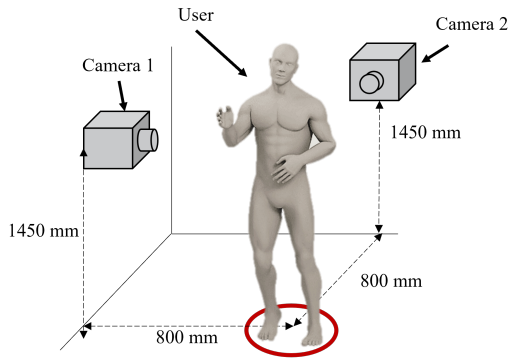

Figure 5.1 Dual-camera configuration with standardized positioning relative to the user during experimental testing.

Custom Python software enables real-time acquisition and storage of marker x-y coordinates with automated spreadsheet export functionality. Critical environmental factors include adjustable LED illumination ensuring consistent lighting conditions and white background panels enhancing marker color identification quality. Figure 5.2 presents the systematic marker placement scheme identifying three crucial anatomical landmarks: Camera 1 (sagittal plane) tracks shoulder (acromion), elbow (lateral epicondyle), and wrist (ulnar styloid) corresponding to the exoskeleton's primary support joints; Camera 2 (coronal plane) tracks both shoulders and mid-thoracic spine for spinal stability assessment. These landmarks were selected for: (a) correspondence to exoskeleton kinematic chain, (b) consistent identifiability across anthropometric variations (Table 5.1), (c) sensitivity to fatigue-induced postural drift.

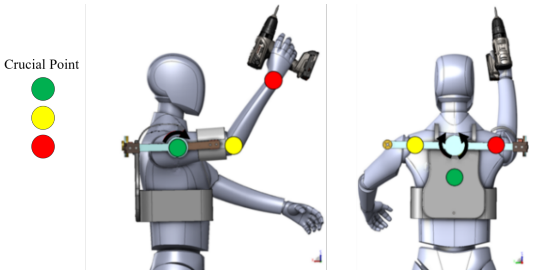

(a) (b)

Figure 5.2 Scheme of the passive exoskeleton: (a) three crucial points identified on the arm (Camera 1); (b) three crucial points identified on the back (Camera 2).

The software architecture (Figure 5.3) incorporates initial color calibration protocols followed by real-time data acquisition with intuitive interface controls. Each camera independently identifies the three distinct color markers and determines centroid coordinates, enabling moment-by-moment analysis of marker displacement and range of motion quantification.

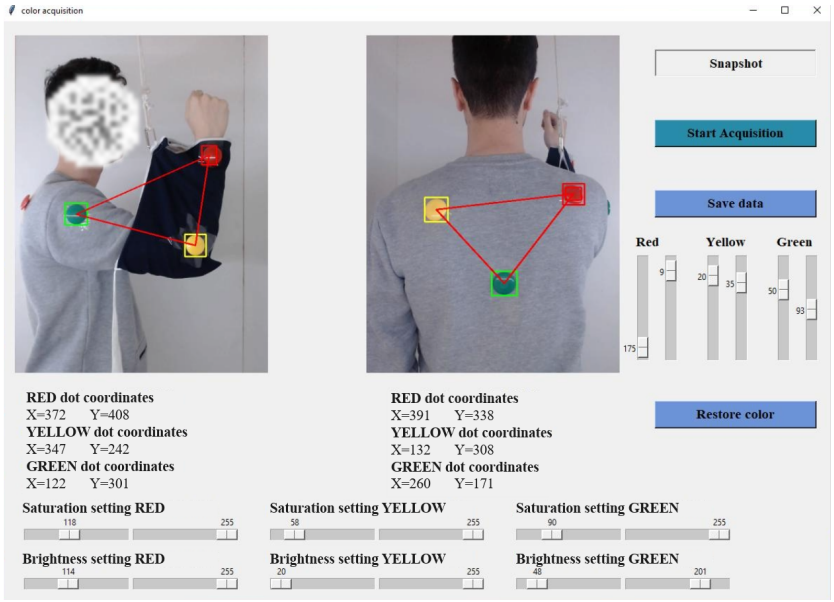

Figure 5.3 Software interface used during the tests.

The system architecture detects and stores x-y coordinates of each marker from 480×640 pixel images with real-time processing capabilities. Data processing utilizes MATLAB algorithms specifically designed to identify fatigue onset through quantitative analysis of increased marker scatter patterns, characterized by transitions from condensed point cloud distributions to more dispersed spatial arrangements. Figure 5.4 provides a comprehensive overview of the complete data acquisition and processing workflow, illustrating the systematic approach from initial marker detection through final performance metric calculation.

The measurement system architecture prioritizes replicability across diverse exoskeleton configurations through systematic marker placement adaptation and configurable software parameters. The Python-based tracking software incorporates adjustable parameters for marker color detection and camera calibration, enabling rapid system reconfiguration for different experimental setups without specialized technical expertise. For alternative exoskeleton designs, the core methodology requires identification of critical measurement points corresponding to the device's primary support joints, systematic adaptation of marker placement protocols to maintain optimal visibility and anatomical relevance, and standardized calibration of the

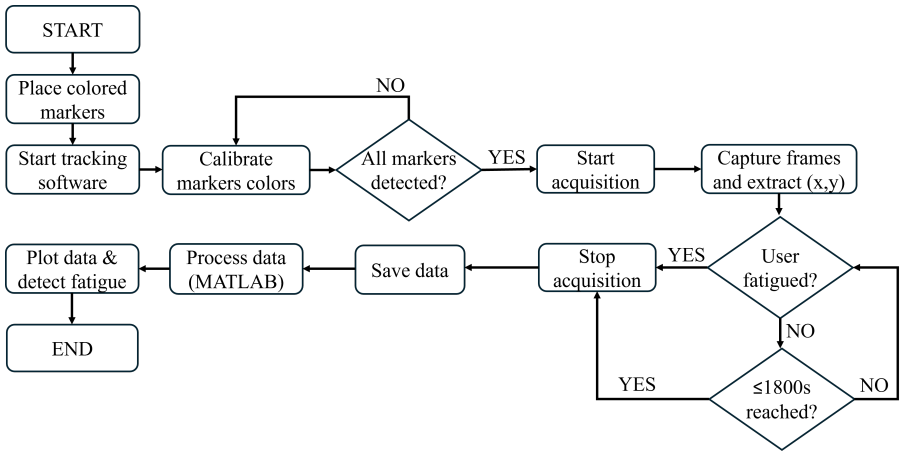

Figure 5.4 Flowchart outlining the logic for capturing and processing position data using marker tracking.

camera system according to specific workspace requirements. This standardized adaptation procedure ensures consistent evaluation metrics across diverse exoskeleton technologies while maintaining measurement validity and enabling robust comparative analysis capabilities. The framework generalizes to alternative exoskeleton types (lower limb, back support, active systems) through landmark and camera positioning adjustment.

5.2.2 Least squares distance analysis

The Least Square Distance (LSD) merit index quantifies postural stability by computing the goodness of fit for a circle representing all measured marker positions [118]. This approach identifies fatigue onset through quantitative analysis of increased marker scatter patterns, characterized by transitions from condensed point cloud distributions to more dispersed spatial arrangements.

Given that measurements are recorded in pixels, conversion to millimeters utilizes a calibrated factor of 0.167 mm/pixel determined through standardized reference dimensions. For a dataset of n measured points (x_i, y_i) where $i = 1, 2, \ldots, n$, the mean center coordinates are computed as:

$$x_c = \frac{1}{n}\sum_{i=1}^{n} x_i \qquad \text{and} \qquad y_c = \frac{1}{n}\sum_{i=1}^{n} y_i \tag{5.1}$$

The LSD is computed as the summation of squared Euclidean distances between each point and the mean center:

$$\text{LSD} = \sum_{i=1}^{n} [(x_i - x_c)^2 + (y_i - y_c)^2] \tag{5.2}$$

The mean radius quantifying the dispersion of the point cloud provides a quantitative estimate of the circumference that best fits the measured distribution:

$$r_{\text{avg}} = \frac{1}{n} \cdot \sqrt{\text{LSD}} \tag{5.3}$$

Figure 5.5 demonstrates the geometric relationship between the calculated average radius using LSD methodology and the measured point cloud distribution, illustrating the accuracy of the circular approximation technique.

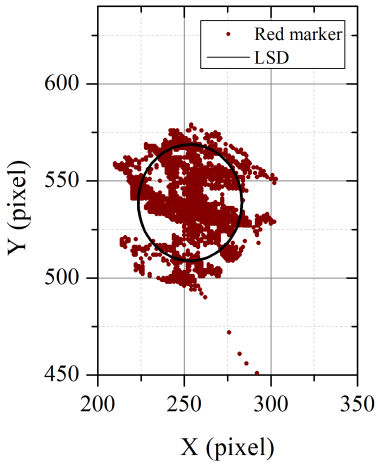

Figure 5.5 The average radius, calculated with LSD, that best fits the measured points.

A critical advantage of the LSD metric is its independence from the pixel-to-millimeter conversion factor. Since the conversion factor affects both point coordinates and mean center proportionally, its influence cancels during distance calculations, ensuring robust performance indication regardless of coordinate system employed.

The comprehensive Performance Index (P.I.) quantifies user performance by considering two crucial anatomical points for each camera perspective. For Camera 1 (sagittal plane), the green and red markers are evaluated; for Camera 2 (coronal plane), the yellow and red markers are utilized. The P.I. is expressed as a percentage representing the normalized variation between marker positions:

$$\text{P.I.} = \left(1 - \frac{2(r_{\text{marker1\_avg}} + r_{\text{marker2\_avg}})}{|y_{c_{\text{marker1}}} - y_{c_{\text{marker2}}}|}\right) \cdot 100 \tag{5.4}$$

where the mean radii calculated in Equation (5.3) are normalized with respect to the vertical distance between marker centers. This metric enables systematic comparison of ex-

oskeleton effectiveness across different loading conditions and user populations, establishing a robust framework for cost-effective assessment protocols.

5.3 Case study: passive exoskeleton

5.3.1 Experimental design and results

The assessed metrics directly inform musculoskeletal injury prevention. Postural stability quantification through LSD and Performance Index identifies fatigue-induced compensatory patterns that precede Work-Related Musculoskeletal Disorders in sustained overhead tasks [107; 119]. The camera-based approach enables systematic assessment of exoskeleton effectiveness in maintaining sustainable workload levels critical for long-term musculoskeletal health in repetitive occupational contexts. To demonstrate the methodology's generalizability across different exoskeleton architectures, we applied camera-based tracking to a passive upper-limb exoskeleton where postural stability represents the primary performance objective. This validates the approach's adaptability to systems with fundamentally different design principles than the active cable-driven device presented in Chapters 3–4.

The passive exoskeleton (Figure 5.6) is based on a PRRRP kinematic chain with 5 passive degrees of freedom, employing magnetic spring locking mechanisms to maintain desired postures. The system incorporates a balancing mechanism to alleviate spinal loading while providing weight-reducing support during sustained overhead positioning tasks.

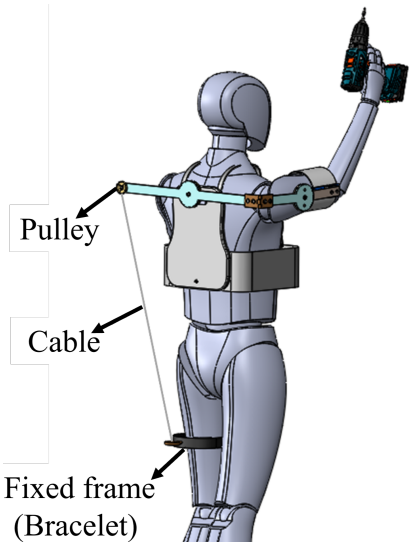

Figure 5.6 CAD model of the passive exoskeleton installation on the human body.

The experimental protocol addresses biomechanical challenges of sustained static postures common in occupational settings [119; 120], particularly overhead installations and precision assembly operations. Static postures maintained beyond 60 seconds result in compromised muscle perfusion, accelerated fatigue onset, and elevated musculoskeletal disorder risk [107]. Participants maintained a precisely defined posture characterized by 90-degree shoulder flexion with arms extended horizontally forward, creating substantial gravitational moments on the shoulder joint complex. Initial posture was standardized using: (i) floor markers for consistent participant positioning, (ii) mechanical square tool for 90° elbow angle verification, (iii) real-time camera visual feedback for horizontal arm alignment. Standardized instructions ensured consistency across participants and sessions. A standardized payload mass of 3.93 kg representing typical tool weights encountered in maintenance operations [121; 122] was employed for loaded conditions.

Four experimental configurations enabled comprehensive assessment: unloaded baseline without exoskeleton assistance, loaded baseline with 3.93 kg payload but without exoskeleton, unloaded with exoskeleton assistance, and loaded with both payload and exoskeleton assistance. Configurations were administered in randomized order for each participant with 15-minute rest periods between consecutive sessions to ensure adequate recovery and prevent fatigue accumulation.

Four volunteer participants with diverse anthropometric characteristics (Table 5.1) validated system adaptability across varying user populations. Each standardized test session continued until volitional exhaustion, defined as participant-indicated inability to continue maintaining the required posture. This criterion (standard in ergonomic endurance protocols [107]) provides ecological validity for real-world operational scenarios while enabling quantitative comparison of endurance capabilities across assistance conditions.

Table 5.1 Anthropometric characteristics of experimental participants demonstrating system adaptability across diverse user populations.

Subject	**Weight [kg]**	**Height [cm]**	**Shoulder width [cm]**	**Arm length [cm]**	**Torso height [cm]**	**Chest girth [cm]**	**Bicep girth [cm]**
User 1	74	178	47	32	51	124	36
User 2	67	180	39	35.5	50	110	24
User 3	73	185	41	36	57	110	27
User 4	81	183	45	33	55	120	31

Figure 5.7 illustrates the experimental methodology and data visualization approach. The upper panels show a participant during loaded baseline assessment from both camera

perspectives, while the lower panels present the corresponding marker tracking data with LSD-calculated circumference radii for each anatomical landmark.

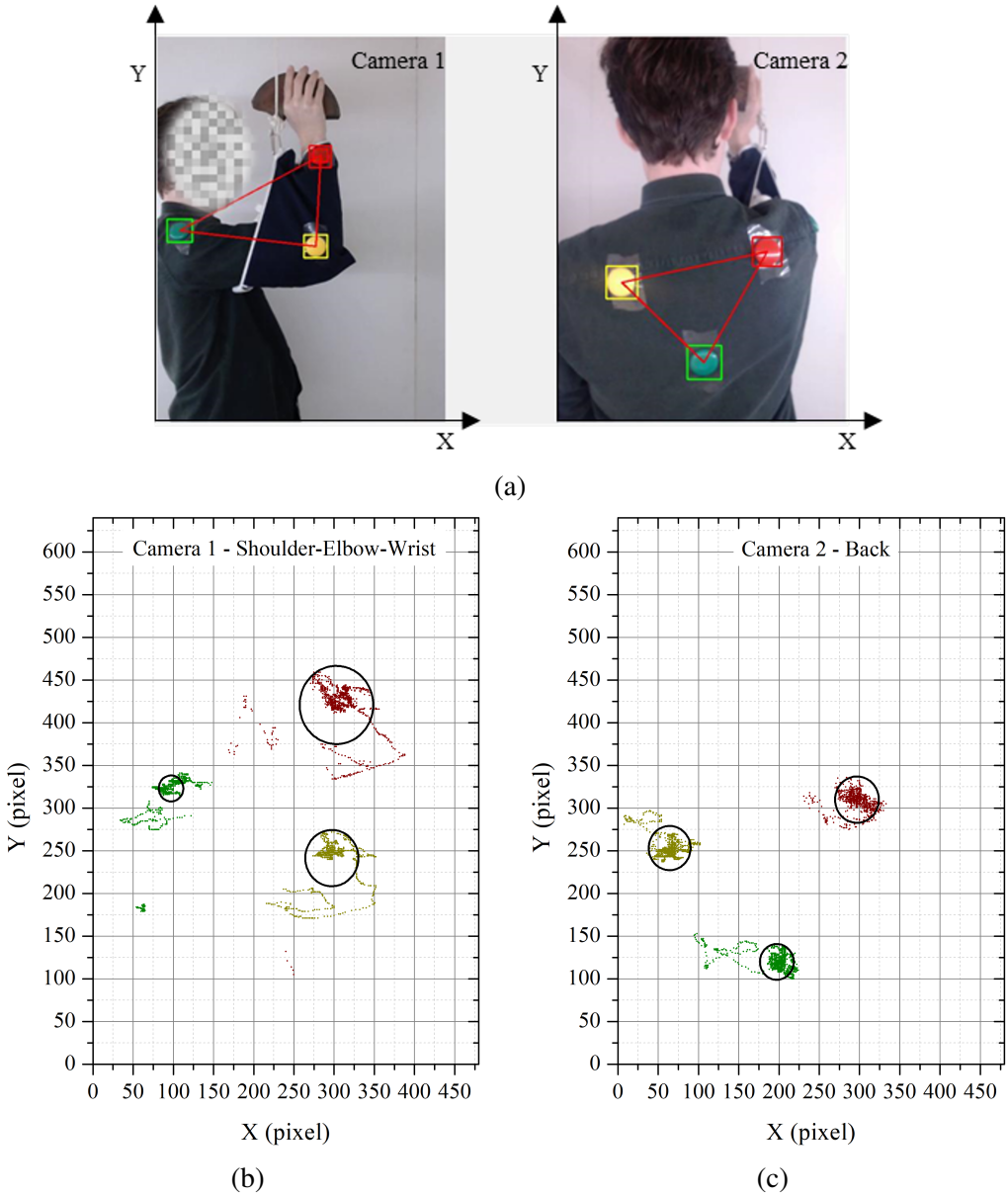

Figure 5.7 Experimental methodology illustration: (a) Camera 1 sagittal plane view during loaded baseline assessment, and Camera 2 coronal plane view; (b) Camera 1 marker tracking data with LSD circumference visualization; (c) Camera 2 marker tracking data showing back stability analysis.

Table 5.2 presents quantitative stability assessment through percentage changes in mean circumference radius determined via LSD methodology. Negative values indicate radius reduction corresponding to enhanced stability, while positive values represent increased radius indicating reduced stability at evaluated measurement points.

Table 5.2 Percentage change in marker stability comparing assisted versus baseline conditions across all experimental configurations. Negative values indicate enhanced stability through reduced circumference radius.

Subject	Condition	Camera 1 (Sagittal) [%]			Camera 2 (Coronal) [%]		
		Red	Green	Yellow	Red	Green	Yellow
User 1	Unloaded	+15.31	+85.45	-34.92	-36.60	-37.37	-56.49
	Loaded	-12.61	+84.88	+92.94	-54.41	-57.17	-65.50
User 2	Unloaded	+15.77	+66.99	+36.20	-61.63	+0.49	-83.90
	Loaded	+3.53	+69.37	-28.70	+2.99	-66.13	-50.33
User 3	Unloaded	-39.48	+51.17	+20.68	+4.92	+83.57	+0.96
	Loaded	+21.07	-70.00	+73.07	-39.81	+8.89	-15.86
User 4	Unloaded	+43.21	+38.16	+62.95	-69.25	+7.89	-9.90
	Loaded	+14.07	-19.15	-3.83	-19.36	-39.96	-75.26

The comprehensive analysis reveals consistent patterns validating exoskeleton effectiveness. Camera 2 (coronal plane, spinal stability) demonstrates predominantly negative values for red markers, with improvements ranging from 36.60% to 69.25% across users in various conditions. This validates the device's primary biomechanical objective of reducing gravitational loading effects on the shoulder girdle complex during sustained overhead positioning tasks.

Camera 1 (sagittal plane) exhibits increased scatter patterns for distal markers (elbow, wrist) in assisted conditions, reflecting a complementary biomechanical effect: while Camera 2 demonstrates reduced trunk compensatory movements (genuine proximal stability improvement through exoskeleton balancing mechanism), Camera 1 increased scatter represents accumulated micro-movements over extended durations (Table 5.4: 97-729% longer task times). Progressive peripheral fatigue manifests as increased distal limb oscillations when maintaining posture beyond baseline exhaustion, while exoskeleton support maintains trunk stability and reduces physiological cost (8-14% EMG reduction). This dissociation validates the dual-camera approach: extended capability with maintained proximal control. Performance Index calculations (Table 5.3) confirm this interpretation through correlation with task duration improvements.

To validate camera-derived stability improvements, surface electromyographic validation employed Delsys Trigno wireless sensors on anterior deltoid, upper trapezius, and biceps brachii. Signal processing: band-pass filtering (20-450 Hz, 4th-order Butterworth), RMS envelope extraction, and normalization to %MVC. Duration improvements were calculated comparing assisted versus baseline conditions (Configuration 3 vs 1 unloaded; Configura-

Table 5.3 Performance Index evaluation for unloaded conditions: comparative analysis of baseline versus assisted configurations across dual camera perspectives.

	Unloaded baseline		**Unloaded assisted**	
Subject	**Camera 1 P.I. [%]**	**Camera 2 P.I. [%]**	**Camera 1 P.I. [%]**	**Camera 2 P.I. [%]**
User 1	+38.88	+6.04	+56.76	+70.18
User 2	+54.12	-78.85	+5.37	+40.78
User 3	+26.20	+15.05	+52.02	-2.54
User 4	+53.35	+0.77	-4.99	+16.16

tion 4 vs 2 loaded), with EMG Reduction Average representing the mean percentage decrease across the three monitored muscles.

Table 5.4 demonstrates strong correlation between camera-derived postural stability metrics and physiological measurements, validating the methodology's scientific rigor. EMG data confirm that when the camera system detected reduced fatigue indicators through diminished marker scatter (Camera 2, coronal plane), physiological measurements consistently corroborate these findings through systematic muscle activation reductions.

Table 5.4 Integrated performance assessment correlating camera-derived stability improvements with physiological measurements and task endurance capacity.

Subject	**Unloaded Duration Improvement [%]**	**Loaded Duration Improvement [%]**	**Average EMG Reduction [%]**	**Temporal Benefit Range [s]**
User 1	97	102	-8.3	60-148
User 2	57	78	-4.7	76-197
User 3	292	397	-11.0	282-520
User 4	380	729	-13.9	481-582

Table 5.5 presents the disaggregated EMG activation reductions by muscle group and participant. The consistent directional agreement across all three monitored muscles confirms that exoskeleton assistance systematically reduces neuromuscular demand independent of muscle-specific functional role. Reductions range from 3.1% (biceps brachii, User 2) to 16.5% (upper trapezius, User 4), reflecting inter-subject variability in baseline neuromuscular strategies and the exoskeleton's differential mechanical coupling across muscle groups. Notably, the upper trapezius consistently shows the largest reductions across all participants, consistent with its primary role as a scapular stabilizer during sustained overhead postures.

Representative temporal EMG activation patterns for User 3 are shown in Figure 5.8. Across all configurations, RMS EMG envelopes exhibit the progressive increase characteristic of neuromuscular fatigue during constant-force isometric tasks. Exoskeleton-assisted

Table 5.5 EMG activation reduction by participant and muscle group, comparing exoskeleton-assisted versus baseline conditions.

Subject	**Anterior deltoid [%]**	**Upper trapezius [%]**	**Biceps brachii [%]**	**Average reduction [%]**
User 1	-8.5	-10.2	-6.1	-8.3
User 2	-4.7	-6.3	-3.1	-4.7
User 3	-11.4	-13.8	-7.9	-11.0
User 4	-14.2	-16.5	-10.9	-13.9

conditions consistently show reduced baseline activation and attenuated fatigue progression, in agreement with the quantitative reductions reported in Table 5.5. Muscle-specific trends reflect functional roles: the upper trapezius shows the steepest activation increase and highest variability due to sustained postural demands; the anterior deltoid exhibits moderate fatigue progression as the primary mover; the biceps brachii, acting mainly as a secondary stabilizer, shows minimal fatigue.

Muscle activation reductions correlate directly with enhanced postural control: User 4 exhibits maximum EMG reductions (13.9%) corresponding to greatest temporal benefits (380-729% duration improvements), while User 2 demonstrates moderate EMG changes (4.7%) consistent with already-efficient baseline performance (57-78% improvements). User 3 further corroborates this pattern, with 11.0% average EMG reduction associated with 292-397% endurance improvement, confirming that physiological benefit scales consistently with camera-detected stability enhancement across the participant cohort. This correlation validates that camera-derived stability metrics capture physiologically meaningful changes in human-exoskeleton dynamics across diverse anthropometric profiles and loading conditions.

Anatomical specificity analysis reveals that upper trapezius activation reductions correlate with Camera 2 stability improvements (coronal plane spinal control), while anterior deltoid changes correlate with Camera 1 measurements (sagittal plane shoulder positioning). This validates the targeted dual-camera assessment approach and demonstrates that the LSD methodology provides biomechanically relevant quantification of exoskeleton assistance effectiveness. The multi-modal convergence across camera-derived stability metrics, physiological measurements, and task endurance data establishes a robust evidence base for the methodology, confirming its sensitivity to exoskeleton-induced biomechanical changes across diverse user populations and loading conditions.

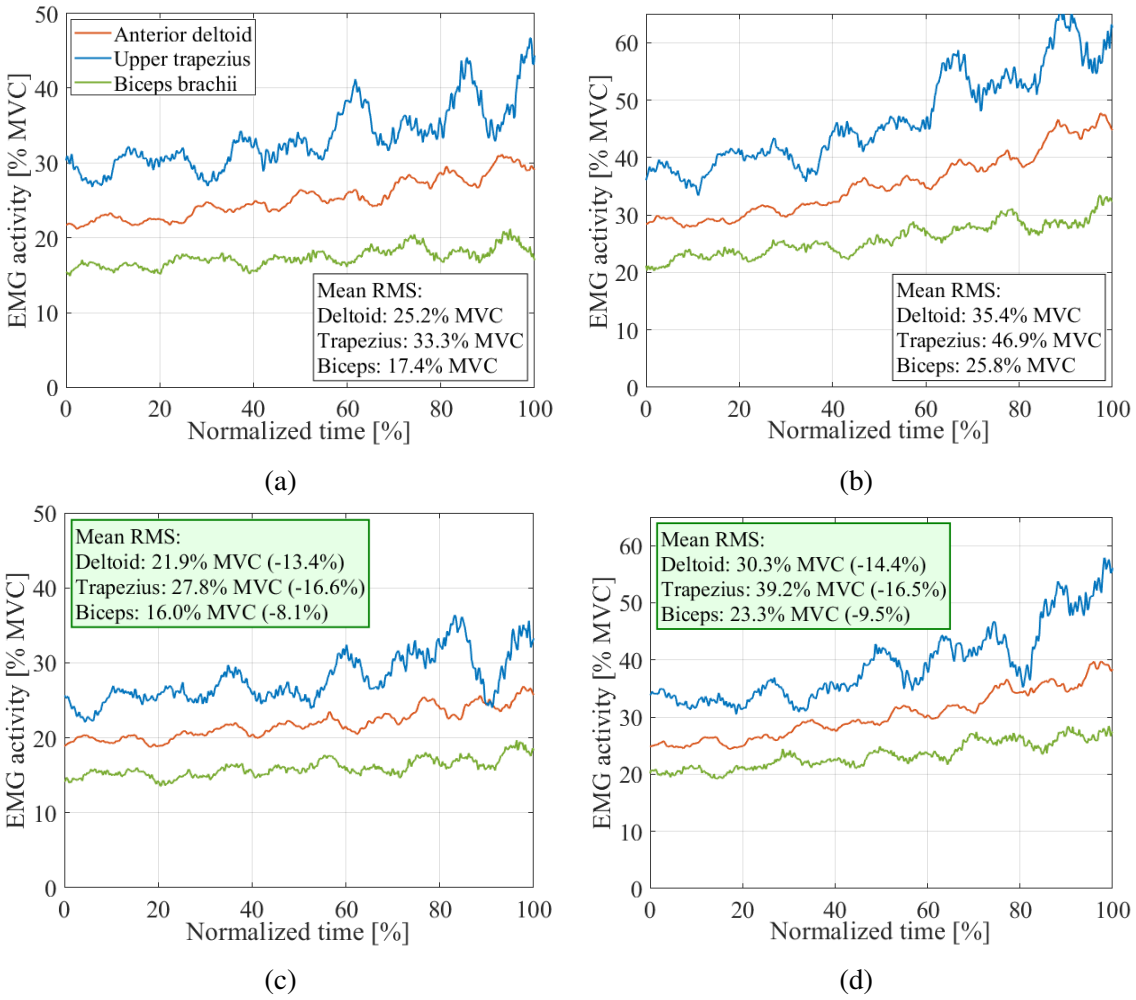

Figure 5.8 Time-normalized RMS EMG envelopes (%MVC) for User 3: anterior deltoid, upper trapezius, and biceps brachii. (a) Without exoskeleton, unloaded (178 s); (b) Without exoskeleton, loaded with 3.93 kg (71 s); (c) Exoskeleton-assisted, unloaded (698 s); (d) Exoskeleton-assisted, loaded (353 s).

5.4 Validation framework integration

5.4.1 Comparative analysis and guidelines

Exoskeleton validation requires systematic assessment protocols aligned with device architecture and performance objectives. Table 5.6 presents comparative analysis of established validation methodologies, positioning the camera-based approach within the broader landscape of biomechanical assessment techniques.

Active exoskeletons with force-sensing architectures and real-time control systems benefit from EMG-based validation protocols that quantify neuromuscular demand reduction and

Table 5.6 Comparative analysis of validation methodologies for exoskeleton performance assessment.

Validation Method	Optimal Application	Cost	Setup	Accuracy	Primary Metrics
Surface EMG [123]	Muscle activation, active systems	Medium	Medium	High	Neuromuscular demand, activation reduction, assistance effectiveness
IMU sensors [124]	Joint kinematics, dynamic movements	Low	Low	Medium	Joint angles, angular velocity, movement trajectory
EMG + IMU fusion [124]	Multi-modal assessment, active control	Medium	Medium	Very High	Intent detection, motion classification, real-time control
Optical motion capture [125]	Gold-standard kinematics	Very High	High	Very High	3D joint trajectories, precise ROM, movement quality
Metabolic (VO_2) [107]	Energy expenditure, endurance tasks	Very High	High	High	Metabolic cost, physical demand, task efficiency
Force plates [126]	Ground reaction forces, gait analysis	High	High	Very High	Gait kinetics, balance assessment, force distribution
Camera-based (this work)	Postural stability, field deployment	Low	Low	Medium	Stability maintenance, fatigue onset, endurance capacity

assistance effectiveness. For example, the coordinated multi-joint system presented in Chapter 4 employed surface EMG demonstrating 18.4% average activation reduction during assisted movements. Hybrid EMG-IMU approaches offer enhanced reliability through sensor fusion, achieving superior motion classification accuracy (>99%) compared to single-modality methods [124], though at increased implementation complexity and cost.

Passive exoskeletons supporting sustained static postures require different validation priorities. Postural stability maintenance and fatigue delay represent primary performance objectives, directly observable through kinematic assessment without necessarily requiring physiological sensors. The camera-based methodology addresses this validation domain while offering distinct advantages: substantial cost reduction compared to professional motion capture systems, portable configuration enabling field deployment in realistic operational environments, and straightforward setup facilitating frequent validation iterations during design refinement cycles.

The passive exoskeleton case study demonstrated that camera-derived stability metrics provide scientifically valid performance quantification. Correlation between LSD-based stability assessment and task duration improvements (57-729% across participants) established

the methodology's sensitivity to exoskeleton effectiveness. Subsequent EMG validation confirmed that camera-detected stability improvements correspond to physiological benefit through systematic muscle activation reductions (8.3-13.9% average), validating the approach's scientific rigor while preserving accessibility advantages.

Metabolic assessment through oxygen consumption measurement provides comprehensive quantification of physical demand reduction but requires specialized equipment and controlled laboratory conditions [107]. Optical motion capture systems combined with force plates represent the validation gold standard for detailed biomechanical characterization [125]. IMU-based validation offers portable kinematic assessment with moderate accuracy, enabling field deployment while maintaining cost-effectiveness [124]. Camera-based tracking occupies a unique position within this validation landscape: lower accuracy than professional systems but adequate for postural stability assessment, substantially lower cost enabling broader research access, and field deployment capability addressing ecological validity limitations of laboratory-restricted methodologies.

Conclusions

C.1 Research Objectives and Achievements

This thesis addressed fundamental limitations in upper limb rehabilitation robotics through integrated development of systematic design methodology and innovative technical solutions for coordinated multi-joint assistance. Three primary research objectives structured the investigation, each validated through experimental demonstration and quantitative performance assessment.

Objective 1 - Systematic Design Methodology: Development and validation of a structured framework integrating PDS, MCDM, mathematical modeling, and iterative validation protocols specifically adapted for rehabilitation exoskeleton development. The methodology was successfully applied to coordinated shoulder-elbow exoskeleton design (Chapter 3), demonstrating effectiveness in translating requirements into functional specifications, enabling quantitative alternative evaluation through explicit weighting criteria, and guiding systematic design space exploration. The framework addresses reproducibility challenges through documented decision processes, objective performance metrics, and traceable requirements flow from specifications to validated implementation.

Objective 2 - Coordinated Multi-Joint Exoskeleton: Design and experimental validation of a novel coordinated cable-driven system providing simultaneous 3-DoF assistance (shoulder flexion/extension, abduction/adduction, elbow flexion/extension) with preserved functional range of motion (0–90° across all DoF). The implemented prototype achieved 3.3 kg total system mass including battery, meeting portability requirements while enabling coordinated assistance. Human subject validation (n=5) demonstrated statistically significant muscle activation reduction (overall 18.4% average, medial deltoid 27.7% with p=0.012) while maintaining natural kinematic coordination patterns (R^2=0.64–0.82) during functional tasks including drinking, pick-and-place manipulation, and controlled range-of-motion exercises. These results establish clinical viability for endurance-based rehabilitation protocols supporting activities of daily living.

Objective 3 - Motor-Proximal Sensing Architecture: Development and validation of a novel force sensing configuration relocating load cells from cable anchor points to motor-proximal positions adjacent to actuation units. This architecture resolves the fundamental spatial interference constraint that limits traditional anchor-point configurations to single-joint operation in cable-driven systems. Comprehensive validation of the measurement samples spanning complete operational workspace established measurement accuracy (R^2=0.75 overall, RMSE=1.51 Nm) sufficient for real-time admittance control while enabling coordinated multi-joint assistance previously achievable only through rigid exoskeletons with substantially higher mass (7.5 kg versus 3.3 kg). Workspace-dependent accuracy analysis revealed optimal performance within 0–60° elevation range where 96% of functional activities occur, with acceptable degradation at extreme elevations (60–90°) where gravitational loads inherently diminish.

The three objectives were achieved through systematic integration documented across thesis chapters, demonstrating that structured methodology combined with enabling technical innovations can address fundamental constraints in rehabilitation robotics: multi-joint coordination supporting functional movement patterns, sensing precision across extended operational ranges, and practical deployment feasibility balancing assistance effectiveness with wearability requirements.

C.2 Scientific and Technical Contributions

The thesis delivers validated contributions advancing rehabilitation robotics across methodological, architectural, and technological dimensions.

Methodological Contribution: The systematic design framework (Chapter 2) provides reproducible guidance for rehabilitation exoskeleton development through explicit integration of Product Design Specifications defining quantitative acceptance criteria, Multi-Criteria Decision Making enabling objective alternative evaluation with traceable weighting justifications, mathematical modeling predicting performance across operational envelopes, and iterative validation protocols comparing measured versus predicted results. Application to coordinated shoulder-elbow exoskeleton development (Chapter 3) demonstrated methodology effectiveness in identifying optimal design solutions balancing functionality (3-DoF coordination), portability (3.3 kg system mass), and clinical viability (statistically significant muscle activation reduction). The framework extends beyond the specific case study, offering validated principles applicable to broader classes of wearable assistive devices through

adaptation of evaluation criteria, model fidelity, and validation depth to specific application contexts.

Architectural Contribution: The novel coordinated shoulder-elbow exosuit represents a lightweight (<4 kg) self-wearable cable-driven system providing simultaneous 3-DoF assistance with preserved functional workspace (0–90° all joints). The integrated architecture employs biomimetic dual-tendon shoulder actuation principles (validated by [108]) with coordinated elbow assistance methodology (demonstrated by [109]), extending established single-joint paradigms to multi-joint coordination through novel motor-proximal sensing enablement. This system-level innovation achieves coordinated assistance preventing compensatory loading patterns inherent in single-joint devices, where unassisted joints must compensate during functional tasks, potentially creating overuse injuries and maladaptive motor patterns. Experimental validation established clinically meaningful performance: 18.4% average muscle activation reduction with individual joint-specific effectiveness (medial deltoid 27.7%, biceps 18.2%) comparable to specialized single-DoF systems, preserved kinematic coordination (R^2=0.64–0.82) maintaining natural movement synergies, and joint range preservation (87–89° achieved versus 90° target across all DoF) demonstrating minimal kinematic constraint from cable-driven assistance.

Technological Contribution: The new motor-proximal sensing resolves a fundamental constraint in cable-driven soft exoskeletons through strategic load cell repositioning from anchor points to actuation unit locations. This enabling innovation makes coordinated 3-DoF cable-driven assistance feasible, representing a fundamental advancement rather than incremental improvement by resolving the RoM-accuracy trade-off that constrained cable-driven systems to single-joint operation. In multi-joint coordination scenarios, conventional anchor-point sensors create physical interference between distributed cables (typical 40–50 mm load cell housing reducing free cable length), constraining achievable range of motion particularly during combined shoulder-elbow movements. Motor-proximal configuration eliminates this spatial interference while maintaining force measurement accuracy through geometric compensation algorithms that translate motor-proximal pulley forces into effective anchor-point tensions accounting for configuration-dependent cable routing geometry. Comprehensive validation established measurement fidelity (R^2=0.75, RMSE=1.51 Nm) sufficient for real-time admittance control, with workspace-dependent characteristics aligned with natural task distribution (96% of measurements within 0–60° elevation where accuracy remains optimal). This enabling technology makes coordinated 3-DoF cable-driven assistance feasible, representing a fundamental advancement rather than incremental improvement by

resolving the ROM-accuracy trade-off that constrained cable-driven systems to single-joint operation or reduced functional workspace.

These contributions collectively advance rehabilitation robotics by demonstrating systematic methodology integration with technical innovations addressing coordination, sensing precision, and deployment feasibility constraints, establishing validated principles extensible to broader assistive technology applications.

C.3 Clinical and Translational Implications

The demonstrated system performance establishes specific clinical applications and translational pathways warranting further investigation.

Target Patient Populations: The coordinated 3-DoF assistance with preserved functional workspace addresses rehabilitation needs for individuals with moderate upper limb impairment affecting activities of daily living, particularly stroke survivors (77–85% experience upper limb dysfunction) and individuals with neurological, musculoskeletal, or age-related conditions retaining voluntary movement but requiring gravitational compensation. The particularly effective shoulder abduction assistance (medial deltoid 27.7% reduction, $p=0.012$) combined with coordinated elbow support provides optimal configuration for sustained upper limb training during functional rehabilitation protocols. The system's portable architecture (3.3 kg, battery-powered, self-wearable) enables potential home-based rehabilitation scenarios extending therapy beyond clinical facilities, addressing scalability constraints in conventional manual therapy approaches.

Therapeutic Applications: The coordinated assistance paradigm preventing compensatory loading patterns addresses fundamental limitations of single-joint devices that can create overuse injuries in unassisted joints during functional tasks. Preserved kinematic coordination ($R^2=0.64–0.82$) maintains natural movement synergies essential for motor learning and functional recovery, distinguishing the approach from isolated joint training that may reinforce maladaptive compensation strategies. The demonstrated 18.4% average muscle activation reduction provides clinically meaningful assistance levels for endurance-based rehabilitation interventions, enabling extended training durations supporting neuroplastic adaptation mechanisms underlying functional recovery. Workspace-dependent sensing accuracy characteristics (optimal performance 0–60° elevation covering 85–90% of ADL movements) align well with functional training emphasis on mid-range reaching, manipulation, and self-care activities constituting primary rehabilitation objectives.

Translational Requirements: The proof-of-concept validation with healthy subjects (n=5), while establishing baseline system performance and technical feasibility, necessitates subsequent expanded cohort studies with target patient populations for clinical efficacy validation. Required investigations include: controlled trials with stroke patients comparing coordinated assistance versus conventional therapy or single-joint devices (primary outcome: functional independence measures; secondary outcomes: muscle activation patterns, kinematic quality, training duration tolerance), long-term studies assessing motor learning transfer and retention following coordinated training protocols (follow-up assessments: ADL performance, compensatory movement patterns, functional workspace utilization), and usability assessments in home-based rehabilitation scenarios evaluating self-donning capability, system reliability during extended use, and user acceptance across diverse anthropometric and functional ability ranges. The restricted initial sample size (n=5) and homogeneous demographics (healthy males, age 29±5 years) constrain immediate generalizability, requiring systematic expansion to broader populations including varied ages, genders, anthropometric ranges, and impairment severities.

Implementation Pathways: Clinical deployment strategies should emphasize mid-range functional training (0–60° elevation) where sensing accuracy is optimal and natural task distribution is concentrated, with conservative assistance gain tuning (reduced from nominal 70% to 50–60%) for protocols requiring sustained high-elevation postures. The systematic design methodology provides framework for adaptation to specific patient populations through anthropometric scaling, assistance gain personalization, and task-specific training protocols guided by individual functional requirements. Regulatory considerations for clinical translation include medical device classification, safety validation protocols, and demonstration of therapeutic equivalence or superiority versus established rehabilitation approaches through controlled clinical trials meeting regulatory standards.

C.4 Future Research Directions

Several promising research directions emerge from thesis contributions, extending validated principles toward broader rehabilitation applications and enhanced clinical effectiveness.

Multi-Joint Coordination Enhancement: Current implementation provides coordinated assistance across shoulder and elbow with preserved functional workspace, establishing foundation for extension to additional degrees of freedom including wrist movements and forearm rotation. Integration of wrist assistance requires addressing increased kinematic complexity, distributed actuation routing through multiple joints, and coordinated control strategies

maintaining natural synergies across expanded DoF. Potential approaches include additional cable routing paths for wrist flexion/extension and pronation/supination, hybrid actuation combining cable-driven proximal assistance with compact distal actuators, and hierarchical control architectures coordinating assistance distribution across primary (shoulder/elbow) and secondary (wrist) joints based on task requirements and user intent signals.

Adaptive Control Strategies: The current admittance control implementation provides gravity compensation with empirically tuned damping parameters, offering opportunities for enhanced personalization through adaptive algorithms learning individual user characteristics, movement patterns, and assistance preferences. Machine learning approaches could optimize assistance gains based on real-time performance metrics (muscle activation levels, movement smoothness, task completion efficiency), adapt control parameters throughout rehabilitation progression as functional capacity improves, and implement subject-specific biomechanical models accounting for individual anthropometry, impairment characteristics, and residual motor capabilities. Integration with clinical assessment tools would enable objective tracking of rehabilitation progress and data-driven adjustment of therapeutic protocols.

Sensing Architecture Refinement: The motor-proximal sensing validation revealed workspace-dependent accuracy characteristics with degradation at elevated angles (60–90°) due to reduced moment arms and diminishing gravitational torques. Future iterations could address this through adaptive transmission efficiency models accounting for configuration-dependent Bowden conduit friction, hybrid sensing strategies combining motor-proximal load cells with distributed strain sensors on cable segments providing complementary measurements, or machine learning compensation algorithms trained on individual user calibration data. However, clinical relevance depends on target applications: for ADL-focused rehabilitation where 85–90% of movements occur within 0–60° elevation, current performance aligns well with functional requirements, while overhead task training may warrant enhanced elevated-angle accuracy.

Clinical Validation Expansion: Rigorous clinical efficacy assessment requires controlled trials with neurological patient populations comparing coordinated assistance versus conventional therapy and single-joint devices. Recommended study designs include: randomized controlled trials with stroke patients (minimum n=30 per group) measuring functional independence (primary outcome: Fugl-Meyer Assessment, Action Research Arm Test), kinematic quality (movement smoothness, compensatory patterns), and training efficiency (session duration tolerance, perceived exertion); longitudinal studies tracking motor learning transfer and retention following coordinated training (6-month follow-up assessments); and comparative effectiveness research versus established rehabilitation robotics platforms (e.g., Armeo,

InMotion) establishing therapeutic equivalence or superiority. Systematic expansion across diverse patient populations (varied impairment severities, etiologies, ages) would establish broader clinical applicability and identify optimal use cases for coordinated assistance paradigm.

Methodology Extension and Validation: The systematic design framework demonstrated effectiveness for cable-driven upper limb exoskeletons, warranting validation across broader device classes including lower limb exoskeletons, passive assistance devices, and hybrid actuation systems. Extension to different rehabilitation domains (gait training, balance support, hand function) would establish methodology generalizability and identify domain-specific adaptations. Longitudinal tracking of design iterations across multiple development cycles would quantify methodology impact on development time, prototype iterations required, and final performance compared to ad-hoc approaches. Integration with digital twins and simulation environments could enhance predictive accuracy during preliminary design phases, reducing physical prototyping requirements.

These research directions build upon validated thesis contributions, offering pathways toward enhanced clinical effectiveness, broader patient population applicability, and systematic advancement of rehabilitation robotics through continued integration of rigorous methodology with innovative technical solutions.

References

[1] L. M. Weber and J. Stein, "The use of robots in stroke rehabilitation: A narrative review," *NeuroRehabilitation*, vol. 43, no. 1, pp. 99–110, 2018.

[2] J. C. MacDermid, J. Ramos, D. Drosdowech, K. Faber, and S. Patterson, "The impact of rotator cuff pathology on isometric and isokinetic strength, function, and quality of life," *Journal of Shoulder and Elbow Surgery*, vol. 13, no. 6, pp. 593–598, 2004.

[3] R. Gassert and V. Dietz, "Rehabilitation robots for the treatment of sensorimotor deficits: a neurophysiological perspective," *Journal of Neuroengineering and Rehabilitation*, vol. 15, pp. 1–15, 2018.

[4] R. Bertani, C. Melegari, M. C. De Cola, A. Bramanti, P. Bramanti, and R. S. Calabro, "Effects of robot-assisted upper limb rehabilitation in stroke patients: a systematic review with meta-analysis," *Neurological Sciences*, vol. 38, pp. 1561–1569, 2017.

[5] J. Laut, M. Porfiri, and P. Raghavan, "The present and future of robotic technology in rehabilitation," *Current Physical Medicine and Rehabilitation Reports*, vol. 4, pp. 312–319, 2016.

[6] N. Rehmat, J. Zuo, W. Meng, Q. Liu, S. Q. Xie, and H. Liang, "Upper limb rehabilitation using robotic exoskeleton systems: A systematic review," *International Journal of Intelligent Robotics and Applications*, vol. 2, no. 3, pp. 283–295, 2018.

[7] M. Xiloyannis, D. Chiaradia, A. Frisoli, and L. Masia, "Physiological and kinematic effects of a soft exosuit on arm movements," *Journal of NeuroEngineering and Rehabilitation*, vol. 16, pp. 1–15, feb 2019.

[8] F. Molteni, G. Gasperini, G. Cannaviello, and E. Guanziroli, "Exoskeleton and end-effector robots for upper and lower limbs rehabilitation: narrative review," *PM&R*, vol. 10, no. 9, pp. S174–S188, 2018.

[9] M. Xiloyannis, R. Alicea, A.-M. Georgarakis, F. L. Haufe, P. Wolf, L. Masia, and R. Riener, "Soft robotic suits: State of the art, core technologies, and open challenges," *IEEE Transactions on Robotics*, pp. 1–20, 2021.

[10] H. Veeger and F. Van Der Helm, "Shoulder function: the perfect compromise between mobility and stability," *Journal of Biomechanics*, vol. 40, no. 10, pp. 2119–2129, 2007.

[11] W. Bakhsh and G. Nicandri, "Anatomy and Physical Examination of the Shoulder," sep 2018.

[12] A. M. Oosterwijk, M. K. Nieuwenhuis, C. P. van der Schans, and L. J. Mouton, "Shoulder and elbow range of motion for the performance of activities of daily living: A systematic review," jul 2018.

[13] S. A. Taylor, A. E. Kedgley, A. Humphries, and A. F. Shaheen, "Simulated activities of daily living do not replicate functional upper limb movement or reduce movement variability," *Journal of Biomechanics*, vol. 76, pp. 119–128, 2018.

[14] J. M. Soucie, C. Wang, A. Forsyth, S. Funk, M. Denny, K. E. Roach, and D. Boone, "Range of motion measurements: reference values and a database for comparison studies.," *Haemophilia : the official journal of the World Federation of Hemophilia*, vol. 17, pp. 500–507, may 2011.

[15] I. Gûnal, N. Köse, O. Erdogan, E. Göktürk, and S. Seber, "Normal range of motion of the joints of the upper extremity in male subjects, with special reference to side.," *The Journal of bone and joint surgery. American volume*, vol. 78, pp. 1401–1404, sep 1996.

[16] B. J. Majors and J. S. Wayne, "Development and validation of a computational model for investigation of wrist biomechanics," *Annals of Biomedical Engineering*, vol. 39, no. 11, pp. 2807–2815, 2011.

[17] H. Hallaceli and I. Gunal, "Normal range of scapular elevation and depression in healthy subjects," *Archives of Orthopaedic and Trauma Surgery*, vol. 122, no. 2, pp. 99–101, 2002.

[18] S. Nadeau, P. Gobeil, S. de Serres, and J. Landry, "Active movement measurements of the shoulder girdle in healthy subjects with goniometer and tape measure techniques: a study on reliability and validity," *Physiotherapy Theory and Practice*, vol. 23, no. 3, pp. 179–187, 2007.

[19] M. Doğan, M. Koçak, Ö. Onursal Kılınç, F. Ayvat, G. Sütçü, E. Ayvat, M. Kılınç, Ö. Ünver, and S. Aksu Yıldırım, "Functional range of motion in the upper extremity and trunk joints: Nine functional everyday tasks with inertial sensors," *Gait and Posture*, vol. 70, pp. 141–147, 2019.

[20] K. I. Norton, "Standards for Anthropometry Assessment," in *Kinanthropometry and Exercise Physiology*, pp. 68–137, Routledge, jun 2018.

[21] G. Mall, M. Hubig, A. Büttner, J. Kuznik, R. Penning, and M. Graw, "Sex determination and estimation of stature from the long bones of the arm," *Forensic Science International*, vol. 117, no. 1-2, pp. 23–30, 2001.

[22] M. Perrelli, F. Lago, S. Garofalo, L. Bruno, D. Mundo, and G. Carbone, "A critical review and systematic design approach for innovative upper-limb rehabilitation devices," *Robotics and Autonomous Systems*, vol. 183, p. 104835, 2025.

[23] E. Trigili, L. Grazi, S. Crea, A. Accogli, J. Carpaneto, S. Micera, and N. Vitiello, "Detection of movement onset using emg signals for upper-limb exoskeletons in reaching tasks," *Journal of NeuroEngineering and Rehabilitation*, vol. 16, p. 45, 2019.

[24] G. A. Pratt and M. M. Williamson, "Series elastic actuators," *Proceedings 1995 IEEE/RSJ International Conference on Intelligent Robots and Systems*, vol. 1, pp. 399–406, 1995.

[25] D. Verdel, S. Bastide, N. Vignais, O. Bruneau, and B. Berret, "An identification-based method improving the transparency of a robotic upper limb exoskeleton," *Robotica*, vol. 39, no. 9, pp. 1711–1728, 2021.

[26] M. W. Spong, S. Hutchinson, and M. Vidyasagar, *Robot Modeling and Control*. Hoboken, NJ, USA: John Wiley & Sons, 2 ed., 2020.

[27] B. Siciliano, L. Sciavicco, L. Villani, and G. Oriolo, *Robotics: Modelling, Planning and Control*. London, UK: Springer, 2009.

[28] "Robots and robotic devices – safety requirements for personal care robots," ISO Standard 13482:2014, International Organization for Standardization, 2014.

[29] S. Hussain, S. Q. Xie, and P. K. Jamwal, "Adaptive impedance control of a robotic orthosis for gait rehabilitation," *IEEE Transactions on Cybernetics*, vol. 43, no. 3, pp. 1025–1034, 2017.

[30] N. Hogan, "Impedance control: An approach to manipulation: Part i—theory," *Journal of Dynamic Systems, Measurement, and Control*, vol. 107, no. 1, pp. 1–7, 1985.

[31] L. Marchal-Crespo and D. J. Reinkensmeyer, "Review of control strategies for robotic movement training after neurologic injury," *Journal of NeuroEngineering and Rehabilitation*, vol. 6, no. 20, 2009.

[32] K. R. S. Holzbaur, W. M. Murray, and S. L. Delp, "A model of the upper extremity for simulating musculoskeletal surgery and analyzing neuromuscular control," *Annals of Biomedical Engineering*, vol. 33, no. 6, pp. 829–840, 2005.

[33] H. I. Krebs, N. Hogan, M. L. Aisen, and B. T. Volpe, "Robot-aided neurorehabilitation," *IEEE Transactions on Rehabilitation Engineering*, vol. 6, no. 1, pp. 75–87, 2003.

[34] G. Salazar and M. N. Russi-Vigoya, "Technology Readiness Level (TRL) as the foundation of Human Readiness Level (HRL)," *Ergonomics in Design: The Quarterly of Human Factors Applications*, 2021. NASA Technical Report Server (NTRS) Citation: 20210000183.

[35] F. Stella, M. Severino, M. Manetti, and N. Nencini, "Rehabilitation, assistive devices and home tele-rehabilitation for the elderly: Where we are and what are the perspectives," *Journal of Clinical Medicine*, vol. 11, no. 17, p. 5069, 2022.

[36] N. F. Rojo, I. Nazari, C. Applegate, M. Lee, J. Carley, and Y. Sun, "A Wearable Soft Exoskeleton for Shoulder Motion Assistance," in *Proceedings - 2022 IEEE/ACM International Conference on Connected Health: Applications, Systems and Engineering Technologies, CHASE 2022*, pp. 162–163, ACM, 2022.

[37] A.-M. Georgarakis, M. Xiloyannis, P. Wolf, and R. Riener, "A textile exomuscle that assists the shoulder during functional movements for everyday life," *Nature Machine Intelligence*, vol. 4, no. 6, pp. 574–582, 2022.

[38] R. F. Natividad and C. H. Yeow, "Development of a soft robotic shoulder assistive device for shoulder abduction," in *Proceedings of the IEEE RAS and EMBS International Conference on Biomedical Robotics and Biomechatronics*, vol. 2016-July, pp. 989–993, IEEE Computer Society, jul 2016.

[39] J. F. Rodríguez-León, B. D. M. Chaparro-Rico, D. Cafolla, F. Lago, E. Castillo-Castañeda, and G. Carbone, "Design of a Novel Exoskeleton with Passive Magnetic Spring Self-locking and Spine Lateral Balancing," *Journal of Bionic Engineering*, 2023.

[40] Y. G. Kim, K. Little, B. Noronha, M. Xiloyannis, L. Masia, and D. Accoto, "A voice activated bi-articular exosuit for upper limb assistance during lifting tasks," *Robotics and Computer-Integrated Manufacturing*, vol. 66, 2020.

[41] S. J. Park, K. Choi, H. Rodrigue, and C. H. Park, "Fabric muscle with a cooling acceleration structure for upper limb assistance soft exosuits," *Scientific Reports*, vol. 12, pp. 1–13, jul 2022.

[42] R. Sambhav, S. Jena, A. Chatterjee, S. Bhasin, S. Santapuri, L. Kumar, S. P. Muthukrishnan, and S. Roy, "An Integrated Dynamic Closed Loop Simulation Platform for Elbow Flexion Augmentation Using an Upper Limb Exosuit Model," *Frontiers in Robotics and AI*, vol. 9, p. 768841, mar 2022.

[43] D. Copaci, E. Cano, L. Moreno, and D. Blanco, "New Design of a Soft Robotics Wearable Elbow Exoskeleton Based on Shape Memory Alloy Wire Actuators," *Applied Bionics and Biomechanics*, vol. 2017, 2017.

[44] J. Nassour, G. Zhao, and M. Grimmer, "Soft pneumatic elbow exoskeleton reduces the muscle activity, metabolic cost and fatigue during holding and carrying of loads," *Scientific Reports*, vol. 11, no. 1, p. 12556, 2021.

[45] M. Irshaidat, M. Soufian, A. Al-Ibadi, and S. Nefti-Meziani, "A novel elbow pneumatic muscle actuator for exoskeleton arm in post-stroke rehabilitation," in *RoboSoft 2019 - 2019 IEEE International Conference on Soft Robotics*, pp. 630–635, Institute of Electrical and Electronics Engineers Inc., may 2019.

[46] M. Xiloyannis, E. Annese, M. Canesi, A. Kodiyan, A. Bicchi, S. Micera, A. Ajoudani, and L. Masia, "Design and validation of a modular one-to-many actuator for a soft wearable exosuit," *Frontiers in Neurorobotics*, vol. 13, p. 456109, jun 2019.

[47] R. S. Diteesawat, S. Hoh, E. Pulvirenti, N. Rahman, L. Morris, A. Turton, M. Cramp, and J. Rossiter, "A Soft Fabric-based Shrink-to-fit Pneumatic Sleeve for Comfortable Limb Assistance," in *IEEE International Conference on Intelligent Robots and Systems*, vol. 2022-Octob, pp. 9766–9773, 2022.

[48] S. J. Park and C. H. Park, "Suit-type Wearable Robot Powered by Shape-memory-alloy-based Fabric Muscle," *Scientific Reports*, vol. 9, no. 1, 2019.

[49] M. M. Salvatore, M. Ceccarelli, D. Pisla, M. Sofan, and G. Carbone, "Design and validation of a hybrid upper-limb assistive exoskeleton for repetitive lifting tasks," *International Journal of Mechanics and Control*, vol. 24, no. 1, pp. 215–226, 2023.

[50] D. Xie, Z. Ma, J. Liu, and S. Zuo, "Pneumatic Artificial Muscle Based on Novel Winding Method," *Actuators*, vol. 10, may 2021.

[51] C. Lambelet, M. Lyu, D. Woolley, R. Gassert, and N. Wenderoth, "The eWrist - A wearable wrist exoskeleton with sEMG-based force control for stroke rehabilitation," in *IEEE International Conference on Rehabilitation Robotics*, pp. 726–733, 2017.

[52] H. Su, K. S. Lee, Y. Kim, and H. S. Park, "A Soft, Wearable Skin-Brace for Assisting Forearm Pronation and Supination With a Low-Profile Design," *IEEE Robotics and Automation Letters*, vol. 7, pp. 12078–12085, oct 2022.

[53] R. F. Natividad, T. Miller-Jackson, and R. Y. Chen-Hua, "A 2-DOF Shoulder Exosuit Driven by Modular, Pneumatic, Fabric Actuators," *IEEE Transactions on Medical Robotics and Bionics*, vol. 3, no. 1, pp. 166–178, 2021.

[54] J. L. Samper-Escudero, A. Gimenez-Fernandez, M. A. Sanchez-Uran, and M. Ferre, "A Cable-Driven Exosuit for Upper Limb Flexion Based on Fibres Compliance," *IEEE Access*, vol. 8, pp. 153297–153310, 2020.

[55] T. Proietti, C. O'neill, C. J. Hohimer, K. Nuckols, M. E. Clarke, Y. M. Zhou, D. J. Lin, and C. J. Walsh, "Sensing and Control of a Multi-Joint Soft Wearable Robot for Upper-Limb Assistance and Rehabilitation," *IEEE ROBOTICS AND AUTOMATION LETTERS*, vol. 6, no. 2, 2021.

[56] A. Golgouneh, E. Beaudette, H. Woelfle, B. Li, N. Subash, A. Redhouse, M. Jones, T. Martin, M. Lobo, B. Holschuh, and L. Dunne, "Design of a Hybrid SMA-Pneumatic based Wearable Upper Limb Exoskeleton," in *Proceedings - International Symposium on Wearable Computers, ISWC*, pp. 179–183, Association for Computing Machinery, sep 2020.

[57] T. Chen, R. Casas, and P. S. Lum, "An Elbow Exoskeleton for Upper Limb Rehabilitation with Series Elastic Actuator and Cable-Driven Differential," *IEEE Transactions on Robotics*, vol. 35, no. 6, pp. 1464–1474, 2019.

[58] M. A. Laribi and M. Ceccarelli, "Design and experimental characterization of a cable-driven elbow assisting device," *Journal of Medical Devices, Transactions of the ASME*, vol. 15, mar 2021.

[59] N. Li, T. Yang, Y. Yang, P. Yu, X. Xue, X. Zhao, G. Song, I. H. Elhajj, W. Wang, N. Xi, and L. Liu, "Bioinspired Musculoskeletal Model-based Soft Wrist Exoskeleton for Stroke Rehabilitation," *Journal of Bionic Engineering*, vol. 17, pp. 1163–1174, nov 2020.

[60] H. Choi, B. B. Kang, B. K. Jung, and K. J. Cho, "Exo-Wrist: A Soft Tendon-Driven Wrist-Wearable Robot with Active Anchor for Dart-Throwing Motion in Hemiplegic Patients," *IEEE Robotics and Automation Letters*, vol. 4, pp. 4499–4506, oct 2019.

[61] J. Jeong, I. B. Yasir, J. Han, C. H. Park, S. K. Bok, and K. U. Kyung, "Design of shape memory alloy-based soft wearable robot for assistingwrist motion," *Applied Sciences (Switzerland)*, vol. 9, p. 4025, sep 2019.

[62] C. Greco, T. H. Weerakkody, V. Cichella, L. Pagnotta, and C. Lamuta, "Lightweight Bioinspired Exoskeleton for Wrist Rehabilitation Powered by Twisted and Coiled Artificial Muscles," *Robotics*, vol. 12, p. 27, feb 2023.

[63] S. Liu, Z. Fang, J. Liu, K. Tang, J. Luo, J. Yi, X. Hu, and Z. Wang, "A Compact Soft Robotic Wrist Brace With Origami Actuators," *Frontiers in Robotics and AI*, vol. 8, p. 614623, mar 2021.

[64] B. W. Ang and C. H. Yeow, "Design and characterization of a 3d printed soft robotic wrist sleeve with 2 DoF for stroke rehabilitation," in *RoboSoft 2019 - 2019 IEEE International Conference on Soft Robotics*, pp. 577–582, Institute of Electrical and Electronics Engineers Inc., may 2019.

[65] D. Serrano, D. S. Copaci, L. Moreno, and D. Blanco, "SMA based wrist exoskeleton for rehabilitation therapy," in *IEEE International Conference on Intelligent Robots and Systems*, pp. 2318–2323, Institute of Electrical and Electronics Engineers Inc., dec 2018.

[66] T. Higuma, K. Kiguchi, and J. Arata, "Low-Profile Two-Degree-of-Freedom Wrist Exoskeleton Device Using Multiple Spring Blades," *IEEE Robotics and Automation Letters*, vol. 3, pp. 305–311, jan 2018.

[67] S. Christensen and S. Bai, "Kinematic analysis and design of a novel shoulder exoskeleton using a double parallelogram linkage," *Journal of Mechanisms and Robotics*, vol. 10, aug 2018.

[68] S. Lessard, P. Pansodtee, A. Robbins, J. M. Trombadore, S. Kurniawan, and M. Teodorescu, "A Soft Exosuit for Flexible Upper-Extremity Rehabilitation," *IEEE Transactions on Neural Systems and Rehabilitation Engineering*, vol. 26, pp. 1604–1617, aug 2018.

[69] A. Ebrahimi, "Stuttgart Exo-Jacket: An exoskeleton for industrial upper body applications," in *Proceedings - 2017 10th International Conference on Human System Interactions, HSI 2017*, pp. 258–263, Institute of Electrical and Electronics Engineers Inc., aug 2017.

[70] A. U. Pehlivan, F. Sergi, A. Erwin, N. Yozbatiran, G. E. Francisco, and M. K. O'Malley, "Design and validation of the RiceWrist-S exoskeleton for robotic rehabilitation after incomplete spinal cord injury," *Robotica*, vol. 32, no. 8, pp. 1415–1431, 2014.

[71] J. Huang, W. Huo, W. Xu, S. Mohammed, and Y. Amirat, "Control of Upper-Limb Power-Assist Exoskeleton Using a Human-Robot Interface Based on Motion Intention Recognition," *IEEE Transactions on Automation Science and Engineering*, vol. 12, pp. 1257–1270, oct 2015.

[72] J. L. Samper-Escudero, S. Coloma, M. A. Olivares-Mendez, M. A. S. U. Gonzalez, and M. Ferre, "A Compact and Portable Exoskeleton for Shoulder and Elbow Assistance for Workers and Prospective Use in Space," *IEEE Transactions on Human-Machine Systems*, vol. 53, pp. 668–677, aug 2023.

[73] I. Gaponov, D. Popov, S. J. Lee, and J. H. Ryu, "Auxilio: A portable cable-driven exosuit for upper extremity assistance," *International Journal of Control, Automation and Systems*, vol. 15, pp. 73–84, feb 2017.

[74] X. Chen, S. Zhang, K. Cao, C. Wei, W. Zhao, and J. Yao, "Development of a Wearable Upper Limb Rehabilitation Robot Based on Reinforced Soft Pneumatic Actuators," *Chinese Journal of Mechanical Engineering (English Edition)*, vol. 35, pp. 1–9, dec 2022.

[75] J. Ma, D. Chen, Z. Liu, and M. Wang, "A Soft Wearable Exoskeleton with Pneumatic Actuator for Assisting Upper Limb," in *2020 IEEE International Conference on Real-Time Computing and Robotics, RCAR 2020*, pp. 99–104, Institute of Electrical and Electronics Engineers Inc., sep 2020.

[76] T. Y. Tsai, C. Y. Chang, M. T. Chung, K. C. Lu, J. F. Huang, and W. P. Shih, "A portable exoskeleton driven by pneumatic artificial muscles for upper limb motion replication," in *ACM International Conference Proceeding Series*, pp. 133–138, 2018.

[77] T. P. Valayil and R. S. Augustine, "Kinematics and workspace analysis of a robotic device for performing rehabilitation therapy of upper limb in stroke-affected patients," *Acta of Bioengineering and Biomechanics*, vol. 23, no. 3, pp. 175–189, 2021.

[78] M. H. Rahman, M. J. Rahman, O. L. Cristobal, M. Saad, J. P. Kenné, and P. S. Archambault, "Development of a whole arm wearable robotic exoskeleton for rehabilitation and to assist upper limb movements," *Robotica*, vol. 33, pp. 19–39, jan 2015.

[79] N. Li, T. Yang, P. Yu, J. Chang, L. Zhao, X. Zhao, I. H. Elhajj, N. Xi, and L. Liu, "Bio-inspired upper limb soft exoskeleton to reduce stroke-induced complications," *Bioinspiration and Biomimetics*, vol. 13, p. 066001, aug 2018.

[80] J. B. Hidler and A. E. Wall, "Alterations in muscle activation patterns during robotic-assisted walking," *Clinical Biomechanics*, vol. 20, no. 2, pp. 184–193, 2005.

[81] L. Gerez, S. Micera, R. Nuckols, and T. Proietti, "Assessment of wearable robotics performance in patients with neurological conditions," *Current Opinion in Neurology*, vol. 37, no. 6, pp. 645–654, 2024.

[82] W. Wang, J. Zhang, X. Wang, A. Yuan, and P. Zhang, "Motion intensity modeling and trajectory control of upper limb rehabilitation exoskeleton robot based on multi-modal information," *Complex & Intelligent Systems*, vol. 8, pp. 1763–1775, 2022.

[83] A. Gasparetto, Y. Takeda, and G. Rosati, "Editorial of the special issue: Innovative robot design for special applications," *Robotica*, vol. 42, no. 6, pp. 1712–1714, 2024.

[84] G. Pahl, W. Beitz, J. Feldhusen, and K.-H. Grote, *Engineering Design: A Systematic Approach*. Springer-Verlag London, 3rd ed., 2007.

[85] N. Cross, *Engineering Design Methods: Strategies for Product Design*. John Wiley & Sons, 4th ed., 2008.

[86] E. Reutskaja, A. Lindner, R. Nagel, R. A. Andersen, and C. F. Camerer, "Choice overload: A conceptual review and meta-analysis," *Journal of Consumer Psychology*, vol. 28, no. 3, pp. 333–358, 2018.

[87] K. T. Ulrich and S. D. Eppinger, *Product Design and Development*. McGraw-Hill Education, 6th ed., 2015.

[88] NASA, "NASA Systems Engineering Handbook," Tech. Rep. NASA/SP-2007-6105 Rev1, National Aeronautics and Space Administration, Washington, DC, 2007.

[89] E. Hull, K. Jackson, and J. Dick, *Requirements Engineering*. Springer, 3rd ed., 2011.

[90] E. Triantaphyllou, *Multi-criteria Decision Making Methods: A Comparative Study*. Boston, MA: Springer, 2000.

[91] C.-L. Hwang and K. Yoon, *Multiple Attribute Decision Making: Methods and Applications*. Berlin, Germany: Springer-Verlag, 1981.

[92] T. L. Saaty, *The Analytic Hierarchy Process*. New York: McGraw-Hill, 1980.

[93] E. K. Zavadskas, Z. Turskis, and S. Kildienė, "Multiple criteria decision making (mcdm) methods in economics: an overview," *Technological and Economic Development of Economy*, vol. 17, no. 2, pp. 397–427, 2014.

[94] E. J. Haug, *Computer Aided Kinematics and Dynamics of Mechanical Systems*, vol. 1. Boston: Allyn and Bacon, 1989.

[95] A. A. Shabana, *Dynamics of Multibody Systems*. Cambridge, UK: Cambridge University Press, 4th ed., 2013.

[96] D. A. Winter, *Biomechanics and Motor Control of Human Movement*. Hoboken, NJ: John Wiley Sons, 4th ed., 2009.

[97] G. Boothroyd, P. Dewhurst, and W. A. Knight, *Product Design for Manufacture and Assembly*. Boca Raton, FL: CRC Press/Taylor & Francis, 3rd ed., 2010.

[98] M. F. Ashby, *Materials Selection in Mechanical Design*. Oxford, UK: Butterworth-Heinemann/Elsevier, 4th ed., 2011.

[99] L. Marchal-Crespo and D. J. Reinkensmeyer, "Review of control strategies for robotic movement training after neurologic injury," *Journal of NeuroEngineering and Rehabilitation*, vol. 6, no. 20, pp. 1–15, 2009.

[100] E. T. Wolbrecht, V. Chan, D. J. Reinkensmeyer, and J. E. Bobrow, "Optimizing compliant, model-based robotic assistance to promote neurorehabilitation," *IEEE Transactions on Neural Systems and Rehabilitation Engineering*, vol. 16, no. 3, pp. 286–297, 2008.

[101] SENIAM Project, "SENIAM: Surface ElectroMyoGraphy for the Non-Invasive Assessment of Muscles." http://www.seniam.org, 1999.

[102] N. Vitiello, T. Lenzi, S. Roccella, S. M. M. De Rossi, E. Cattin, F. Giovacchini, F. Vecchi, and M. C. Carrozza, "Neuroexos: A powered elbow exoskeleton for physical rehabilitation," *IEEE Transactions on Robotics*, vol. 29, no. 1, pp. 220–235, 2013.

[103] International Organization for Standardization, "Iso 14971: Medical devices—application of risk management to medical devices," 2019.

[104] R. Bostelman, E. Messina, and S. Foufou, "Astm f48 formation and standards for industrial exoskeletons and exosuits," *IISE Transactions on Occupational Ergonomics and Human Factors*, vol. 7, no. 3-4, pp. 230–236, 2019.

[105] International Organization for Standardization, "Iso 9283: Manipulating industrial robots—performance criteria and related test methods," 1998.

[106] R. Bostelman and T. Hong, "Test methods for exoskeletons: Lessons learned from industrial and response robotics," in *Wearable Exoskeleton Systems: Design, Control and Applications*, pp. 335–361, IET, 2018.

[107] K. Huysamen, M. de Looze, T. Bosch, J. Ortiz, S. Toxiri, and L. W. O'Sullivan, "Evaluation of a passive exoskeleton for static upper limb activities," *Applied Ergonomics*, vol. 70, pp. 148–155, 2018.

[108] F. Missiroli, A. Ciaramella, L. Radaelli, E. Rambaldi, A. Frisoli, M. Casadio, and L. Masia, "Reconfigurable soft exoskeleton for shoulder support using tendon-driven underactuation," *IEEE Transactions on Medical Robotics and Bionics*, pp. 1–1, 2025.

[109] N. Lotti, M. Xiloyannis, F. Missiroli, C. Bokranz, D. Chiaradia, A. Frisoli, R. Riener, and L. Masia, "Myoelectric or force control? a comparative study on a soft arm exosuit," *IEEE Transactions on Robotics*, vol. 38, no. 3, pp. 1363–1379, 2022.

[110] T. Chen, R. Casas, and P. S. Lum, "An elbow exoskeleton for upper limb rehabilitation with series elastic actuator and cable-driven differential," *IEEE Transactions on Robotics*, vol. 35, no. 6, pp. 1464–1474, 2019.

[111] J. Rosen and J. C. Perry, "Upper limb powered exoskeleton," *International Journal of Humanoid Robotics*, vol. 4, no. 03, pp. 529–548, 2007.

[112] S. G. Hart and L. E. Staveland, "Development of NASA-TLX (Task Load Index): Results of Empirical and Theoretical Research," technical report, NASA Ames Research Center, 1988. In P.A. Hancock and N. Meshkati (Eds.), Human Mental Workload, pp. 139-183. Amsterdam: North-Holland.

[113] G. Palli, G. Borghesan, and C. Melchiorri, "Modeling, identification, and control of tendon-based actuation systems," *IEEE Transactions on Robotics*, vol. 28, no. 2, pp. 277–290, 2012.

[114] M. A. Murphy, C. Willén, and K. S. Sunnerhagen, "Kinematic Variables Quantifying Upper-Extremity Performance After Stroke During Reaching and Drinking From a Glass," *Neurorehabilitation and Neural Repair*, vol. 20, pp. 444–453, December 2006.

[115] A. Murgia, P. J. Kyberd, P. H. Chappell, and C. M. Light, "Marker Placement to Describe the Wrist Movements During Activities of Daily Living in Cyclical Tasks," *Clinical Biomechanics*, vol. 19, pp. 248–254, March 2004.

[116] F. Lago, S. Leone, E. Curcio, and G. Carbone, "Challenges in designing and adopting robotic rehabilitation systems," vol. 180, 2025.

[117] J. F. Rodríguez-León, B. D. Chaparro-Rico, D. Cafolla, F. Lago, E. Castillo-Castañeda, and G. Carbone, "Design of a novel exoskeleton with passive magnetic spring self-locking and spine lateral balancing," *Journal of Bionic Engineering*, vol. 21, no. 1, pp. 236–255, 2024.

[118] Ç. Arslan and A. Tiemessen, "Adaptive bézier degree reduction and splitting for computationally efficient motion planning," *IEEE Transactions on Robotics*, vol. 38, no. 6, pp. 3655–3674, 2022.

[119] S. Mänttäri, A. P. Rauttola, J. Halonen, J. Karkulehto, P. Säynäjäkangas, and J. Oksa, "Effects of upper-limb exoskeleton on muscle activity in tasks requiring arm elevation: Part ii–in-field experiments in construction industry settings," *Work*, vol. 77, no. 3, pp. 1023–1035, 2024.

[120] S. P. Arjunan, D. K. Kumar, K. Wheeler, H. Shimada, and K. Siddiqu, "Effect of overhead work on muscle fatigue and postural stability," in *2015 37th Annual International Conference of the IEEE Engineering in Medicine and Biology Society (EMBC)*, pp. 1506–1509, IEEE, 2015.

[121] A. Copco, "Power tool ergonomics: How to improve operator well-being and productivity." https://www.atlascopco.com/content/dam/atlas-copco/industrial-technique/ergonomics/documents/PowerToolErgonomics.pdf, 2020. Accessed: 9 July 2025.

[122] Canadian Centre for Occupational Health and Safety (CCOHS), "Hand tool ergonomics." https://www.ccohs.ca/oshanswers/ergonomics/handtools/tooldesign.html, 2023. Accessed: 9 July 2025.

[123] L. Bi, A. G. Feleke, and C. Guan, "A review on emg-based motor intention prediction of continuous human upper limb motion for human-robot collaboration," *Biomedical Signal Processing and Control*, vol. 51, pp. 113–127, 2021.

[124] H. Dimitrov, A. Bull, and D. Farina, "High-density emg, imu, kinetic, and kinematic open-source data for comprehensive locomotion activities," *Scientific Data*, vol. 10, p. 789, 2023.

[125] S. L. Colyer, M. Evans, D. P. Cosker, and A. I. Salo, "A review of the evolution of vision-based motion analysis and the integration of advanced computer vision methods towards developing a markerless system," *Sports Medicine-Open*, vol. 4, no. 1, p. 24, 2018.

[126] R. Li, N. Peterson, H. Walter, R. Ommer, S. Leonhardt, and C. Ngo, "Review of the upright balance assessment based on the force plate," *International Journal of Environmental Research and Public Health*, vol. 18, no. 5, p. 2696, 2021.

List of Publications

Publications Under Review

- Lago, F., Missiroli, F., Masia, L., & Carbone, G. *Design and Preliminary Tests of a Novel Lightweight Multi-Degree of Freedom Cable-Driven Exoskeleton for Coordinated Shoulder and Elbow Assistance*.Robotica, under review.

Published Journal Articles

- Lago, F., Leone, S., Curcio, E. M., Lamonaca, F., & Carbone, G. (2026). *A Cost-Oriented and User-Friendly Performance Assessment Procedure for Passive Upper Limb Exoskeletons*. Journal of Bionic Engineering, 1–17.
- Perrelli, M., Lago, F., Garofalo, S., Bruno, L., Mundo, D., & Carbone, G. (2025). *A critical review and systematic design approach for innovative upper-limb rehabilitation devices*. Robotics and Autonomous Systems, 183, 104835.
- Leone, S., Lago, F., Lavia, G., Macrì, F. P., Sgamba, F., Tozzo, A., Adamo, D., Avila, J. M. N., & Carbone, G. (2025). *Design and Experimental Validation of a Unidirectional Cable-Driven Exoskeleton for Upper Limb Rehabilitation*.Applied Sciences, 15(22), 11996.
- Leone, S., Lago, F., Pisla, D., & Carbone, G. (2025). *A Systematic Approach for Robotic System Development*. Technologies, 13(8), 316.
- Rodríguez-León, J. F., Chaparro-Rico, B. D., Cafolla, D., Lago, F., Castillo-Castañeda, E., & Carbone, G. (2024). *Design of a Novel Exoskeleton with Passive Magnetic Spring Self-locking and Spine Lateral Balancing*. Journal of Bionic Engineering, 21(1), 236–255.
- Curcio, E. M., Lago, F., & Carbone, G. (2024). *Design Models and Performance Analysis for a Novel Shape Memory Alloy-Actuated Wearable Hand Exoskeleton for Rehabilitation*. IEEE Robotics and Automation Letters, 9(10), 8905–8912.
- Leone, S., Giunta, L., Rino, V., Mellace, S., Sozzi, A., Lago, F., ... & Carbone, G. (2024). *Design of a Wheelchair-Mounted Robotic Arm for Feeding Assistance of Upper-Limb Impaired Patients*. Robotics, 13(3), 38.
- Rodinò, S., Lago, F., Malyshev, D., & Carbone, G. (2023). *Design Of A Movable Palm for A 3-Fingers Robotic Hand*. International Journal of Mechanics and Control, 24(1), 177–188.

Conference Publications

- Lago, F., Leone, S., Curcio, E. M., & Carbone, G. (2025). *Challenges in Designing and Adopting Robotic Rehabilitation Systems*. In International Workshop IFToMM for Sustainable Development Goals (pp. 118–125). Springer.

- Curcio, E. M., Gencarelli, G., Rodinò, S., Lago, F., Felicetti, F., Carbone, G., and Lamonaca, F. (2025). *Development of a Virtual Laboratory for Simulating Real Experiences: The Case of a Hybrid Drone in Complex Urban Environments*. In Proc. 2025 IEEE 13th Int. Conf. Intelligent Data Acquisition and Advanced Computing Systems: Technology and Applications (IDAACS), pp. 1057–1061.

- Khadem, M., Leone, S., Malyshev, D., Lago, F., & Carbone, G. (2025). *Preliminary Experimental Test of Thermal Exploration Using a Thermocamera for Specific Applications in Cultural Heritage*. In Proceedings of Jc-IFToMM International Symposium, Vol. 8 (pp. 71–77). Japanese Council of IFToMM.

- Arcorace, G., Caruso, G., Cavallaro, P., Paglia, A. P., Sollazzo, C., Tripodi, M., Curcio, E. M., Lago, F., ... & Carbone, G. (2023). *Design and Prototyping of Novel Chimney Cleaning Robot*. In IFToMM World Congress on Mechanism and Machine Science (pp. 910–918). Springer.

- Arcorace, G., Caruso, G., Cavallaro, P., Paglia, A. P., Sollazzo, C., Tripodi, M., Curcio, E. M., Lago, F., ... & Carbone, G. (2023). *Towards the Design of a User-Friendly Chimney-Cleaning Robot*. Machines, 11(11), 1024.

- Curcio, E. M., Lago, F., Rodino, S., & Carbone, G. (2023). *Examples of a Learning-By-Doing Approach for Bachelor and Master Students Approaching Robot Design*. In State-of-the-Art and Innovations in Mechanism and Machine Science: A Tribute to Carlos López-Cajún (pp. 123–140). Springer.

- Ferrise, G., Curcio, E. M., Lago, F., & Carbone, G. (2023). *Design and Operation of a Cable-Driven Robot for Lower-Limb Rehabilitation*. Mechanisms and Machine Science, 127, 197–207.

- Rodríguez-León, J. F., Lago, F., Curcio, E. M., Flores-Campos, J. A., & Carbone, G. (2023). *An Experimental Testing Procedure for Validating a Passive Upper-Limb Exoskeleton*. Mechanisms and Machine Science, 133, 211–219.